UNIVERSITY OF CALIFORNIA,
IRVINE

An activating GNAQ R183Q mutation drives port wine birthmark lesion formation in a vascularized organ-on-chip microphysiological system

DISSERTATION

submitted in partial satisfaction of the requirements
for the degree of

DOCTOR OF PHILOSPHY

in Biological Sciences

by

William K. Van Trigt

Dissertation Committee:
Professor Christopher C.W. Hughes, Chair
Professor Kristen M. Kelly
Professor Melissa Lodoen
Professor Peter Donovan

2024

DEDICATION

To my amazing family:

Lori, John, Benji, and Alex

Thank you for the endless love and support.

TABLE OF CONTENTS

LIST OF FIGURES

Page

LIST OF TABLES

ACKNOWLEDGEMENTS

There are a lot of people that I would like to thank for their personal and professional support during my graduate studies.

Firstly, I would like to thank my thesis advisor, Dr. Chris Hughes, for his support during my graduate career, especially during the multiple once-in-a-grad-school-catastrophes that just seemed to keep coming. His compassion and understanding when things were not working are not qualities that have gone unnoticed. I would also like to Dr. Kristen Kelly for her amazing expertise in helping me guide this project towards a successful completion. Her input over the years has been invaluable. Additionally, I would like to thank the rest of my committee members, Dr. Melissa Lodoen, Dr. Craig Walsh, Dr. Matt Inlay, and Dr. Peter Donovan for rounding out my committee with incredible knowledge and support both for my dissertation project and for my success in the graduate program.

I would also like to thank the staff at the UCI core facilities. Vanessa Scarfone and Pauline Nguyen at the UCI Sue and Bill Gross Stem Cell Research Center, as well as Dr. Melanie Oakes and Valentina Ciobanu at the UCI Genomics Research and Technology Hub have been very helpful in key aspects of this project.

Thank you to the UCI Sue and Bill Gross Stem Cell Center T32 Trainee Program, funded by the National Institute for Neurological Disorders and Stroke (NINDS). Your funding for two years of my graduate career, and especially the guidance under Dr. Peter Donovan and Dr. Leslie Thompson, have been very important in understanding the way that I collaborate with others. The professional development I received under your stewardship has made me a better scientist and colleague.

I also want to thank my lab mates. In particular, Chris Hatch and Makena Ewald—I cannot imagine doing this without you. You've helped me through the lows of graduate school and I am so happy to celebrate the highs with you now. Mentoring Zee has been an honor.

I would be remiss to overlook the contributions that my family has made to my success. My mom and dad, brother, and extended family have always supported my education and it is upon their solid foundation that I have been able to dedicate myself through college and graduate school. You are the reason I am the man I am today.

Lastly, I want to thank the friends I made in graduate school. To my pandemic bubble: Julia DeRogatis, Emily Neubert, and Makena Ewald, I love you. Thank you for sharing your friendship and compassion, as well as your passions for trashy food and trashy TV. Alex Cocoles, Chris Hatch, and Zac Bracken, I hope nothing but nat 20s for you all. You are great examples of kind, intelligent men that I look up to. To everyone that has kept me sane over the last six years, including our therapy fluffies, Jazz, Maisie, and especially Benji, I cannot express the gratitude and love for your support.

Thank you.

VITA

William K. Van Trigt
University of California, Irvine

EDUCATION

University of California, Irvine 2024
PhD. Biology, emphasis in vascular biology, microphysiological systems
Advisor: Dr. Christopher C.W. Hughes

California State University, Channel Islands 2015
M.S. Biotechnology

University of California, Davis 2011
B.S. Neurobiology, Physiology, and Behavior

RESEARCH EXPERIENCE

University of California, Irvine 2018-2024
Doctoral Candidate
Department of Molecular Biology and Biochemistry

Celavie Biosciences (Oxnard, CA) 2014-2018
Research Associate

Monsanto (Oxnard, CA) 2012-2014
Laboratory Technician IV

University of California, Davis 2008-2011
Undergraduate Student Researcher
Dr. Jorge Dubcovsky, Department of Plant Sciences

PUBLICATIONS

Messele, F., **Van Trigt, W.,** Arkin, L., Hughes, C.C.W. and Kelly, K.M. (2024). Port Wine Birthmark Therapy: A New Direction. *Lasers in Surgery and Medicine*. 56: 529-531. doi:10.1002/lsm.23810

Hatch C., Piombo S., Fang J., Gach J., Ewald M., **Van Trigt W.**, Coon B., Tong J., Forthal D., Hughes C. (2024). SARS- CoV-2 infection of endothelial cells, dependent on flow-induced ACE2 expression, drives hypercytokinemia in a vascularized microphysiological system. *Front. Cardiovasc. Med.* 11:1360364. doi:10.3389/fcvm.2024.1360364

Van Trigt, W., Kelly, K., Hughes, C. (2022). GNAQ mutations drive port wine birthmark-associated Sturge-Weber syndrome: A review of pathobiology, therapies, and current models. *Front. Hum. Neurosci.* 16, 1006027. doi:10.3389/fnhum.2022.1006027

Tierney W., Uhlendorf T., Ortega B., Magaña J., Ochoa J., **Van Trigt W.**, Cruz A., Kopyov A., Kopyov O., Cohen R. (2020). Transplanted Human Neural Progenitor Cells Attenuate Motor Disfunction and Lengthen Longevity in a Rat Model of Ataxia. *Cell Transplantation,* 29(1), 1-12. doi:10.1177/2F0963689720920275.

Nuryyev R., Uhlendorf T., Tierney, W., Zatikyan S., Kopyov O., Kopyov A., Ochoa J., **Van Trigt W.**, Malone C., Cohen R. (2017). Transplantation of Human Neural Progenitor Cells Reveals Structural and Functional Improvements in the Spastic Han-Wistar Rat Model of Ataxia. *Cell Transplantation, 26*(11), 1811-1821. doi:10.1177/0963689717723637.

PRESENTATIONS

Van Trigt, W., Hatch, C., Piermatteo, Z., Kelly, K., Hughes, C. (2023, Oct 15-19). *iPSC-derived EC to model port wine birthmark in a microphysiological system.* [Conference Presentation]. NAVBO 2023. Newport, RI. Abstract award.

Van Trigt, W., Kelly, K., Hughes, C. (2023, Oct 13). *A port wine birthmark model to understand biology and evaluate potential medications.* [Conference Presentation] Sturge-Weber Foundation Patient and Family Conference. Irvine, CA.

Van Trigt, W., Hatch, C., Ewald, M., Chen, Y., Lee, A., Kelly, K., Hughes, C. (2022, Oct 13-17) *Development of a Port Wine Birthmark Microphysiological System.* [Poster Presentation]. IVBM 2022. Oakland, CA. Awarded travel grant.

Van Trigt, W., Kelly, K., Hughes, C. (2022, Oct 22). *Development of a Port Wine Birthmark Model*. [Conference Presentation]. Sturge-Weber Foundation Patient and Family Conference. Irvine, CA

Hatch C., Piombo S., Fang J., Gach J., Ewald M., **Van Trigt W.,** Coon B., Forthal D., and Hughes C. (2022, May 30 - Jun 3) *Development of a Humanized In Vitro Vascular Model to Study Hypercytokinemia and Endothelial Dysfunction in SARS-CoV-2 Infection.* [Poster Presentation]. MPS World Summit 2022. New Orleans, LA

Ewald M., Hatch C., Piombo S., **Van Trigt W.,** Chen Y., Kelly K., Lee A., and Hughes C. (2022, May 30 – Jun 3). *Development of a Perfusable Vascularized Micro Organ System for the Study of Vascular Biology and the Vascular Niche.* [Poster presentation]. MPS World Summit 2022. New Orleans, LA

Van Trigt W., Ewald M., Hatch C., Piombo S., Chen Y., Kelly K., Lee A., and Hughes C. (2021, Oct 25-29). *Development of a Perfusable Vascularized Micro Organ System for the Study of Vascular Biology and the Vascular Niche.* [Poster presentation]. NAVBO 2021. Online only

AWARDS, HONORS, AND GRANTS

2023 Tewari Family Foundation Award—School of Biological Sciences, UCI
T32 Stem Cell training fellowship, NIH (5T32NS082174-08; 2020-2022)
NAVBO Travel Award—IVBM 2022
Moderator-Led Select Poster Discussion—NAVBO 2021

MENTORING
Zee S. Piermatteo, Undergraduate Researcher, UCI (2022-2024)

TEACHING EXPERINECE
University of California, Irvine

MolBio 118L, Microbiology	Fall 2019
MolBio 121, Immunology	Fall 2019, Winter 2020
Bio 98A, Biochemistry	Winter 2020

PROFESSIONAL DEVELOPMENT

Mentorship Excellence Program	2023
CliftonStrengths Talent Assesment	2022
GPS STEM	2018-2020

SKILLS
In vitro techniques: PCR and qPCR, restriction enzyme digestion, gel electrophoresis for agarose and SDS-PAGE gels, bacterial cloning and plasmid purification, DNA and protein extraction (from a variety of vegetable and mammalian cells), animal handling and surgeries, cell culture, aseptic technique, lentiviral production, western blot, spectroscopy, brightfield/ fluorescence/ confocal microscopy, stem cell maintenance and differentiation, flow cytometry, histology, ELISA, microphysiological systems, microfluidics design, 3D printing, protocol development, quality management ISO 9001: 2008

Software: Angiotool, BLAST, Benchling, FACS Diva, FCS Express, Fiji (ImageJ), FlowJo, Fusion 360, Gen5, GraphPad Prism V9, LabArchives, LasX, LIMS applications, Matlab, PreForm, R, SAP, SharePoint document systems, SmartSheet, SPSS Statistical Package, Zotero

Communication: Public speaking, collaboration, technical writing, peer-reviewed publication, teaching, and mentoring.

ABSTRACT OF THE DISSERTATION

An activating Gnaq R183Q mutation drives port wine birthmark lesion formation in a vascularized organ-on-chip microphysiological system

by

William K. Van Trigt

Doctor of Philosophy in Biological Sciences

University of California, Irvine 2024

Professor Christopher C.W. Hughes, Chair

Port-wine birthmark (PWB) is a progressive, congenital blood vessel disease that affects roughly one in 350 people and manifests as a light pink patch on the face or neck that can darken with age and develop soft tissue hypertrophy or nodularity. A portion of PWB patients have vascular lesions that are not superficial, affecting dentition, eyes, and/ or brain tissues and causing a variety of neurological and cognitive deficits called Sturge-Weber Syndrome (SWS). Most superficial PWB is resolved with pulsed-laser therapy during the first decade of life; deeper vascular lesions and some skin lesions, however, are difficult to treat and developing new therapeutic strategies has stalled over the last few decades. Several hurdles to therapeutic progress include poor understanding of disease biology and limited *in vitro* and *in vivo* models of PWB.

Port-wine birthmarks are caused by endothelial somatic mutations within the Gnaq protein's GTP hydrolysis site, which likely over-activates downstream growth and survival pathways of the endothelial cells containing a GNAQ mutation. We have used a

multidisciplinary, translational approach to develop a microphysiological model of PWB lesions using our *in vitro* vascularized micro-organ (VMO) platform.

Here we lay out our progress developing an autologous model of *in vitro* vasculogenesis for the study of PWB. We can recapitulate in this model using GNAQ-mutant vasculature the formation of dilated vascular lesions seen in patients. Through single cell transcriptome analysis of PWB patients and this model system, we additionally identify overexpression of BMP2 in PWB mutant EC as potential drivers of vascular lesion formation. Future experiments plan to leverage this novel mechanism for the discovery of effective therapeutics.

CHAPTER 1: Introduction

1.1 The Vascularized Micro Organ

Despite advancement in biological and medical technologies, one challenge in translating traditional basic science research to the patient clinic is applying inferences about efficacy and safety from model systems to patients. Traditional cell culture-based model systems lack the complexity seen in human tissues, while animal models often operate under a manipulated disease state [1]. As examples, drug toxicity can be challenging to evaluate in rodents because metabolism in rodents is different from humans; additionally, many human diseases like Alzheimer's disease are human-specific and have to be artificially created in rodents for *in vivo* research [2,3]. Thus, there is an interest in developing better human *in vitro* models to compliment animal studies, especially those that include human vasculature.

The vascularized micro organ (VMO) is a sophisticated *in vitro* cell culture device developed by our lab to study human microvessels. It has been used to study developing endothelium [4–10] and the impact that the extracellular matrix (ECM) has on the vasculogenesis process [11,12]. Additionally, we have interrogated the tissue-specific and disease-specific microenvironments in tissues like the brain, liver, and pancreas [13,14] as well as in various cancer types [15–21]. This approach allows us to interrogate complex biological interactions in a novel way. Here we outline some of the features of the VMO and discuss advantages and disadvantages of using this cell culture technique for vascular biology.

The VMO is a type of cell culture technique called a microphysiological system (MPS). There are three features of an MPS that are key to include: *i.* multiple cell types are used in *ii.* a three-dimensional (3D) space which *iii.* experiences fluid flow [22].

Traditional techniques using two-dimensional (2D) cell culture of endothelial cells (ECs) are poor representations of the structural environment that these cells usually grow in. In the body, the endothelium is a highly dynamic, structural tissue in which the EC must organize into lumenized structures to permit blood flow. Cell culture on 2D plastic not only removes the ability for the EC to grow lumenized structures, but it also limits the amount of cell-cell junctional contact that is typical of an intact endothelial barrier [23].

The multiple cell types used to create an MPS play a key role in promoting endothelial function. A healthy endothelium is comprised of a hollow tube of endothelial cells, where the abluminal surface interacts with cell types such as pericytes, smooth muscle cells, and various tissue-specific cell types like astrocytes. We and others have shown that these perivascular stromal cells assist in the formation and maintenance of the vascular network [11,12]. Omitting these stromal cells from a model obscures some of the tissue biology at play in homeostatic and diseased vascular states and limits study impact and/ or application.

The fluid forces in an MPS model, lastly, play an important role in formation and maturation of the tissue system. Many next-generation *in vitro* techniques are static-culture models—these models still capture cell-cell and cell-matrix interactions but have limitations in representing more complex tissue structures [22]. In the body, blood flow through the vasculature delivers nutrients and oxygen, removes metabolic waste, and carries important cells and signaling mechanical and chemical cues that influence tissue development and maintenance in healthy and disease states. EC are highly flow-sensing cell types on their luminal surface and largely change gene expression in

response to fluid shear on the cell membrane. These changes can cause vascular remodeling of the endothelium and drive signaling between EC and perivascular cells. MPS devices generally have gravity or pump-driven fluid flow through the tissue chamber to achieve this biomechanical stimulus.

These three aspects of an MPS are important for studying vascular biology described in later chapters. By using vasculogenesis as a readout for induced pluripotent stem cell-derived endothelial cell (iEC) function, we hold differentiated cells to a higher functional standard, rather than typical surface marker expression as a marker of cell “purity”. In particular, the Hughes Lab MPS model is an effective tool to evaluate vasculogenesis, the process of *de novo* blood vessel formation that naturally occurs during embryonic development from endothelial progenitor angioblast cells [24–26]. This process differs from angiogenic growth of new vessels sprouting from pre-existing vessels [24–26].

In brief, the VMO is created by clotting a single cell suspension of EC and stroma in a fibrin hydrogel within a tissue chamber made of polydimethylsiloxane (PDMS) (FIGURE 1.1) [27]. Three diamond-shaped tissue chambers are patterned per MPS device, 12 devices per plate (FIGURE 1.1 A). The PDMS device layer is attached to a (3-mercaptopropyl)trimethoxysilane (MPS) treated polypropylene bottomless 96-well plate. The wells of the plate align with media inlets and outlets in the PDMS device layer such that media placed into the plate wells serve as a media reservoir for the plate. Establishing a hydrostatic media pressure head directs media from the higher volume media inlet reservoir, through the media channels to the tissue chamber and out the lower pressure media outlet channel, mimicking fluid flow through an arteriole- and

venule-like channel in a gravity dependent manner. Using fluorescently labeled EC, we track the vasculogenesis process over the course of about a week as the EC change from individual cells in the fibrin hydrogel to polarized, connected networks of cells that eventually lumenize and can be tested for vascular permeability using fluorescent dyes (FIGURE 1.1 B-C). Computational Comsol modeling of cell culture media flowing through the tissue chambers demonstrated approximately 0.5 dynes per cm^2 on the luminal surface of the EC (FIGURE 1.1 D). The vascularized chamber is also an excellent model for studying drug delivery to the tissue as potential therapeutic compounds are administered through the circulation in a physiologically relevant way. Modifications to the cell sourcing and MPS design used for this dissertation project are discussed in Chapters 2 and 3, and applied to port wine birthmark disease modeling in Chapter 4.

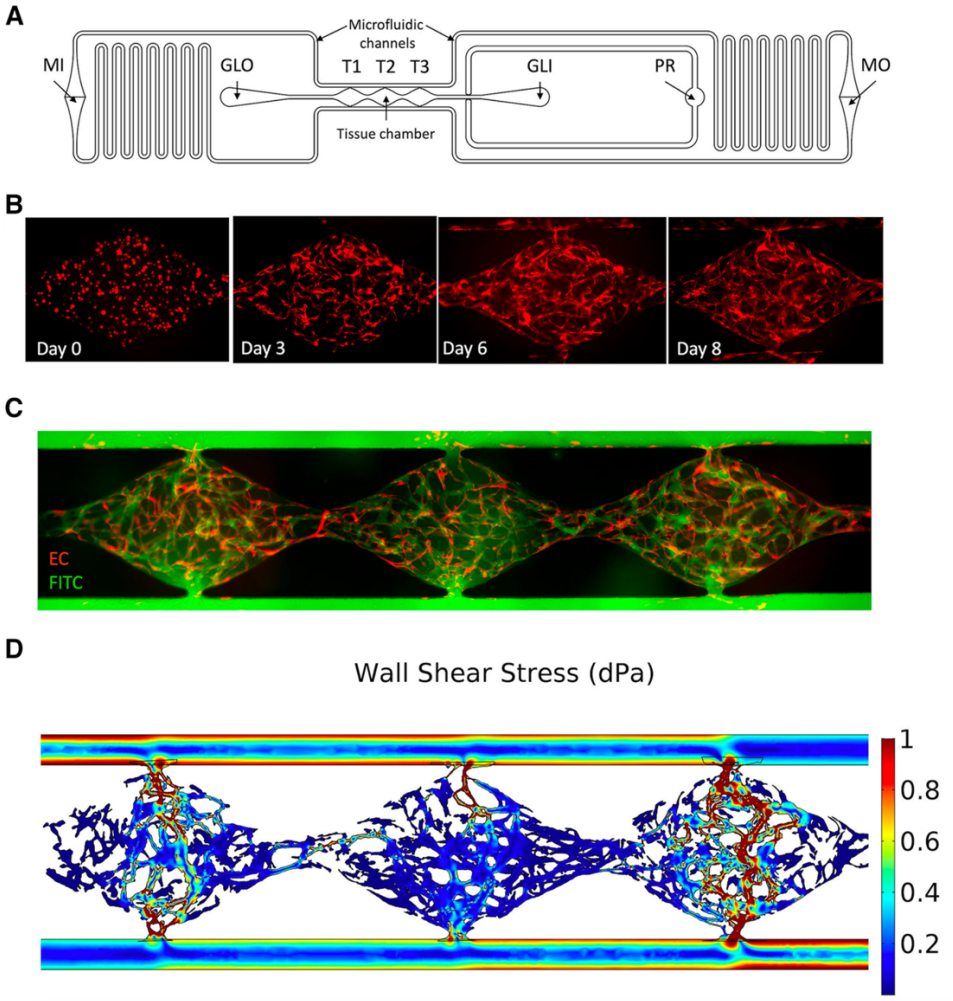

FIGURE 1.1: The VMO is a model of vasculogenesis.

Adapted from Hatch and Piombo *et al.* [27]. (A) Schematic of MPS design. 3 diamond tissue chambers are fed via media channel inlets and outlets. (B) EC (red) form a vascular network over about 1 week. (C) perfusion of 70kDa dextran dye (green) through EC (red) network to test lumenization of the vascular network. (D) Comsol computational modeling of fluid pressure through vascular network, corresponding to approximately 0.5 dynes/cm^2 at max shear stress.

1.2 GNAQ Mutations Drive Port Wine Birthmark-Associated Sturge-Weber Syndrome: A Review of Pathobiology, Therapies, and Current Models

William K Van Trigt[1], Kristen M Kelly[2], Christopher CW Hughes[1]

1. Department of Molecular Biology and Biochemistry; School of Biological Sciences; University of California, Irvine
2. Department of Dermatology; School of Medicine; University of California, Irvine

We published in November 2022 the following review article in the special research topic “Brain Arteriovenous Malformations: Cerebrovasculature Behaving Badly” of Frontiers in Human Neuroscience.

ABSTRACT

Port wine birthmarks (PWBs) are caused by somatic, mosaic mutations in the G protein Guanine nucleotide binding protein alpha subunit q (GNAQ) and are characterized by the formation of dilated, dysfunctional blood vessels in the dermis, eyes, and/or brain. Cutaneous PWBs can be treated by current dermatologic therapy, like laser intervention, to lighten the lesions and diminish nodules that occur in the lesion. Involvement of the eyes and/or brain can result in serious complications and this variation is termed Sturge-Weber Syndrome (SWS). Some of the biggest hurdles preventing development of new therapeutics are unanswered questions regarding disease biology and lack of models for drug screening. In this review, we discuss the

current understanding of GNAQ signaling, the standard of care for patients, overlap with other GNAQ-associated or phenotypically similar diseases, as well as deficiencies in current *in vivo* and *in vitro* vascular malformation models.

Keywords

GNAQ, Gαq, Port Wine Birthmark, Sturge-Weber Syndrome, brain vascular malformation, capillary malformation

1. INTRODUCTION

Port wine birthmark (also known as nevus flammeus and Port Wine Stain) is a congenital, progressive blood vessel disease that manifests as regions of skin that darken and thicken with age (FIGURE 1.2) [28]. Approximately one in 350 newborns is born with capillary malformations (CM) like PWB [29,30]. PWB lesions are usually apparent from birth as a unilateral light pink to red patch typically on the face or neck, although PWB can occur on any area of the body [31]. CMs that are also found in the eyes and/or the brain are commonly referred to as Sturge-Weber Syndrome (SWS). SWS has also been described as an over-arching syndrome with three types – Type I with neurological and skin involvement, with or without glaucoma; Type II with skin, but no neurological involvement, with or without glaucoma; and, Type III neurological only [32]. In this review we will discuss cutaneous CMs as PWB and CMs with neurological involvement as SWS.

The CMs associated with PWB/SWS are caused by a somatic activating mutation in GNAQ (although sometimes found in the paralog GNA11) that results in an

arginine to glutamine substitution at the 183 amino acid residue (p.R183Q) [33]. Disease appears to be manifested by expression of this mutant protein primarily, perhaps exclusively, in endothelial cells leading to an increase in proliferation and capillary overgrowth, as summarized in FIGURE 1.3. A glutamine to leucine (p.Q209L) GNAQ mutation can also cause capillary malformations and cancer, although this mutation has not yet been reported in PWB patients [34–36]. It has been included in this review in discussions of possible overlap with p.R183Q GNAQ constitutive activity. PWB and SWS are typically differentiated from other types of capillary vascular lesions through genetic tests that confirm the presence of mutant GNAQ in these lesions.

Since the mutations are somatically acquired, no difference in disease prevalence is expected or known to occur between sexes or races, although there are discrepancies in diagnosis and treatment.

2. PORT WINE BIRTHMARK

As noted above, PWB lesions can occur anywhere on the body but are particularly prevalent around the head and neck. Without treatment (or with treatment-resistant PWB), cutaneous lesions have the potential to progress with vascular hyperplasia, increasing prevalence of ectatic (dilated) vessels that cause the skin to darken in color (from pink or red to purple), and in some cases nodularity can develop [28,37]. Perivascular cell disorganization is also observed [33]. Disease progression is slow, however, so patients may not experience serious pathologies until late teens or adulthood.

Nodules are predicted to occur in about 40 percent of untreated PWB, with a mean onset of 22 years, and soft-tissue hypertrophy is seen in about 60% of cutaneous PWB patients [30,38]. Early laser intervention is thought to significantly delay onset of nodularity, however nodularity and hypertrophy can be difficult to treat with lasers and may require excisional surgical intervention [39]. The exact mechanisms leading to hypertrophy and nodularity are not characterized, but Yin *et al.* identify upregulation of PP2A, DAG, and activation of PI3K, PKCα, PDPK1, and PLCγ in the patient tissue [28]. This aberrant signaling was mostly detected in the endothelial cells (EC) but also had some spillover into surrounding fibroblasts and pericytes proliferating in the stromal tissue, although whether these effects are cell autonomous or due to endothelial-released factors is not known [28]. However, multilineage detection of mutant GNAQ and aberrant downstream targets in PWB tissue suggest that the somatic mutation may be propagated from a progenitor cell population into several adult cell types, in addition to EC [28,33]. Other researchers have predicted or detected the driving of lesion formation by mutant GNAQ (GNAQ*) through Angiopoietin 2 (ANGPT2), PI3K, and MAPK activation [40–43].

Both the p.R183Q and p.Q209L GNAQ mutations are located within the predicted GTP binding cleft and help stabilize GNAQ affinity for the GTP-bound “on” state (FIGURE 1.4). Recent data suggests the p.209 position also plays a role in the switch II domain (discussed later) that helps shield the binding cleft from regulatory proteins [30,34]. Simultaneous GNAQ and GNA11 mutations are uncommon in patients [35,44]. Downstream RAS pathway activation was proposed early on as the causative driver of pathogenesis because it explains how affected cells increase proliferation and inhibit

apoptosis [30]. GNAQ* cells typically comprise 6-85% of the total endothelial cells (ECs) in the PWB lesion; the range in heterogeneity correlates with disease severity, with higher ratios of mutant GNAQ cells contributing to increased pathology [28,31,33,41,45]. Testing for genetic panels usually costs about US $3,000 and are often not covered by insurance [46].

3. STURGE-WEBER SYNDROME

SWS was named after William Allen Sturge and Frederick Parkes Weber [28,30,31]. PWB endothelium in what has traditionally been called the ophthalmic V1 trigeminal nerve distribution is associated with SWS, perhaps reflecting the lineage that underwent the somatic mutation in GNAQ during development [29,30]. More recent studies have identified PWB cutaneous lesions in the triangular area from the forehead midline, outer edge of the eye, and top of the ear as the best prediction of SWS involvement (FIGURE 1.5) [47,48]. This area is called the frontal placode and typically develops its own vasculature derived from the prosencephalon and anterior mesencephalon. SWS affects approximately one in 50,000 individuals [29,30]. About 80% of SWS patients have the p.R183Q GNAQ mutation [41–43]. SWS is characterized by cutaneous PWBs which are usually more extensive than nonsyndromic PWB, ophthalmologic impairment, especially glaucoma, and malformed vessels in the thickened leptomeninges [43]. These torturous leptomeningeal vessels cause neurological deficits, macrocephaly, seizures, astrocytosis, and cortical atrophy with calcification [41,43,45]. Dilated deep draining veins can exacerbate SWS pathology. SWS leptomeningeal vessels also have increased fibronectin and VEGF expression and EC proliferation and apoptosis [30]. Seizures occur

in 75% of patients within the first year of life and 90% of SWS patients will experience seizures before 2 years of age [30]. Since the GNAQ mutations in SWS are widely prevalent in the EC compartment, many researchers speculate that the GNAQ*-EC have impaired blood brain barrier capability and possibly aberrant interactions with surrounding tissue in the leptomeninges and cortex that cause these neurovascular dysfunctions and seizures, possibly due do hypoxia, ischemia, and gliosis [30,41].

As noted, there are three different subclasses of SWS that are sometimes referenced in the literature and that vary from each other by the combination of tissues involved. Type I SWS involves cutaneous PWB and brain vascular malformations with or without eye involvement (usually glaucoma). Type I SWS is the most common and usually only affects one side of the brain [32]. Type II involves facial cutaneous PWB and eye involvement but not brain. Type III characterizes SWS with brain vascular malformations without skin PWB or (rarely) eye. Type III can only be diagnosed via brain scanning [32]. These categories have not been universally adopted; we and others hypothesize that the type of classification is not useful because treatment decisions are made on an individual level depending on symptoms, patient age, and disease severity [48].

About half of SWS patients have pathogenesis that affects the eyes (Type I and II) [34,45]. In this case, a patient may develop choroidal hemangioma, seen as PWB vessel overgrowth in the choroid that leads to thickening of the choroid and increased intraocular and intravenous pressures, eventually causing glaucoma [45,49]. Choroidal hemangioma, unlike infantile hemangioma is not responsive to propranolol treatment. Common treatment includes therapeutics to lower intraocular pressure or enucleation

surgery. Only the p.R183Q GNAQ mutation has been detected in choroidal hemangioma patients, although this is probably sampling error from small datasets.

The remainder of this review will focus on GNAQ and its role in driving PWB-associated SWS. We do not intend to be exhaustive but will concentrate on the current literature regarding GNAQ signaling, the role of GNAQ in driving brain capillary malformations, and on illuminating current exciting research on molecular mechanisms and models of disease pathology.

3.1 DIAGNOSIS OF SWS

Extracutaneous involvement is suspected with SWS whenever patients have PWB on their forehead, even without the presentation of neurological symptoms. SWS involvement can be evaluated through a variety of imaging techniques that play a crucial role in detection, diagnosis, and follow-up of this disease.

3.1.1 Computed tomography (CT)

Computed tomography with or without contrast enhancement is frequently used due to its ability to detect reduced parenchymal brain volume, enlarged ventricles, or enlarged choroid plexus. CT scans can also detect calcification better than x-ray or magnetic resonance imaging [30].

3.1.2 Magnetic resonance imaging (MRI)

Gadolinium enhanced MRI is the principle imaging technique used for SWS diagnosis [30]. It can effectively identify calcified areas as well as structural and functional anomalies in the leptomeninges, abnormal venous drainage, reduced and/or enlarged brain structures, and hypermyelination underneath the leptomeningeal lesion(s) [30].

3.1.3 Perfusion imaging

Perfusion imaging can play a crucial role in identifying stage of disease. Perfusion imaging may be performed in several ways: in conjunction with CT or MRI; or, by using radiotracers and either single photon emission computed tomography (SPECT) or positron emission (PET) techniques. Most SWS lesions tend to be hyperperfused with blood early in childhood, but this tends to change to hypoperfusion later—leading to progressive ischemia, hypoxia, and nutrient starvation of the brain around the vascular malformation [30]. It is predicted that this switch to progressive hypoperfusion in SWS is responsible for the neurological degradation characteristic of this disease.

3.1.4 Electroencephalogram (EEG)

Like perfusion imaging, EEG frequently can identify progression to an increasingly abnormal SWS signature correlated with patient age. EEG readings of advanced SWS brain tissue detect epileptiform characteristics with decreased brain voltage and focal discharge in the hemisphere affected by SWS [30].

3.1.5 Angiography

Angiographical imaging is not usually performed for patients with SWS unless clinically indicated. Unlike other vascular malformation diseases, SWS lesions are low-flow malformations that are unlikely to undergo thrombotic events. Angiography may be used prior to craniotomy procedures to detect bleeding risk [30].

3.2 SWS TREATMENT

A recent consensus statement prepared by 12 top US expert clinicians in dermatology and SWS identified several key guidelines for the management of PWB associated with SWS [48].

Early diagnosis of PWB/SWS (as close to birth as possible) and intervention maximizes the success of treatment(s) [47,48]. Several factors must be weighed when designing a treatment plan, including but not limited to reducing birthmark appearance, diminishing or preventing nodularity and/or soft tissue hypertrophy, minimizing the impact to patient quality of life and self-esteem, and lastly, financial considerations.

3.2.1 Cutaneous PWB treatments

Light-based therapy, especially with pulsed-dye laser (PDL), is the standard of care for PWB in the United States [30,48]. Experienced clinicians can safely and effectively use PDL on patients of all ages, including infants. Other wavelengths (532, 755, and 1064nm) have been used and are especially useful for treating PDL-resistant PWB lesions. The longer wavelengths are also better for penetrating larger or deeper vessels like those that occur in nodular or hypertrophic lesions, but these laser devices also pose an increased risk of damage to non-target adjacent tissue [48,50]. Laser therapies target heat absorption of hemoglobin and cause photocoagulation, with the goal to remove aberrant vasculature by selective damage and photothermolysis [48,51]. PDL therapy has also been combined with other techniques like infrared laser pulses or bipolar radiofrequency to improve efficacy in treatment-resistant PWB [48,52]. Pain management is an important concern with laser therapy. Topical or injected local

anesthetics, skin cooling, nerve blockers, and/or general anesthesia can be used during treatment [48].

PDL treatment response is difficult to predict, but can lighten PWB skin color by 50-70% through at least eight to ten PDL sessions, although complete clearance is rarely achieved and touch-up follow-up treatment is frequently used to maintain level of clearance [48]. There are no consistent guidelines for intervals between treatment sessions. Patients with lighter skin tones tend to have a better PDL treatment response than those with darker skin [30,48]. Patients with darker skin require more skin cooling or adjustment of laser parameters to prevent scarring or blistering. PWB on the face and neck, especially the lateral sides of the face, are easier to treat than PWB on the lower body extremities [48,53]. It is possible that patients with SWS have PWB lesions that are more likely to be treatment-resistant, although this has not been clearly established and the mechanism is unknown [48]. As mentioned earlier, PWBs are more effectively treated in younger than older patients, especially if the affected area is still flat without signs of nodularity or hypertrophy.

There are some adjuvant treatments which have been tried with PDL, although none have achieved marked improvement over laser therapy alone and are no longer used frequently in clinical treatments [54]. Combination of PDL with topical imiquimod demonstrated slightly improved effect in treating PWB over PDL alone in small scale studies through immunomodulation activity that reduces tumor necrosis factor (TNF), interferon-γ (IFN-γ), as well as decreasing pro-angiogenic production of matrix metalloproteinase 9 (MMP9) and increasing apoptosis [54–56].

Rapamycin, an mTOR inhibitor, has been studied in a variety of diseases for its immunosuppressant and antiproliferative activities. Human clinical studies of topical rapamycin combined with PDL on affected areas of the face and neck showed some efficacy in limiting cutaneous vessel regrowth via HIF-1α and VEGF inhibition, but results were disappointing with wider clinical use [54,55]. Using animal models, PDL and axitinib, an inhibitor of MEK/ERK, have been shown to prevent vessel regrowth [57]. Efficacy in patients has not yet been demonstrated. A small scale trial with PDL and bosentan (an endothelin receptor antagonist) showed efficacy in one of four PWB patients treated [58].

As laser therapy works through excitation of hemoglobin, the perfusion of hemoglobin-laden vesicles during PDL treatment has been tried and was shown to increase efficacy of PDL for dilated and deeper vessels in animal models, improving the safety of PDL by reducing the laser intensity required and thereby reducing off-target tissue effects [59,60]. In another preclinical study, PDL therapy with the α1A- and partial α2A-adrenoreceptor agonist oxymetazoline was used for the treatment of erythematotelangiectatic rosacea and showed some efficacy for PDL combination treatment of PWB in mouse models [61]. Both of these strategies warrant further investigation.

Photodynamic therapy, unlike PDL, uses perfusion of a photosensitive dye and an excitatory source to produce reactive oxygen species (ROS) that destroy local tissue. This technique is not widely used in the US, but may be beneficial for resistant PWB, and when treating darker skin types as the melanin content of skin does not reduce photodynamic therapy efficacy [48].

Lastly, surgical intervention may be employed to selectively remove hypertrophic or nodular tissue.

3.2.2 Treatments targeted specifically for SWS

Unfortunately, SWS-specific treatments that target neurodegeneration are not currently available. The cornerstone for treatment is anticonvulsant therapy to limit damage due to seizures. Carbamazepine and oxcarbazepine are frequently prescribed to SWS patients, sometimes even prophylactically before the first incident, to prevent epileptic events [30]. Low-dose aspirin may additionally help prevent seizures and ischemia in SWS tissue. Seizures are untreatable in about half of SWS patients; in these cases, early surgical intervention with lesionectomy, corpus callosotomy, and/or hemispherectomy may be considered [30]. Patients with these invasive brain interventions as well as patients with cognitive deficits or hyperactivity may need physiotherapy, educational therapy, and behavioral therapy. Some studies have shown oral treatment with rapamycin improves cognitive function and recovery time from stroke-like episodes [62]. Larger clinical studies are required.

Treatment for glaucoma aims to prevent degeneration of the optic nerve by decreasing intraocular pressure. Placement of a drainage device is often required and aqueous suppressants or medications to increase outflow are usually effective [30].

SWS patients are prone to thyroid diseases and should be routinely examined for growth hormone deficiencies and hypothyroidism [63,64].

4. GNAQ AND THE G PROTEIN LANDSCAPE

Heterotrimeric guanine nucleotide-binding proteins (G proteins) transduce a variety of important autocrine and paracrine signals from numerous receptors, such as those for hormones, neurotransmitters, and chemokines. These effect changes in such diverse cell functions as gene transcription, metabolism, cell motility, embryonic and gonadal development, and learning and memory [65]. Reflecting this diversity of function, the G protein coupled receptor (GPCR) family has over 800 family members, and almost 30% of drug discovery targets influence GPCR signaling [66].

The G protein complex is made up of 3 subunits: α, β, and γ. Upon activation of a GPCR, the Gα subunit exchanges guanine diphosphate (GDP) for guanine triphosphate (GTP), dissociating Gα from the G$\beta\gamma$ heterodimer and allowing Gα and G$\beta\gamma$ to transduce downstream signals. There are currently 18 identified Gα, five Gβ, and 12 Gγ subunits [67]. With respect to receptor and effector specificity, and sequence and functional similarities, the Gα subunit can be further divided into four families: Gα_i, Gα_s, Gα_{12}, and Gα_q [65,68]. The Gα_i family is the biggest and most diverse group of G proteins and these are expressed in most cells, although there are a few that are specific to neurons, platelets, and rod and cone cells. The i stands for “inhibition,” as a majority of these downstream responses limit activity of cAMP-dependent protein kinases [67]. The Gα_s family (s for “stimulation”) only has two members; Gα_s is expressed in most cell types while Gα_{olf} is only expressed in olfactory sensory neurons. The Gα_{12} family also has two members that are widely expressed. Lastly, the Gα_q family has four members: GNAQ and its paralog Gα_{11} are ubiquitously expressed, while Gα_{14} and G$\alpha_{15/16}$ are expressed in soft organs (kidney, lung, and liver) and hematopoietic cells, respectively.

4.1 GENE

In humans, GNAQ is encoded by the GNAQ gene on chromosome 9 at 9q21.2 [69]. There is also a pseudogene at location 2q21as well as the paralog $G\alpha_{11}$ (GNA11) at location 19p13.31 [69]. The eight-exon GNAQ mRNA transcript is 6,882 nucleotides long, coding for a 359 amino acid protein (FIGURE 1.4; NM_002072.5, P50148.4, CCDS6658.1). Although the GNA11 paralog is also 359 amino acids long, there are areas of dissimilarities in protein sequence. These disparities do not occur in the conserved active site amino acids, however, and the GNAQ p.R183Q or p.Q209L amino acid substitutions (c.548G>A and c.626A>T nucleotide substitutions, respectively) in SWS patients can also occur in GNA11 at the same corresponding amino acid positions in GNA11-driven SWS [30,33,69]. GNA11 mutations will not be covered in this review as they cause the same constitutive $G\alpha$ constitutive activity and SWS disease pathogenesis, albeit GNA11 mutations are detected at lower patient frequency than GNAQ [45].

4.2 PROTEIN

G proteins, including GNAQ, function in a GTPase cycle. GPCRs act as a kind of guanine nucleotide exchange factor (GEF) to initiate release of GDP and binding of GTP to GNAQ, causing dissociation of GNAQ from the $G\beta\gamma$ complex (FIGURE 1.6) [67]. GNAQ-GTP is eventually hydrolyzed back to GNAQ-GDP by its intrinsically weak GTPase activity to terminate GNAQ effector function. This process of GTP hydrolysis can be expedited by GTPase activating proteins (GAPs). Re-association of GNAQ with $G\beta\gamma$ terminates the signaling cascade and completes the GTPase cycle.

The amino acid sequence of the GDT/GTP binding cleft is highly conserved [67,69]. The GNAQ protein has a RAS-like GTPase domain and an α-helical domain, connected by the Linker 1 and Linker 2 domains. The RAS-like GTPase and α-helical domains surround the GTP hydrolysis cleft, thereby protecting the GDP or GTP nucleotide from the surrounding solvent and serving as an inhibitory barrier for regulation by GEFs, GAPs, and the Gβγ complex [67]. GDP/GTP binding and hydrolysis take place in the RAS-like domain of GNAQ through a "switch" mechanism. The domain comprises six β-sheets and five α-helices on each side, defining a nucleotide-binding fold, with several key amino acids lining the fold to specify guanine binding [67,70–72]. The side loops around the cleft are the switch regions – Switch I and Switch II. The N-terminus of the Gα α-helix and the Switch II region associate with a propellor structure of Gβ in the Gβγ complex [67]. Switch I and II together with the P loop region interact with GDP/GTP and the Mg^{2+} coordinating ion. Two of the key sequences in the cleft are the NKKD sequence in Switch II, predicted to form a bifurcated hydrogen bond between aspartate and the guanine base, while the second sequence is a Walker A motif in the P-loop region where the GTGESGKS sequence is associated with binding of the β-phosphate of GDP/ GTP [67,71,73]. The α-helical domain and switch III regions play a role in G protein regulation (discussed later).

GNAQ has a high affinity for GDP. GEFs (including GPCRs) work to weaken this affinity by causing instability in the protein switch regions. GEFs on their own have a relatively low affinity for GNAQ in either the GDP or GTP bound state. Instead, for the exchange reaction to occur, the GEF must interact with the switch regions in a way that partially displaces the Mg^{2+} ion, which destabilizes bound GDP and causes a push/pull

interaction between the switch regions and GDP. The destabilized GDP is released as a stable GEF-GNAQ complex forms, leaving GNAQ available to bind GTP (GTP is usually at higher intracellular concentrations than GDP) [67]. More detailed structural and mechanistic information regarding conformational state, the ways in which GEFs initiate interaction with GNAQ, as well as the way GDP is released, still need to be elucidated.

Originally, it was thought that GPCRs diffuse freely within the cell membrane and interact with G proteins though collision, but there are data suggesting un-activated GPCRs in a pre-assembled complex with G proteins: agonist activation of the GPCR then causes a conformational change in the pre-organized complex that facilitates G protein signal transduction [67,74]. The different kinds of GPCR and G protein interaction depend on the pair, which may explain the range of GPCR activity in different cell types and tissues. Additionally, GPCR-agonist binding alone is sometimes insufficient to cause G protein activation and may require additional interactions with other proteins. On the other hand, GPCRs may require desensitization through phosphorylation of G protein receptor kinases (GRKs) or binding of GPCR inhibitory proteins like arrestin [67,75]. GNAQ's specific GPCR interaction type is unknown at this time, and additionally, it is possible the GPCR-ligand state is less relevant under GNAQ* constitutive activity.

GPCR extracellular ligands are divided into three categories: agonist, inverse agonists, and antagonists. Agonists bind to GPCRs and promote G protein signal transduction while inverse agonists stabilize the inactive "off" state. Antagonists do not change the equilibrium dynamics of the GPCR's active and inactive conformations but do block binding of agonist and inverse agonist ligands.

All 4 $G\alpha_q$ family members are palmitoylated at the Cys^9 and Cys^{10} amino acid residues, but this post-translational modification is not well understood because it does not seem to affect association of GNAQ with $G\beta\gamma$ at the GPCR interface, nor downstream effector functions of GNAQ, such as activation of the phospholipase C pathway [76].

4.3 GNAQ REGULATION

G proteins like GNAQ can be regulated by a variety of intracellular proteins (besides GPCRs), including Ric-8 (synembryn), G-protein regulatory (GPR)-domain containing proteins (GRPs), $G\alpha$-binding and activating (GBA) motif-containing proteins, and regulators of G-protein signaling (RGS) proteins.

Mammals have both Ric-8A and Ric-8B and both have been demonstrated to interact with GNAQ. Ric-8A is widely expressed while Ric-8B is restricted mostly to olfactory tissue. Ric-8A is a GEF that promotes GDP release and stabilizes the nucleotide-free GNAQ transition state by initiating conformational changes to Switch I and II regions, thereby exposing the GTP binding site to the solvent, leading to formation of the GNAQ-GTP complex [77,78]. The lack of crystal structures prevents resolution of this exact mechanism, but it is interesting that Ric-8 acts on the GNAQ-GDP monomer itself, rather than the whole GNAQ-GDP/$G\beta\gamma$ complex (like GPCRs), as well as in concert with other regulatory proteins like GRPs. Additionally, Ric-8 plays other roles as a chaperone during $G\alpha$ folding and processing in addition to membrane translocation [79].

GRP contains an ~25 amino acid long G protein regulator domain, also called a GoLoco domain, that prolongs signal transduction by sequestering Gα from the Gβγ complex and possibly assisting Ric-8A activation of the GNAQ subunit [80].

GBA domain-containing proteins, like Girdin, Dapple, NUCB1/2, and GBAS-1 interact with Gα proteins to initiate Akt signaling by accelerating the exchange rate of GDP [81,82]. As rheostats, these GBA proteins have a powerful ability to fine-tune the duration of signaling and have been implicated in cancer progression and metastasis [82]. GBA-domain proteins bind to $G\alpha_l$ and $G\alpha_s$ family members, but their direct interactions with GNAQ have yet to be confirmed.

Lastly, RGS modulate the intrinsic GTPase activity of the Gα subunit by stabilizing the GTP hydrolysis transition state, thereby encouraging deactivation of Gα. Heterogeneity in the RGS domains leads to preferential selectivity between RGS proteins and Gα subunits due to sequence-specific interactions between RGS domains and the Gα Switch I, III, and N-terminal side of Switch II [83]. RGS1, 3, 4, 8, 16, 17, and 18 bind to GNAQ and other Gα members; RGS2 seems to be specific to GNAQ [84]. RGS proteins may be an attractive target for drug development for a variety of diseases, including SWS [85].

4.4 GNAQ SIGNALING PATHWAYS

There are a variety of well-defined downstream targets of G proteins, although their role in PWB is not understood. GNAQ in particular can stimulate the phospholipase C β (PLC-β) isoforms through interactions with the GNAQ N-terminal β-1 strand, which cleaves phosphatidyl inositol 4,5-bisphosphate into inositol triphosphate (IP3) and

diacylglycerol (DAG) [76,83,86]. IP3 opens the calcium channel IP3 receptor on the endoplasmic reticulum (ER) membrane while DAG activates protein kinase C (PKC). Additionally, GNAQ uses helix-loop-helix domains in Switch II and α-helix 3 to interact with RhoGEFs like p63RhoGEF through p63RhoGEF Dbl-homology/pleckstrin-homology (DH/PH) domains [67,83,87]. Less well defined targets of GNAQ signaling include GRK2, actin, tubulin, PI3K, TPR1, Btk tyrosine kinase, phospholipase C-ε, and TRPM8 [67]. The biological significances of these are not well understood and may lie in tissue-specific functions. It is unclear how EC GNAQ* affects these factors.

It is important to note there are many G$\beta\gamma$ interactions that are influenced by GNAQ activation, including adenylate cyclase, PI3K, potassium and calcium channels, and possibly IP3 receptors, Raf kinases, protein kinase D, histone deacetylase 5 (HDAC5), tubulin, F-actin, vinculin, ElmoE, Rab11, mitofusinil, Radil, activator protein 1, TFE3, and TRPM1 [67].

There are no therapeutic agents used clinically to target GNAQ protein at the time of this manuscript's publication [88]. Instead, many treatment strategies (discussed earlier) either manage symptoms or in the case of cutaneous lesions, aim to target pathways that limit vessel regrowth after laser treatment.

5. OVERLAP WITH OTHER VASCULAR MALFORMATIONS

GNAQ mutations are found in a variety of diseases, including but not limited to: p.T96S NK/T cell lymphoma and diffuse bone and soft tissue angiomatosis [89,90]; p.R183Q Klippel-Trenaunay Syndrome [91]; p.V179M and F335L dark skin point mutations and hyperpigmentation [36,92,93]; p.Q209L or silencing mutations in non-small

cell lung cancers [94]; p.D663fs insertion and p.R385* nonsense mutations in melanocytoma [95]; p.Q209L and p.Q209P intramedullary and leptomeningeal melanomas [96]; p.S12fs*49 breast cancer [97]; and decreased GNAQ expression in brain aging and neurodegeneration [98–103]. The following diseases discussed in more detail were selected due to the possible overlap in pathogenesis or molecular interactions, with the goal of spurring synergistic research encompassing these conditions and SWS.

5.1 BRAIN ARTERIOVENOUS MALFORMATIONS

Understanding the molecular etiology of PWBs may benefit from overlapping research conducted in brain arteriovenous malformations (bAVMs). bAVM form when afferent arteries abnormally communicate directly with draining veins without an intermediary capillary bed, sometimes in a tangle called a nidus. Like PWB/SWS, bAVMs can differ substantially in size, location, morphology, architecture, presentation, and clinical treatment/ management between patients [104]. The rate of detection is 1.12-1.42 per 100,000 person years. Unlike SWS, hemorrhage is the most common presenting characteristic of bAVMs, occurring in about half of new diagnoses, with larger nidus size and deep location significantly correlated with hemorrhage risk [104–106]. Seizures (30% of new diagnoses) and headaches (5-14%) are also detected. bAVMs account for a quarter of hemorrhagic stroke in adults under 50 and almost half of bAVM patients die or have significant impairments within a year of a hemorrhagic event [107,108].

Next-gen DNA sequencing of sporadic bAVM has identified KRAS somatic activating mutations localized to the EC compartment in about half of patients [109]. These KRAS mutations activate MAPK-ERK and PI3K-AKT pathways that increase phospho-

ERK levels and lead to overall increases in EC angiogenesis, aberrant vascular EC cadherin localization, Notch signaling, and migration capacity; countering ERK overactivity with trametinib inhibition of MEK reversed these findings [110,111]. These data support the idea that MAPK-ERK activation drives bAVM formation in KRAS mutant spontaneous bAVM in a manner similar to studies that identify KRAS overactivation in PWB. Additionally, Zebrafish bAVM models treated with the BRAF inhibitor vemurafenib had restored blood flow compared to their untreated controls [111].

TGFβ family signaling mutations in familial bAVMs are detected in the autosomal dominant disease hereditary hemorrhagic telangiectasia (HHT), which affects roughly 1 in 5,000 people and is characterized by AVM formation and hemorrhage in multiple organs, including the brain, lungs, liver, and/or gastrointestinal tract [109]. EC ENG (HHT type 1) and ALK1 (HHT type 2) mutations make up the vast majority of HHT cases, while a small number can be attributed to mutations in SMAD4. In the absence of functional Alk1 it appears that angiogenic and/or inflammatory signals subsequent to injury are required for bAVM formation, and this likely involves VEGF-stimulated angiogenesis [112]. Interestingly, localized VEGF delivery in combination with ALK1 or ENG deficiency in EC, but not vascular smooth muscle cells, pericytes, or macrophages was required for bAVM formation in adult mice, suggesting that EC might be intrinsically responsible for the formation of bAVM networks [112–114]. Others have proposed similar EC-stroma miscommunication in SWS disease pathology; although SWS dilated vessels are unlike high-risk hemorrhagic lesions seen in HHT and bAVM, similar deficiencies in mural cell recruitment and wrapping as well as the presence of pro-

inflammatory immune infiltration may exacerbate vessel dilation and fibrosis, possibly through the same mechanisms [33,112,115].

As noted above, aberrant angiogenic control is implicated in bAVM progression. EC deficiencies in TGFβ family signaling can cause bAVM formation through several mediating factors, including loss or depletion of SMAD4, or activation of MEK/ERK [116,117]. Lastly, reduced expression of integrin β8 (ITGβ8) in bAVM promotes hemorrhage in response to VEGF stimulation, possibly through increased Notch and Sox-2 [118,119]. Together, these results suggest that both ITGβ8 and ALK1 are crucial for maintaining a healthy pro- versus anti- angiogenic balance. VEGF-A antagonism with bevacizumab or pazopanib can restore the angiogenic balance and prevent lesion formation [120]. Further work in this area is required, especially as overlapping research in MEK/ERK activation in SWS and bAVM may synergize.

Vessel immaturity and structural defects of the bAVM vascular wall are linked to PDGF/PDGFRβ deficiency. Dilated vessels with diameters greater than typical capillaries (greater than 15μm) are strongly correlated with decreased smooth muscle cell and pericyte coverage and increased vascular permeability and hemorrhage risk [112,121–123]. At this time, it is unclear if expression causes or results from bAVM formation, but increasing pericyte recruitment in the bAVM nidus by PDGFB expression or thalidomide/ lenalidomide treatment reduces future hemorrhage risk [122,124,125]. Increasing pericyte coverage in PWB lesions may help prevent progressive vessel dilation and instability.

Non-coding regulatory RNAs may also play a role in vascular malformation development and/or progression. Downregulation of nicotinamide adenine dinucleotide

phosphate (NADPH) reductase and lipoprotein lipase via several long non-coding RNAs may be associated with patient seizures in bAVM, while dysregulated novel miRNAs have been described to affect VEGF signaling and smooth muscle cell behavior [41,114,126]. Inactivating mutations in DROSHA miRNA processing machinery have also been characterized in zebrafish bAVM models and have been identified in HHT patients that lack other known AVM-causative mutations [127]. To the best of our knowledge, miRNA dysregulation or misprocessing have not been examined in PWB/SWS and warrant investigation.

5.2 NON-CUTANEOUS MELANOMA

GNAQ p.Q209 mutations have been implicated in more than 90% of cases of GNAQ-driven uveal melanoma (UM), although, studies conflict regarding the downstream molecular interactions driving cancer formation and progression [88,93,128,129]. The p.Q209P mutation is fairly common in UM and does not appear to significantly alter disease prognosis compared to p.Q209L, while the p.R183Q mutation is slightly less common and leads to less aggressive disease [44,130]. The p.Q209* mutations are predicted to cause more severe effects through overactivation of the MAPK pathway [35,36].GNAQ p.G48L mutation in UM is rare [131].

Uveal melanoma is currently treated with surgical resection or radiation therapy at the primary tumor site, however, treatment has not improved in decades and about half of UM is diagnosed at a late stage after metastasis has already occurred [44,88,128,130,132,133]. Feng *et al.* have demonstrated that the presence of oncogenic GNAQ mutations can cause an overactivation of FAK-mediated YAP activation, which

transcriptionally activates the TEAD transcription factor family and downstream pro-growth and pro-survival genes [128,129]. The tumor suppressive Hippo pathway is not able to effectively silence this cascade during constitutive GNAQ activity [128]. No specific YAP inhibitors are currently in clinical use, however Truong *et al*. demonstrated that combined therapy with trametinib MEK1/2 inhibition and the lysosome inhibitor chloroquine increased cytotoxicity while indirectly decreasing YAP nuclear localization and transcriptional activity [128,129]. Other groups have proposed GNAQ overactivation of ERK1/2 or MEK1/2 as a driver of UM, but inhibitors of this pathway alone are typically insufficient to stop progression and the degree of MAPK activation is widely heterogeneous within tumor sites [88,128,129,134,135].

Musi *et al*. demonstrated a dose-dependent reduction in mutant GNAQ-driven activation of ADP-ribosylation factor 6 (ARF6) using tris dibenzylideneacetone (DBA) palladium [88]. Moreover, ARF6 GTPase has been identified as an immediate downstream cancer driver in GNAQ-UM, where it plays a role in the localization and transactivation of β-catenin from the plasma membrane to the nucleus, as well as the activation of Rho-Rac pathway signaling [88,136]. Other groups have demonstrated that tris DBA compounds decrease MAPK, PKC, and AKT-driven cancers as a result of NMT-1 blockade, however Musi *et al*. did not observe suppression of these pathways nor FAK inhibition and, interestingly, saw an increase in ERK and AKT phospho-activation despite increased UM apoptosis [88]. Gene array analysis suggests tris DBA palladium additionally interferes with tumor RNA splicing and reduces resistance to chemotherapy [88]. Many of these factors driving UM may be drivers of PWB/SWS.

The presence of a nevus of Ota is one of the few predictors of risk for UM and Van Raamsdonk *et al*. have identified an 83% and 46% incidence of GNAQ p.Q209L mutations in blue nevi and UM, respectively, underscoring the overlapping relationship GNAQ plays in melanocytic neoplasms and uveal melanoma [93]. On the other hand, approximately one in 400 nevi of Ota progresses to uveal melanoma so other factors remain undefined. Van Raamsdonk *et al*. postulate that GNAQ downstream targets such as ERK- and endothelin-regulated developmental survival, as well as Wnt and metabotropic glutamate receptor (GRM1) signaling contribute to melanocytic neoplasia oncogenesis and metastasis [36,93]. Additionally, transfection of GNAQ p.Q209L in melanocytes *in vitro* demonstrated unusual anchorage-independent growth as well as large, irregularly shaped nuclei [93].

5.3 CHERRY ANGIOMAS

Cherry angiomas are the most common kind of vascular tumor in adults. They typically present on the trunk or upper extremities as small, round, red to purple dome-shaped papules composed of dilated, thin-walled capillaries surrounded by hyalinized stroma, somewhat similar to the dilated structure of cutaneous PWB [137]. Liau *et al*. detected EC GNAQ mutations in cherry angioma-like lesions in about half of all patients studied and are predicted to activate the MAPK pathway to drive pathogenesis, as in PWB/SWS [137]. It is possible that significant overlap between cherry angiomas and PWB/SWS could offer us a glimpse of how PWB/SWS lesions form *in utero* and close collaboration between researchers working in the two diseases could afford greater understanding of both.

6. MODELS OF PWB/SWS

6.1 IN VIVO MODELS

Most *in vivo* studies are typically performed using healthy animal skin models such as mice, Wistar rats, or chicken (combs or wattles) where intervention is focused on regressing normal vessels [59,60]. Alternatively, xenotransplants can be used where mutant human EC in Matrigel extracellular matrix are subcutaneously injected into mice to study vessel formation, albeit outside the normal PWB/SWS environment. Most data to date identifying mutant GNAQ and possible molecular interactions leading to pathology have been developed using genome (DNA) sequencing and histology of patient tissue samples [33,34,37,40–43,45,138]. Additional *in viv*o and *in vitro* complex studies like those performed by Huang *et al*. are needed to advance our understanding of PWB. The authors in this study identified Angpt2 as a downstream factor increased by endothelial GNAQ p.R183Q signaling that caused vessel dilation; this feature was reversed through GNAQ inhibition using YM-254890 or shRNA knockdown of Angpt2 [139]. Thorough studies that identify direct controllers of PWB vessel dysfunction are rare.

6.2 IN VITRO MODELS

As noted, there is a critical need for better models of PWB and SWS due to an absence of naturally occurring GNAQ* PWB/SWS in non-human animals and an inability of engineered *in vivo* models to successfully recapitulate SWS disease biology of humans. *In vitro* models may meet this need. Unfortunately, *in vitro* monolayer studies are inadequate for studying the complex disease pathology of PWB, which

involves multiple tissues and cell types and is characterized by clearly three dimensional lesions – dilated blood vessels [22,103]. Complex human disease models such as microphysiological systems (MPS) provide an exciting and untapped opportunity [22]. Frequently referred to as an organ-on-a-chip, these platforms combine relevant cell types in a three-dimensional, ECM-rich tissue bed, often with media delivered to the tissue chamber by perfusable EC-lined microvessels [7,8,10,22]. Phan *et al*. and others have demonstrated the utility of these platforms for screening novel and repurposed therapeutics [6,15,16,18]. In particular, MPS platforms hold promise for rare diseases like SWS, as they can successfully recapitulate many aspects of disease biology and they offer the ability to rapidly test molecular perturbations, such as gene deletion or replacement. To the best of our knowledge, no complex *in vitro* model of PWB/SWS has been published. We argue that MPS technology holds great promise for understanding the GNAQ* downstream effectors in disease progression.

In a recent manuscript posted on BioRivx, Soon *et al.* describe a mosaic EC $KRAS^{G12V}$ MPS of sporadic bAVM [140]. The authors were able to detect increased vessel dilation and permeability in $KRAS^{G12V}$ EC due to breakdown in adherens junctions and increased VEGF signaling. Finally, the authors were able to reverse some of this pathology with pharmaceutical MEK inhibition but not PIK3 inhibition, supporting further investigation in the clinic of MEK inhibition in vascular malformation studies. Complex *in vitro* studies of this nature are needed to understand PWB/SWS pathology.

7. DISCUSSION

SWS is a complicated disease in which GNAQ mutations drive progressive capillary vessel dilation and dysfunction in skin, eye, and brain tissue. The consequences for these CMs entail severe impacts to patient quality of life and include but are not limited to: glaucoma, epilepsy, cognitive deficits, and psychosocial ramifications.

As noted, in contrast to several vascular malformations, there are few good models for PWB/SWS, and as a result there are still many questions left unanswered about how PWB/SWS arises and progresses. Are the effects of GNAQ* EC autonomous or is additional dysfunction in the stroma required? How do we reconcile these disease models with the rare contribution of additional GNAQ* in non-EC cell types? What are the critical downstream effectors of GNAQ that cause disease progression, and can they be specifically targeted in affected skin, brain, and eye tissue? We desperately need better models that evaluate transcriptional changes in PWB/SWS to answer these questions and to provide platforms for therapeutic drug development.

8. ACKNOWLEDGEMENTS

The authors would like to thank the following organizations for their generous support: IQVIA, the National Center for Advancing Translational Sciences (NCATS), the National Institute for Neurological Disorders and Stroke (NINDS), the Sturge Weber Foundation (SWF), and the UCI Health Beckman Laser Institute & Medical Clinic. The authors would also like to thank Emily Neubert for assistance with BioRender.

9. SUPPORTING ORGANIZATIONS

The Sturge Weber Foundation serves as a resource for patients, families, philanthropists, researchers, and clinicians of PWB/SWS [32]. Additionally, the National Organization for Rare Disorders (NORD) and the Genetic and Rare Diseases (GARD) Information Center both aim to increase access to rare disease information for the general public in the hope of driving translational development [141,142].

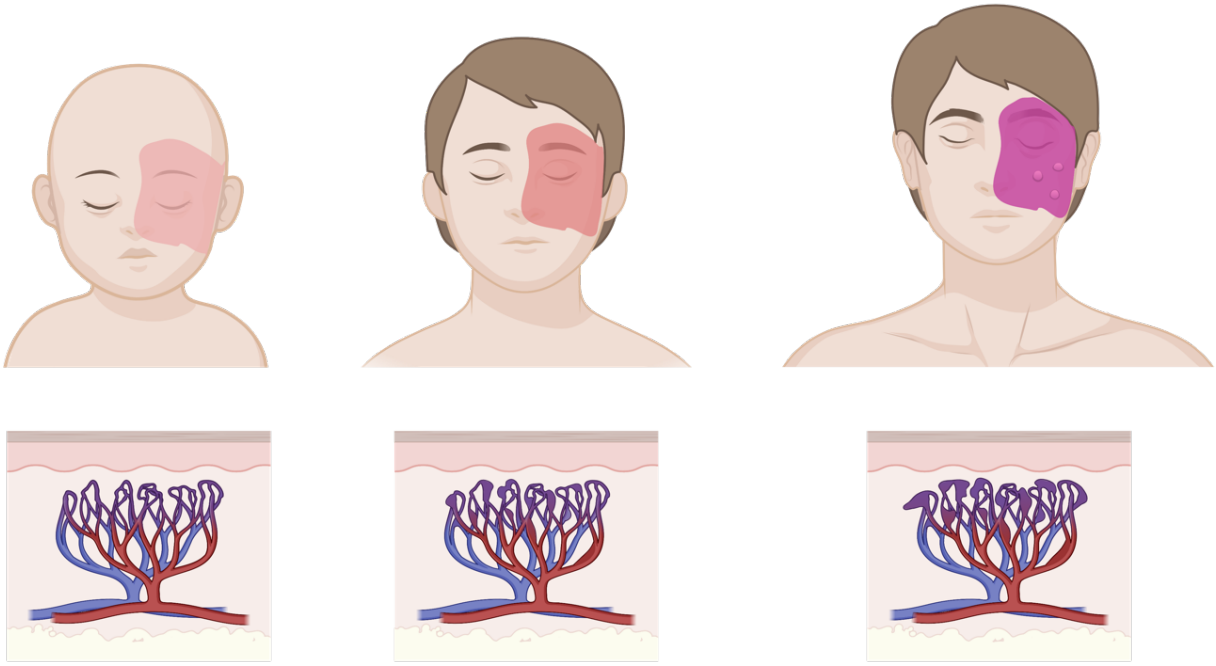

FIGURE 1.2: Age progression of cutaneous PWB.

Birthmark is usually apparent from birth as a light pink patch that can get darker with age, corresponding to progressive dilation of affected capillaries in the dermis. Patients in adulthood may develop soft tissue hypertrophy or nodularity in the absence of clinical intervention. Images created using BioRender.

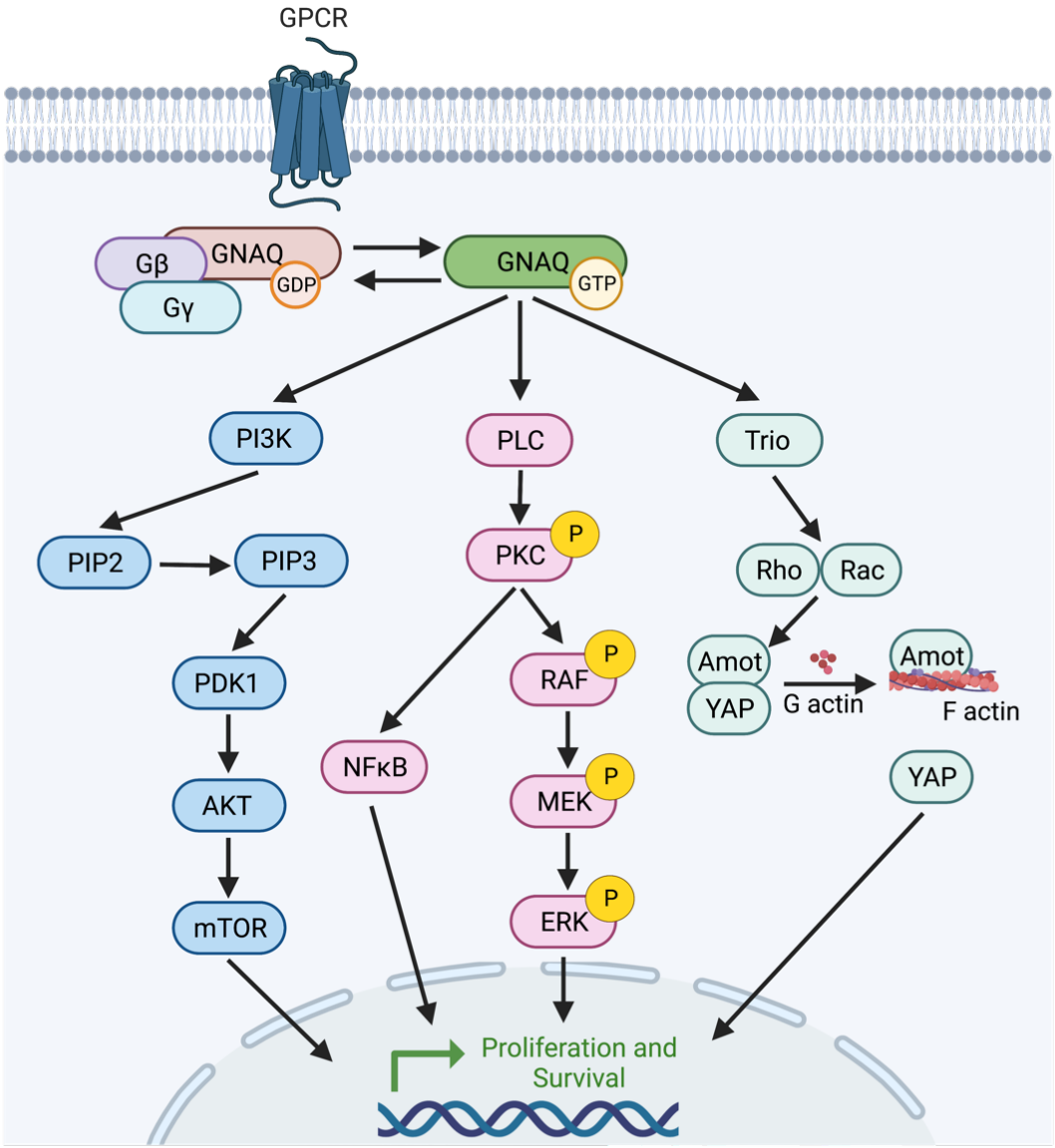

FIGURE 1.3: Selection of predicted downstream targets of GNAQ.

GNAQ can activate PI3K leading to mTOR activation stimulate the MAPK pathway, or activate non-canonical Hippo signaling through Rho/Rac. How GNAQ* leads to vessel instability and PWB/SWS disease progression is poorly understood. Image created using BioRender.

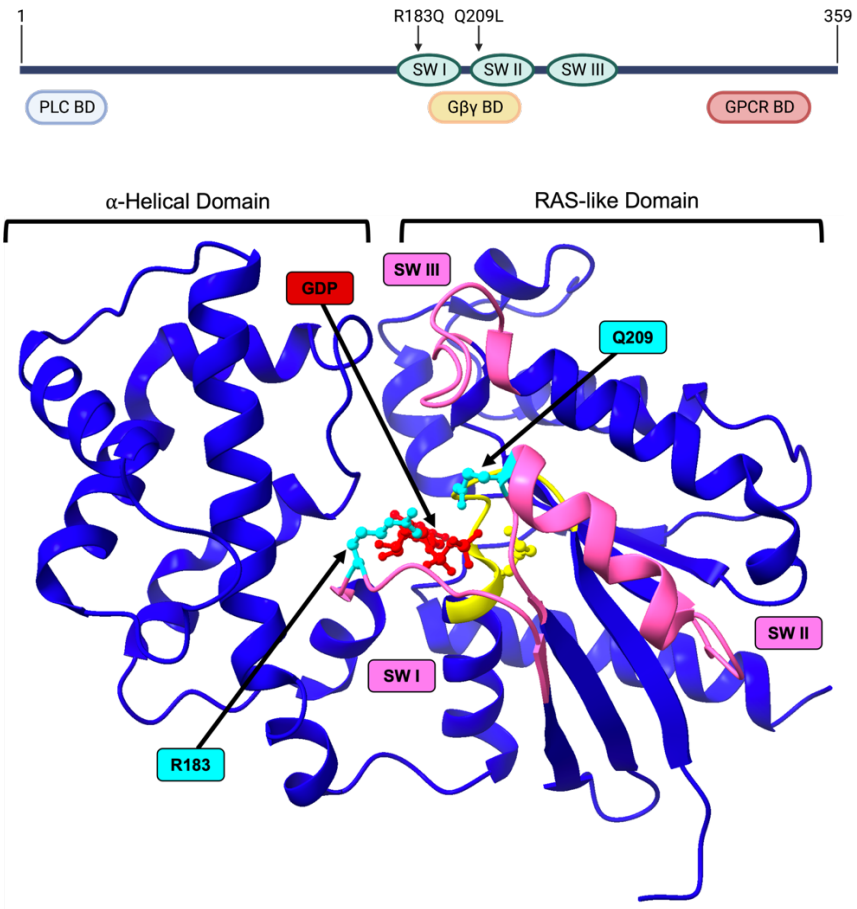

FIGURE 1.4: Map and Crystal Structure of GNAQ.

GNAQ has 3 switch regions (SW): switch regions I and II are part of the GTP binding cleft and have a RAS-like domain for GTP hydrolysis; all three switch regions have key sites for extrinsic regulation by G protein signaling modulators. The p.R183Q and p.Q209L activating mutations are present in switch regions I and II, respectively. GNAQ has a binding domain (BD) for PLC effector function, a binding domain that interacts with the Gβγ subunit during the “off” state, and a GPCR binding domain. Crystal structure (PDB ID: 4GNK) with GDP (red) docked in binding cleft and p.R183Q and p.Q209L mutations (cyan). P loop region with Walker A motif shown in yellow. Switch (SW) I, II, and III shown in pink. Top image created using BioRender. Molecular graphics

performed with UCSF ChimeraX, developed by the Resource for Biocomputing, Visualization, and Informatics at the University of California, San Francisco, with support from National Institutes of Health R01-GM129325 and the Office of Cyber Infrastructure and Computational Biology, National Institute of Allergy and Infectious Diseases.

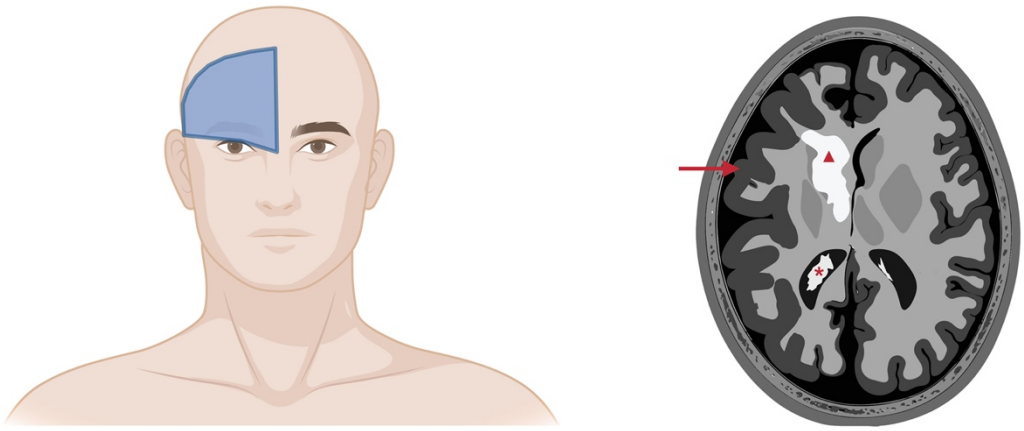

FIGURE 1.5 SWS involvement of brain.

Left panel: Cutaneous PWB in the frontal placode is the best predictor of SWS involvement of eyes and/ or brain. A birthmark in this area is a more reliable suggestion of syndromic potential than PWB distributed along the trigeminal nerve. Right panel: artistic rendering of SWS complications in brain. Red triangle: cerebral calcification. Red arrow: leptomeningeal thickening and cerebral atrophy. Red asterisk: enlarged choroid plexus. Images created using BioRender.

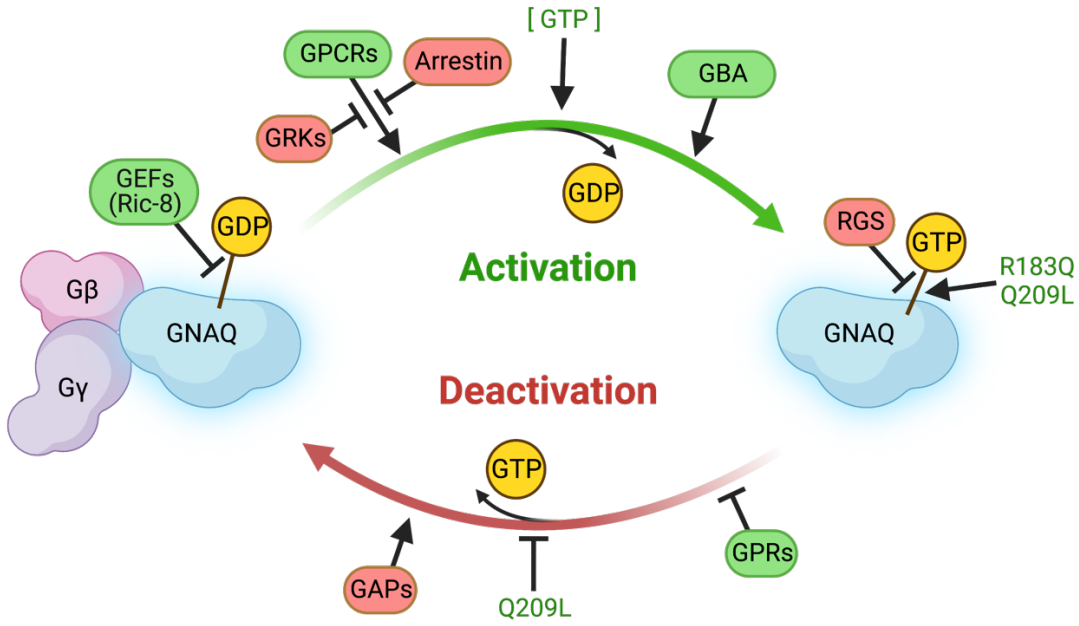

FIGURE 1.6: Summary of regulators of GNAQ signaling.

GEFs, GPCRs, GBA proteins, and GPRs promote GNAQ-GTP “on” signaling and/or delay GTP hydrolysis. Arrestin, GRKs, RGS, and GAPS slow activation of GNAQ, stimulate GTP hydrolysis, and/or stabilize the GNAQ-Gβγ complex. The p.R183Q and p.Q209L strongly stabilize GNAQ-GTP binding and the p.Q209L mutation impairs intrinsic GNAQ GTPase activity. Image created using BioRender.

CHAPTER 2: Modifications to MPS to achieve physiological shear stress and the synthetic fibroblast transcriptome

ABSTRACT

To improve upon the original MPS iteration developed by our lab and increase its applicability to research a broader collection of tissues and diseases, we sought to alter the design of the MPS tissue chip. In particular, there were several areas identified for improvement: the size of the tissue chamber, the characteristics of fluid flow in the microfluidics, and the kind of stromal cells used to support vessel development. In the end, we improved the tissue chamber shape as well as the media reservoirs and channels in ways that support the growth of larger microvascular tissues under physiologically relevant mechanical shear stress. Efforts were unsuccessful to meaningfully alter stroma using the activin A signaling pathway to increase secretion of beneficial extracellular matrix proteins and decrease proliferation or pro-inflammatory activation. Please note that this chapter of the defense is not prepared for publication in a journal manuscript, but aspects of this research are incorporated into manuscripts within Chapters 3 and 4.

INTRODUCTION

In this section, we explore several ways in which we sought to improve upon the existing MPS technology by re-evaluating the structural design of the MPS device as well as potential techniques to modify the behavior of stromal cells in the system. The current MPS schematic, seen in Chapter 1's introduction, is comprised of three diamond shaped tissue chambers that are connected as one unit. We identified several areas to target for improvement, including the size and number of tissue chambers per unit, the

user's control over fluid flow in the microfluidic sections, and performance of detrimental stroma.

Firstly, we aimed to redesign the schematic of the MPS to include a larger tissue chamber to increase fluid flow. Many researchers use large tissue chambers to investigate normal and disease vessel biology and we hypothesized that altering the tissue chambers in the original model to that seen with other published models would provide enough space to grow bigger vessels [143–145]. In particular, we were interested in growing capillary malformations (like those seen in Chapter4) and AVMs and believed that a larger tissue chamber was required to fully allow atypical vasculature to have enough space to form. Additionally, predicted computational modeling of fluid flow through vessels in the original MPS design only predicted shear stress values of approximately 1 dyne per cm^2 or lower. This level of shear stress is below the force that EC would typically experience in vivo and may be altering the microenvironment in a way that obfuscates vessel patterning and signaling pathways [146,147]. Additionally, some disease states require aberrant flow sensing machinery as hallmarks of disease, which would not be possible without adequate levels of interstitial pressure and luminal fluid velocity [148]. Therefore, we sought to redesign the microfluidics in a way that would allow the user to increase the amount of media in the media reservoirs of the 96-well plate; since the MPS is fed by a gravity-driven hydrostatic media head, by increasing the media height of the higher pressure arteriole-like side of the MPS unit, one could increase the amount of fluid pressure and velocity (and thus, shear stress) that the EC would experience.

The modifications to the MPS design were conducted in tandem with experimentation with the normal human lung fibroblasts (NHLF) stromal cells included in the tissue chamber. As previously discussed in Chapter 1, these cells play a key role in assisting network formation during vasculogenesis. These primary stromal cells remodel the fibrin hydrogel, secrete growth factors and other signaling cues, and provide structural support to the developing and maturing vessels, as shown by us and others [6,8,11].

In order to characterize the functionality of these cells in an MPS device, a previous graduate student has identified expression of several key genes as predictors of beneficial stroma [11,12]. Namely, the signature of high expression of Col1A1, SPARC, BIGH3 (TGFBI), and IGFPB7 and low gene expression of PCOLCE indicate strong production of favorable extracellular matrix proteins and reduced proliferation and inflammatory signaling. Due to lot-to-lot variation in function of NHLF purchased from Lonza, we have incorporated a screening approach to evaluate new lots.

While the NHLF are crucial to the formation and maintenance of the vasculature, nonetheless, NHLF activity also sometimes leads to the demise of the MPS tissue chamber, either through over proliferating and out-competing EC in the tissue chamber or outer channels, or by over-degrading the structural integrity of the fibrin hydrogel. We sought to reverse these adverse effects using pro-synthetic strategies used for stroma in wound healing models. The activin A signaling pathway plays a key role in activating the TGFβ wound healing process that leads to tissue repair instead of tissue fibrosis or scarring [149,150]. Importantly, this signaling pathway is normally downregulated upon subsequent subculturing *in vitro*. It is our strategy here to explore options to reactivate

this pathway in NHLF to prevent premature tissue chamber collapse by studying the effects of activin A in the cell culture media as well as constitutively activating the pathway using a mutant form of the receptor complex [151].

MATERIALS AND METHODS

Fabrication of Microfluidic Plate

For full details of MPS fabrication, please see methods section in Chapter 3. Briefly, the design for the MPS was created in AutoCAD software and transferred through a series of steps into a PDMS silicone layer. This layer has a transparent PDMS membrane oxygen plasma bonded to the back side of the device layer and a reservoir plate is attached to the top using a flood-coat of PDMS. This reservoir plate was designed in-house using Fusion 360 and printed using a Form Labs Form 3B printer and High Temp V2 resin. The resin is autoclave-stable and should be inert to cell culture reagents.

Cell Culture Maintenance

Normal human lung fibroblasts (NHLF, Lonza) are used between passages 6-10 and are cultured in DMEM (Corning) containing 10% FBS (Gemini Bio). Human umbilical vein endothelial cell (HUVEC) or endothelial colony-forming cell-derived endothelial cell (ECFC-EC) controls were plated with 0.1% gelatin (Sigma Aldrich) coated flasks and EGM-2 (Lonza) and used between passages 6-8. EC without a fluorescence reporter were transduced with lentivirus expressing mCherry (plasmid 27339; Addgene), green fluorescent protein (GFP; plasmid 27340; Addgene), or azurite

(plasmid 36086; Addgene). All cells are cultured in a humidified incubator at 37°C and 5% CO_2.

Transduction of ACVR1B T206D

ACVR1B T206D (Acv) plasmid was created using Vector Builder. Plasmid was isolated and purified using ZymoPURE II Plasmid Maxiprep Kit (Zymo Research). Acv was made into a second generation lentivirus using transfection with Lipofectamine 2000 (Invitrogen) in HEK293T cell line (ATCC) with psPAX2 (plasmid 12260; Addgene) and pCMV-VSV-G (plasmid 8454; Addgene). Lentivirus infectivity determined via P24 ELISA (Takara Bio).

Vasculogenic Assay in MPS:

To load tissue chambers, NHLFs (Lonza) and ECs are harvested and resuspended in fibrinogen solution at a cell line-dependent concentration (typically 3×10^6 each cell type per mL). Fibrinogen is prepared by dissolving 95% clottable bovine fibrinogen (Neta Scientific) in EBM2 basal media (Lonza) to a concentration of 8 mg per mL. Fibrinogen solution is diluted to a final concentration of approximately 4.6mg per ml with Collagen-1 (Enzo Life Sciences), fibronectin (MilliporeSigma) dissolved in 1x HBSS (Corning), and aprotinin (MilliporeSigma). The final gel-cell matrix suspension is mixed with thrombin (50U per mL, MilliporeSigma) for a final concentration of 3U per mL, quickly seeded into the microtissue chambers through a gel loading inlet and allowed to polymerize in a 37°C incubator for 15 minutes. Laminin (1mg per mL, Life Technologies) is then introduced into the microfluidic channels through medium inlets and incubated at

37°C for an additional 15 minutes. After incubation, culture medium (EGM-2, Lonza) is placed into the microfluidic channels and medium wells. Medium height in reservoir wells is reset every day to maintain interstitial flow and fresh media is replaced every other day. To evaluate vessel formation, MPS are imaged every other day on a Lionheart FX (Agilent) automated fluorescent microscope using the standard 4x air objective.

Image Analysis (vessel formation and permeability assay/ perfusion test)

Mature vascular networks are challenged for perfusion and/ or permeability using 70kDa fluorophore-conjugated dextran (MilliporeSigma) dissolved in culture media at 50mg per mL. Vessel morphometric analysis was performed using MatLab 2022a and Rapid Editable Analysis of Vessel Elements Routine (REAVER) according to Corliss et al. [152].

RESULTS

Modifications to MPS design

Modifications were made to the traditional 3-diamond shaped MPS design that our lab historically used to include a larger tissue chamber that has higher media flow. These changes are shown in FIGURE 2.1. The new design increases the tissue chamber from 1x2mm to 2x6mm to provide a larger space for a microvessel bed to grow. While the previous design worked for some studies, we hypothesized that this increased space is beneficial for understanding vascular diseases where changes in vessel morphology (particularly large vessel morphology such as that discussed in

Chapter 4 to model port wine birthmark) is a hallmark of disease. Modifications were also made to the microfluidic design by uncoupling the media inlets and outlets from each other. In previous iterations, Media Well A and B were combined as one unit, and Media Well C and D would have been one unit; the only factor driving a difference in fluid flow between each side of the tissue chamber would be the presence of the serpentine resistance channels. Now that each media channel has its own inlet and outlet, four different volumes of media can be added to the plate per MPS unit and the pressure gradient driving media flow through the tissue chamber is established by the combined effect of the differential hydrostatic head and the length of the channel.

Furthermore, the 96-well media reservoir plate was exchanged from a commercially available, bottomless 96-well plate (total height about 1cm) to a plate developed and printed in-house (new total height about 4cm). This added height allows us to increase the volume of media in the high-pressure side of the tissue chamber, thus increasing the fluid flow through the media channels and tissue chamber as hydrostatic head equilibrates.

These alterations to the MPS design allow us to increase the amount of shear stress the EC experience to physiological levels that capillary EC would experience. This topic is further addressed with quantitative measurements in Chapter 3.

Re-programming NHLF with ACVR1B T206D

NHLF frequently cause the death of an MPS device because they over-degrade the structural integrity of the fibrin hydrogel in the tissue chamber (FIGURE 2.2 A) or block media flow by over-proliferating and/or invading the outer microfluidic channels to

squeeze the artery- or vein-like vessels (FIGURE 2.2 B). Addition of Activin A to the cell culture media at 100ng/mL for 48 hours in 2D culture causes an increase in Col1A1, SPARC, BIGH3, and IGFBP7 and a decrease in PCOLCE gene expression relative to untreated controls (FIGURE 2.2 C). Addition of activin A in the MPS model, however, prevented vasculogenesis from forming (data not shown). As a result, we used a lentiviral transduction strategy to strongly express ACVR1B T206D in NHLF to constitutively stimulate the activin A receptor complex (FIGURE 2.2 D-E) without stimulating the activin A pathway in EC.

Transduction of NHLF with ACVR1B T206D does not impair vessel formation. Perfusion of four different NHLF lines with 70kDa dextran (green) does not reveal impaired function of the MPS configuration (FIGURE 2.2 F). The perfusion and longevity of vessel networks were challenged with perfusion of 70kDa dextran over 30 minutes and monitoring of vessel patency over the experimental timeline, respectively (FIGURE 2.2 G-H). No statistical difference was found between NHLF transduced with ACVR1B T206D and untransduced controls.

DISCUSSION

The redesign of the MPS device successfully improves the applicability of the MPS system to model human microvasculature. The larger tissue chamber and improved fluid flow align well with our desired characteristics to model the *in vivo* microenvironment that capillary beds experience. Furthermore, the broad applicability of this MPS design allowed the lab to standardize the MPS configuration for a variety of cancer and organoid projects in a way that allows our research team to investigate

vascular biology in tissue-specific and disease-specific contexts without the confounding influence of variable MPS geometry.

Despite literature suggesting that activation of the Activin A signaling pathway promotes a pro-synthetic and anti-proliferative phenotype in stromal cells in wound healing models, activation of this signaling pathway in our MPS model did not substantively alter the function of the NHLF in a way that improves or prolongs device performance. Due to our simultaneous progress developing iPSC-derived model systems, we decided not to pursue this avenue further as we instead decided to investigate the use of iPSC-derived EC and matched stroma (discussed in the next chapter) for an autologous vascular network. This decision removed our dependence on primary cell lines to make *in vitro* microvessels.

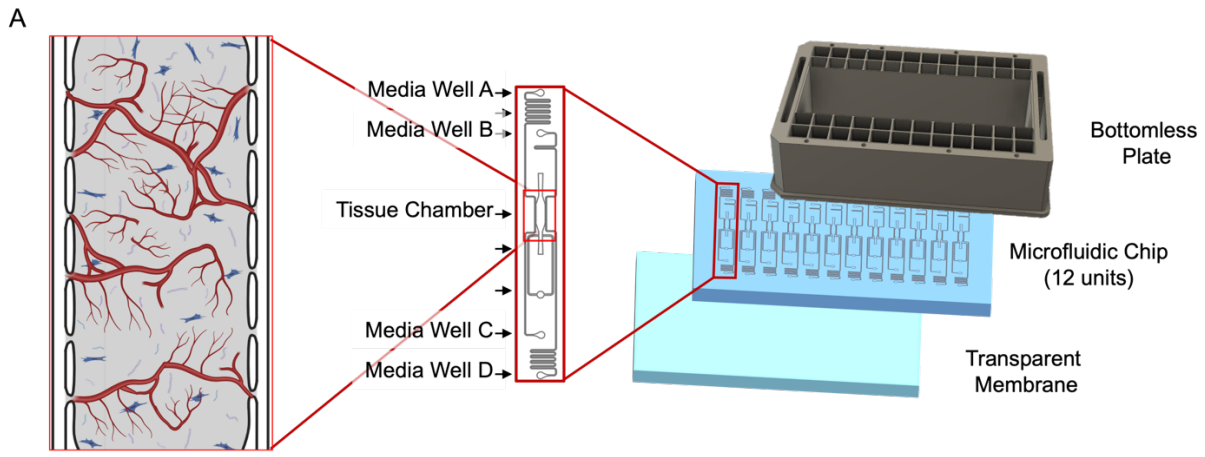

FIGURE 2.1: Modifications to MPS tissue chamber, microfluidics, and media reservoir. (A) Tissue Chamber was redesigned as 2mm x 6mm rectangular tissue chamber. Microfluidics were re-designed so that each media inlet and outlet is controlled by its own media reservoir well. 96-well plate is changed to 3D printed plate made in-house.

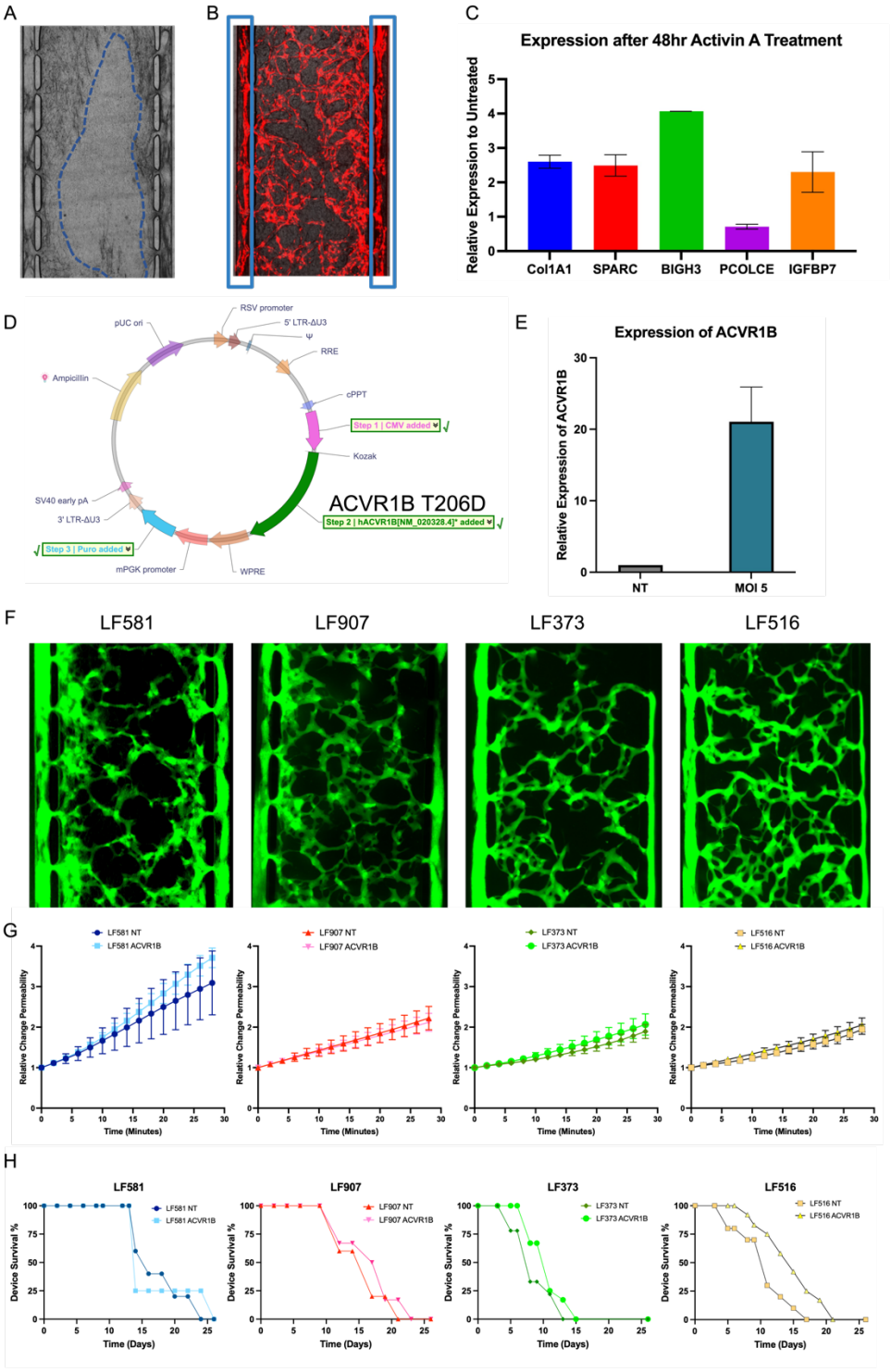

FIGURE 2.2: Attempts to reprogram NHLF to be synthetic.

(A-B) Two issues with NHLF are fibrin hydrogel collapse (A) and media channel pinching (B). (C) Treatment of 100ng/mL Activin A for 48 hours changes gene expression profile of NHLF to synthetic phenotype. (D) Plasmid map of CMV – ACVR1B T206D – puromycin. (E) Transduction of NHLF with ACVR1B T206D at an MOI5 increases expression of ACVR1B approximately 20-fold. (F) Representative perfusion images of 4 NHLF lines. (G) Quantification of permeability images does not indicate increase in vascular permeability of NHLF with ACVR1B T206D. (H) ACVR1B T206D does not prolong tissue chamber health over untransduced controls. qPCR in (C) n=2 for all conditions, (E) n=3. (G) permeability and (H) Meyers-Kaplan experiments LF581 n=3 control, n=4 treatment; LF907 n=5 control, n=6 treatment; LF373 n=5 control, n=7 treatment; LF516 n=5 control, n=8 treatment.

CHAPTER 3: Human iPSC-derived endothelial cells form perfusable microvessels in an autologous vascularized organ-on-chip microphysiological system

William K. Van Trigt[1], Christopher J. Hatch[2], Zee S. Piermatteo[1], Benjamen T. O'Donnell[1], Caleb A. Smeraldi[1], Celeste Sanchez[1], Yu-His Chen[2], Jennifer S. Fang[1,3], Abraham P. Lee[2], Christopher C. W. Hughes[1,2]

1. Department of Molecular Biology and Biochemistry; Charlie Dunlop School of Biological Sciences; University of California Irvine, Irvine, CA, USA
2. Department of Biomedical Engineering; Henry Samueli School of Engineering; University of California Irvine, Irvine, CA, USA
3. Department of Cell and Molecular Biology, School of Science and Engineering, Tulane University, New Orleans, LA, USA

KEYWORDS

iPSC differentiation, engineered tissue, vasculogenesis, microphysiological system, tissue chip, cell culture

ACKNOWLEDGEMENTS

This work was made possible, in part, through access to the following: the UCI Stem Cell Research Center CRISPR and flow cytometry cores, the Genomics Research and Technology Hub Shared Resource of the Cancer Center Support Grant (P30CA-062203), the Single Cell Analysis Core shared resource of Complexity, Cooperation and Community in Cancer (U54CA217378), the Genomics-Bioinformatics Core of the Skin

Biology Resource Based Center (P30AR075047) at the University of California, Irvine and NIH shared instrumentation grant 1S10OD021718-01 (HiSeq 4000). Support for this work was provided by the UCI Stem Cell Research Center and NIH NINDS (5T32NS082174-08), NIH NHLBI (R01 HL149748), and NIH NCATS (UH3TR002137).

ABSTRACT

The discovery of induced pluripotent stem cells (iPSC) ushered in a wave of new hope as researchers predicted the new technology would vastly change the ways in which we could model or treat human diseases. The last 20 years of research, however, have demonstrated that this technology is challenging to adopt, largely due to differences between iPSC lines as well as gaps in successfully differentiating iPSC into adult cell types. Here we lay out the ways in which we have created a novel method for using iPSC in tissue modeling by combining the environment of the VMO with modern differentiation techniques in order to create mature microvessels using iPSC-derived EC. These tissues can be used to create novel disease platforms that capture patient genetic variability and/or replicate *in situ* gene expression of genetic disorders.

INTRODUCTION

Circulatory systems play a crucial role in transporting nutrients, chemical signals, and waste in all tissues of the body. Most blood vessels of the peripheral circulation are composed of three different layers: 1. the outer adventitia, or tunica externa, provides structural support for vessels, 2. the tunica media provides elasticity and its muscular tissue regulates vessel diameter, and lastly 3. the innermost tunica intima layer is an endothelial cell barrier lining the lumen of the vessel [153]. Capillaries, like the tunica intima, are made of a single layer of endothelial cells (EC) and are very thin-walled vessels [153]. It is primarily through these capillary networks that the diffusion between vessels and surrounding tissue occurs.

Vessels play an irreplaceable role in tissue homeostasis and disease. From pro-angiogenic tumor growth to blood brain barrier deterioration in neurodegenerative diseases, there are a variety of conditions that are exacerbated by abnormal vascular involvement. Additionally, blood vessels can cause disease themselves through mutation or injury, like hereditary hemorrhagic telangiectasia or atherosclerosis. The Centers for Disease Control and Prevention estimates that cardiovascular disease and stroke cost the United States economy approximately 1 billion dollars a day in medical costs and lost productivity [154]. Thus, there is an unmet need to treat patients and it is imperative to use vascular models for understanding these normal and disease states.

The rationale for incorporating blood vessel networks in *in vitro* model systems is well-founded, but in practice can be challenging to implement. While simple to study, traditional cell culture methods using 2D techniques preclude the formation of 3D structures like blood vessels and the difference in extracellular matrix stiffness of these model systems versus *in vivo* conditions can greatly perturb the biological function of included cell types [11,12].

Most next-generation cell culture techniques involve organoids or a semi-permeable transmembrane system to include spatial organization with multiple cell types. These have their advantages over 2D culture, however, they are often unvascularized and have limitations in use [22]. EC function in particular is sometimes evaluated using a sprouting assay, where EC-coated microspheres are embedded in static hydrogel and EC form vessel sprouts away from the bead [155,156]. As an evolution from that method, we use a microphysiological system to evaluate this vasculogenesis process. Importantly, as an MPS, this model system is characterized by multiple cell

types (EC and stroma) in a 3D hydrogel that experiences fluid flow. Most *in vitro* systems have one or two of these features, but it is with the combination of all three that one interrogates vessel biology [22]. Furthermore, the resultant tissue is patterned *de novo* by the cells with minimal directional input from researchers, allowing for variation in tissue morphology to occur as a result from disease or therapeutic conditions.

Since the inception of induced pluripotent stem cells (iPSC), researchers have held hope that this novel stem cell type will be able to model individual patient diseases as well as create personalized medicines. Unfortunately, there is much to be desired from current iPSC differentiation methods as differentiation efficiency and, more crucially, the function of the differentiated cells is highly variable. Despite expression of CD31, some stem cell-derived EC show poor vasculogenic capacity as dysfunctional or immature EC [157–164]. In order to evaluate true functional capacity of iPSC-derived EC (iEC), we evaluate tube formation via sprouting assay [155,156] or, more recently, through de novo formation of perfusable vessels in MPS [6–8,10]. Here we combine current iPSC differentiation techniques to create and characterize a novel method for growing autologous *in vitro*, human, iEC microvascular tissue networks.

MATERIALS AND METHODS

Fabrication of Microfluidic Plate

Device fabrication and loading has been described previously [5,15,165]. Briefly, a custom silicon master mold is created using stereolithography, which is transferred to a Sylgard 184 PDMS (Dow Silicones Corporation) replica before creating working molds using polyurethane liquid plastic (Smooth Cast 385, Smooth-On Inc.). A PDMS chip

layer is then replicated from a working mold. Inlets and outlets are punched with a 1.5mm biopsy punching tool while the gel loading inlet, outlet, and burst valve are punched with 1mm biopsy punches. The PDMS chip layer is first attached to a 150μm thin transparent PDMS membrane by treatment bonding with oxygen plasma for 80 seconds. The PDMS layers are then attached to the bottomless reservoir plate (printed using FormLabs Form 3B printer and High Temp Resin V2) by curing a flood-coat of liquid PDMS between the chip layer and plate. The fully assembled platform is placed in a 65°C oven overnight for complete curing before sterilization in an autoclave. The plate is then covered with a clear, sterile 96-well plate polystyrene lid.

Doxycycline-Inducible ETV2 (iETV2) Lentivirus

ETV2 (plasmid 61061; Addgene) coding sequence was inserted into a doxycycline-inducible Gateway backbone (pCW57.1; plasmid 41393; Addgene) using the Gateway LR Clonase II Enzyme kit (Invitrogen). Plasmid was isolated and purified using ZymoPURE II Plasmid Maxiprep Kit (Zymo Research) and confirmed using Sanger sequencing from Retrogen Inc. iETV2 was made into a second generation lentivirus using transfection with Lipofectamine 2000 (Invitrogen) in HEK293T cell line (ATCC) with psPAX2 (plasmid 12260; Addgene) and pCMV-VSV-G (plasmid 8454; Addgene). Lentivirus infectivity determined via P24 ELISA (Takara Bio).

Cell Culture Maintenance

WTC11 (GM25256; Coriell Institute for Medical Research), Edi029-A (Cedars-Sinai Medical Center), and TC012 (University of California, San Diego) were cultured in

mTeSR1 (Stem Cell Technologies) with Matrigel (Corning) coated plates (TABLE 3.1). ReLeSR (Stem Cell Technologies), 10mM ROCK inhibitor (for WTC11 and TC012 only; g-27632, ROCKi; Stem Cell Technologies), and Cryostor CS10 (Biolife Solutions) were used for passaging and cryopreserving. iPSC colonies were transduced overnight with iETV2 lentivirus and 0.8mg/mL polybrene (Santa Cruz Biotechnology) one day before overnight 1µg/mL puromycin (MilliporeSigma) selection. Normal human lung fibroblasts (NHLF, Lonza) are used between passages 6-10 and are cultured in DMEM (Corning) containing 10% FBS (Gemini Bio). Human umbilical vein endothelial cell (HUVEC) or endothelial colony-forming cell-derived endothelial cell (ECFC-EC) controls were plated with 0.1% gelatin (Sigma Aldrich) coated flasks and EGM-2 (Lonza) and used between passages 6-8. EC without a fluorescence reporter were transduced with lentivirus expressing mCherry (plasmid 27339; Addgene), green fluorescent protein (GFP; plasmid 27340; Addgene), or azurite (plasmid 36086; Addgene). All cells are cultured in a humidified incubator at 37°C and 5% CO_2.

Differentiation of iPSC to EC

iPSC were differentiated to EC using reagents and modified protocols from Stem Cell Technologies. iPSC colonies were passaged using ReLeSR to low confluency (5,000 cells/cm^2) in flasks coated with Matrigel using mTeSR1 and 10mM ROCK inhibitor (when appropriate) on Day0, with an emphasis on breaking up colonies into very small clusters of about 5 cells per cluster. The next day and following day(s) (Day1 and Day2+), media was replaced with Mesoderm Induction Media (Stem Cell Technologies). EC Differentiation was achieved by adding on each day Endothelial

Induction Media (Stem Cell Technologies) with 1µg/mL Doxycycline (MilliporeSigma) to induce ETV2 transient expression. Duration in Mesoderm Induction Media and Endothelial Induction Media were each optimized per cell line. Following the conclusion of EC Induction, cells were trypsinized (0.05%; Gibco) and plated into new flasks coated in Animal Component-Free Cell Attachment Substrate (Stem Cell Technologies) in PHEC+ media, comprised of M199 basal media (Gibco), 20% heat-inactivated Fetal Bovine Serum (VWR), 1mg/mL Endothelial Cell Growth Supplement (ECGS; Life Technologies), and 10ng/mL VEGFA-165 (Shenandoah Biotechnology). If necessary, EC were purified with CD31 magnetic separation (MACS).

Characterization of iPSC-EC by flow cytometry:

Single cell suspensions of $1x10^6$ cells in FACS tubes were rinsed briefly fixed with 4% paraformaldehyde for 15 minutes before permeabilization with 0.1% triton X-100 in DPBS. Cells were stained with antibody (BD Biosciences, TABLE 3.2) and analyzed with a BD Fortessa flow cytometer. Results were analyzed with FCS Express 7, using isotype matched controls and anti-mouse compensation beads (Invitrogen) for gating and compensation, respectively.

Vasculogenic Assay in MPS:

To load tissue chambers, NHLFs (Lonza) and ECs are harvested and resuspended in fibrinogen solution at a cell line-dependent concentration (typically 3×10^6 each cell type per mL). Fibrinogen is prepared by dissolving 95% clottable bovine fibrinogen (Neta Scientific) in EBM2 basal media (Lonza) to a concentration of 8 mg per

mL. Fibrinogen solution is diluted to a final concentration of approximately 4.6mg per ml with Collagen-1 (Enzo Life Sciences), fibronectin (MilliporeSigma) dissolved in 1x HBSS (Corning), and aprotinin (MilliporeSigma). The final gel-cell matrix suspension is mixed with thrombin (50U per mL, MilliporeSigma) for a final concentration of 3U per mL, quickly seeded into the microtissue chambers through a gel loading inlet and allowed to polymerize in a 37°C incubator for 15 minutes. Laminin (1mg per mL, Life Technologies) is then introduced into the microfluidic channels through medium inlets and incubated at 37°C for an additional 15 minutes. After incubation, culture medium (EGM-2, Lonza) is placed into the microfluidic channels and medium wells. Medium height in reservoir wells is reset every day to maintain interstitial flow and fresh media is replaced every other day. To evaluate vessel formation, MPS are imaged every other day on a Lionheart FX (Agilent) automated fluorescent microscope using the standard 4x air objective.

Image Analysis (vessel formation and permeability assay/ perfusion test)

Mature vascular networks are challenged for perfusion and/ or permeability using 70kDa fluorophore-conjugated dextran (MilliporeSigma) dissolved in culture media at 50mg per mL. Vessel morphometric analysis was performed using MatLab 2022a and Rapid Editable Analysis of Vessel Elements Routine (REAVER) according to Corliss *et al.* [152].

Comsol Fluid Analysis

Images of tissue chambers were converted into a binary image and imported into AutoCAD in order to map the vessel morphometry. This file was then exported into Comsol and fluid pressure inputs were applied to the media inlets and outlets based on media height in the media wells at the beginning of media flow. Output measurements of Comsol are fluid velocity and shear stress on the vascular wall.

Immunofluorescent microscopy:

MPS were fixed by perfusing 4% paraformaldehyde through the media channels of each device for 30 minutes. The bottom PDMS membrane was peeled from the device layer and each tissue chamber was manually excised and placed tissue-side down in a 24 well plate for staining. Tissues were washed 3 times for 5 minutes with DPBS on a gentle rocker before permeabilization for 30 minutes with 0.1% Triton-X 100 in DPBS. Tissues were blocked for 1 hour at room temperature in 0.1% Triton-X 100 with 5% FBS and 1% donkey serum before overnight incubation at 4°C with primary antibody in DPBS (TABLE 3.2). Tissue chambers were washed 3 times for 5 minutes with DPBS before 1 hour staining of secondary antibody. DAPI served as a nuclear stain and isotype controls were used as negative staining controls.

Bulk RNA Sequencing

Samples were sent to the UCI Genomics and Research Technology Hub (GRTH) for bulk RNA Illumina sequencing. Samples were prepared in house using the Zymo Quick RNA Mini-Prep kit and were evaluated on a nanodrop for purity and concentration

before submission to the GRTH. Future experiments will use this data for deeper understanding of each iPSC-derived EC line.

Single-Cell RNA Sequencing:

Media was aspirated from each well and the bottom membrane was gently peeled off the device to expose the tissue chambers. Tissues were washed with 500μL of DPBS. To each, 100μL of TrypLE (Gibco) was added as a droplet on top of the chamber and incubated for 5 min. After digestion, tissue chambers were transferred into a 15mL conical tube with EGM2 and centrifuged at 300×g for 5 min at 4°C to pellet single cells and whole tissues. Media was carefully aspirated and 200U collagenase III in 1mL DPBS was added to the undigested tissues. After gentle pipetting, the solution was allowed to sit for 2 min at room temperature before pipetting gently again to dissociate the gel. Digestion mix was washed with 10mL of EGM2 and centrifuged at 300×g for 5 minutes at 4°C. Cells were resuspended into DPBS with 1% human serum albumin and passed through a moist 70μm filter by spinning at 200×g for 1 min. Cells were counted and volume was adjusted so that total cells were at a concentration of 1000 cells per μL.

Suspensions were loaded onto a Chromium Single Cell Instrument (10× Genomics) to generate single cell gel beads in emulsion (GEMs). GEMs were processed to generate cDNA libraries by using 10× Genomics v2 chemistry according to the Chromium Single Cell 3′ Reagent kit v2 user guide: CG00052 Rev B. Quantification of cDNA libraries was performed using Qubit dsDNA HS Assay kit (Life Technologies Q32851), high-sensitivity DNA chips (Agilent 5067-4626) and KAPA qPCR (Kapa

Biosystems KK4824). Libraries were sequenced on an Illumina NovaSeq6000 to achieve an average of 50,000 reads per cell.

FASTQ files for each library were aligned to an indexed GRCh38 reference genome using Cell Ranger (10× genomics) Count 3.1.0 to generate count matrices. Count matrices were loaded into RStudio (1.2.5042 version, R version 4.0.4 [166,167]) and converted into a Seurat object using the Seurat R Package (version 4.0.0.9015 [168,169]). Cells containing more than 15% mitochondrial RNA or with less than 200 features were removed. Additionally, genes not detected in at least 3 cells were trimmed. Data were normalized, the 2000 top variable features were found, and scaled using the NormalizeData, Find VariableFeatures, and ScaleData functions, respectively. Data were further normalized using the SCTransform function and the difference between cells in the S phase and G2M phase was regressed to help distinguish non-cycling from cycling cells. Doublets were identified and removed using the DoubletFinder R package (version 2.0.3 [170]). A modified version of the chooseR R package was used to generate silhouette scores for selecting the resolution [171]. Clusters were labeled based on the expression of known markers (ECs: PECAM1, CDH5, VWF, KDR, CLDN5 [172]; fibroblasts: PDGFRα, PDGFRβ, COL1A1 [173]; stroma: PDGFRβ, TPM1, ACTA2 [174]; cycling cells: MKI67 and TOP2A. Heatmaps were generated by filtering expression for each clustering by log2 fold change. Pathway analysis was performed using clusterProfiler with the GO Biological Process 2021 database on the top 100 differentially expressed genes [175]. The significance of key pathways was directly compared for each dataset.

Individual libraries were integrated using the scMC Run- scMC R function and package (version 1.0.0) with default settings [176]. scMC removes the technical variation while preserving biological variation using variance analysis in an unsupervised manner. For integration, the 'RNA' slot was used for each library. After integration, cell types were assigned to individual cells based on the analysis of the individual libraries. UMAP for all the datasets was generated with palette from the Polychrome R package (version 1.5.1) [177].

RESULTS

Differentiation of iPSC to EC

EDi029-A, WTC11, and TC012 (see TABLE 1 for cell line info) iPSC were transduced with iETV2 lentivirus and differentiated using a modified protocol from Stem Cell Technologies (FIGURE 3.1 A-B). Duration of differentiation was determined for each line by evaluating the maximum percentage of CD31 expressing EC at the end of differentiation procedure. Additionally, dox-induced expression of ETV2 during EC induction period was used to improve the differentiation of mesoderm into EC, as described by others [157,158]. ETV2 is uniquely expressed during EC induction period upon addition of 1µg per mL dox to culture media (FIGURE 3.1 C). CD31 expression of differentiated cells varies from 55 percent (EDi029-A iEC) to 75 percent (WTC11 iEC) (Figure 3.1 D).

Formation of iPSC-EC vasculature in MPS

The MPS microfluidic design for this study was altered from previously published models to feature a larger tissue chamber and 3D printed media reservoir plate (FIGURE 3.2 A) [13,15,18,27]. iEC and stromal cells as single cells suspended in fibrin hydrogel are quickly mixed with thrombin and added through the gel loading inlet (GLI) before clotting in the tissue chamber (FIGURE 3.2 B). Media is placed in the media inlet and outlet wells of reservoir plate so that media pressure is gravity driven from top left to bottom right of tissue chamber via microfluidic channels. The iEC and stroma self-organize into vasculature over approximately 1 week (FIGURE 3.2 C). The iEC polarize and form a primitive vascular network that goes on to lumenize, remodel, and anastomose with the microfluidic media channels. Mature vasculature is challenged using a perfusion test of 70kDa dextran dye through the vascular lumen (FIGURE 3.2 D). COMSOL modeling of media velocity through the tissue chamber corresponds to iEC shear stress values between 1 and 3 dynes per cm^2, with some values reaching as high as 7 dynes per cm^2 (FIGURE 3.2 E). Representative images of WTC11 iEC and EDi029A iEC are shown in FIGURE 3.2 F and 3.2 G, respectively.

DISCUSSION

Here we lay out the successful creation of an iPSC-derived vascular model that is an appropriate tool for studying genetic vascular diseases. Ongoing work will identify how the iEC respond to shear stress through transcriptomic analysis of both bulk RNA sequencing as well as single cell RNA sequencing. We hope to identify key ways in which the VMO recapitulates the *in vivo* environment required for maturing iEC into functional EC better than alternative cell culture methods.

The model described here is further expanded upon in the next chapter to evaluate the effects of GNAQ somatic mutations on vascular development in a model of Port Wine Birthmark.

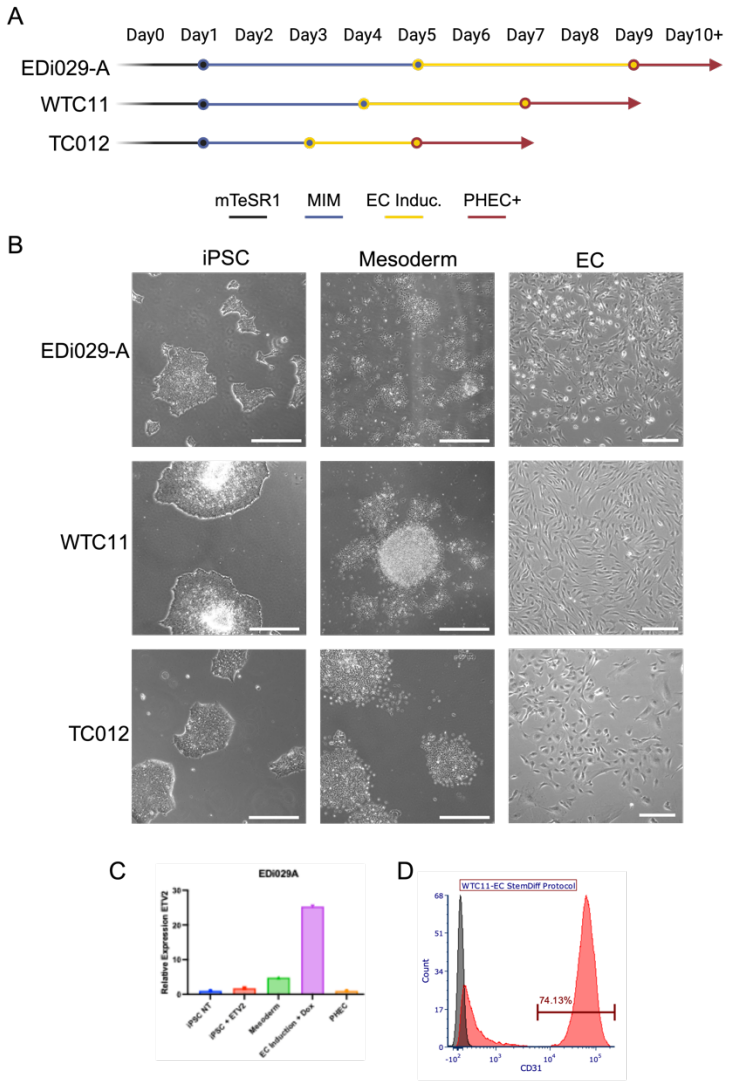

FIGURE 3.1: Multi-stage differentiation of iPSC to EC.

(A) iPSCs are differentiated to a mesoderm intermediate, induced to EC through transient ETV2 expression, and matured in PHEC+ before vasculogenic assays. Duration of steps determined for each cell line based on CD31 purity. MIM mesoderm induction media. (B) Morphology changes during differentiation stages. Scale bars iPSC and mesoderm 250μm, scale bars at EC 25μm. (C) Representative qPCR analysis of ETV2 expression in WTC11. Dox-induced expression of ETV2 transcripts detected during EC induction step. (D) Representative expression of CD31 of WTC11 in PHEC+ at end of differentiation.

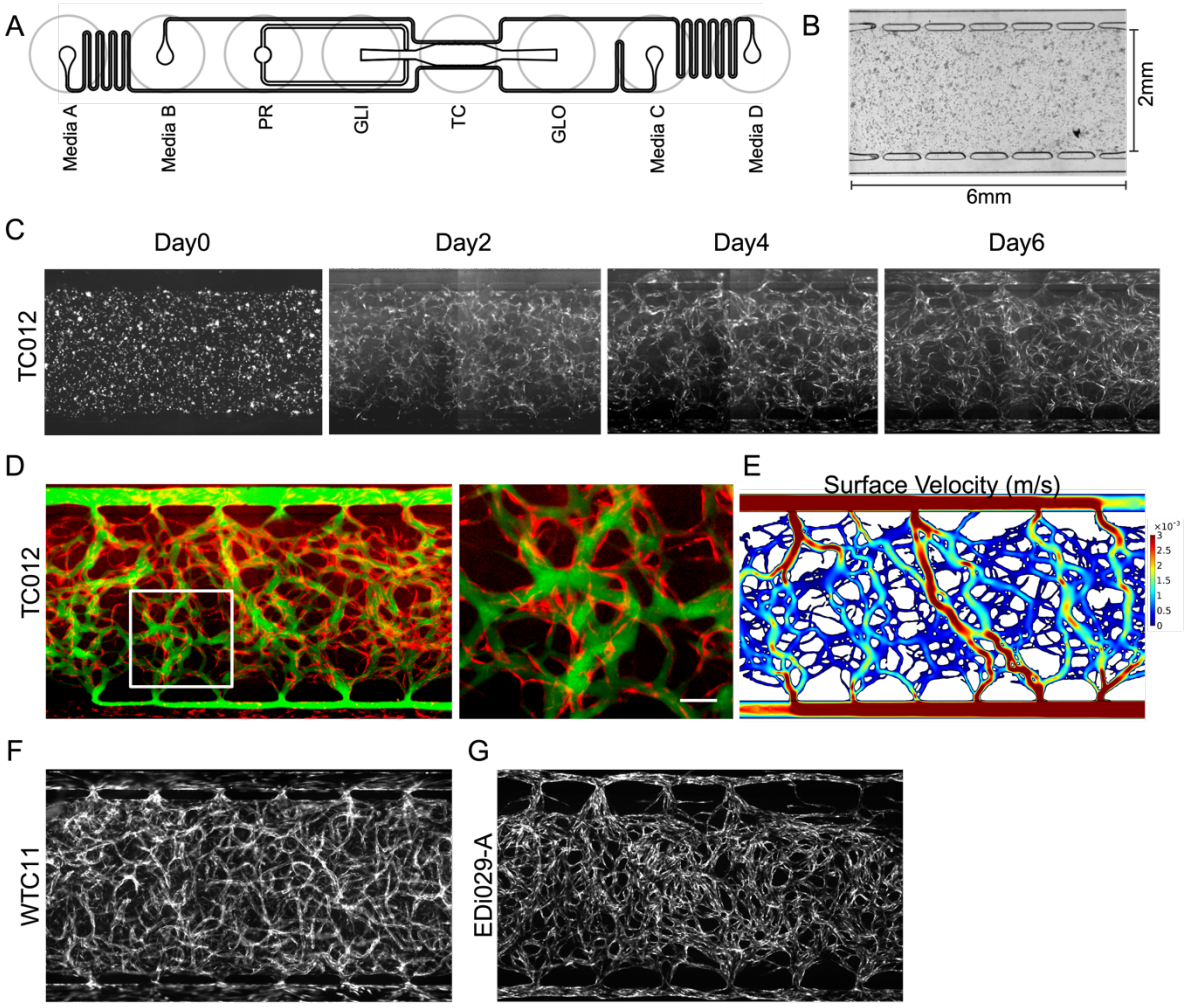

FIGURE 3.2: Organ-on-Chip MPS design grows iEC perfusable microvessels.

(A) Schematic of microfluidic design. iEC and stroma are loaded in fibrin hydrogel through gel loading inlet (GLI) through the tissue chamber (TC) towards the gel loading outlet (GLO). The pressure regulator (PR) serves a burst valve to prevent overloading of chamber. Media is placed in reservoirs A (1mL), B (1.3mL), C (120µL), and D (540µL) to create a hydrostatic pressure gradient from top left of tissue chamber to bottom right. (B) Brightfield image of tissue chamber loaded with iEC and stroma on Day0. Tissue chamber is 6mm x 2mm x 200µm (xyz). (C) iEC transduced with fluorescent reporter allows easy visualization of vasculogenesis in tissue chamber. (D) The mature vascular

network on Day6 is challenged with 70kDa fluorescent dextran (green) to media well B and allowing it to perfuse through the lumen of the iEC microvessels (red). High magnification insert of perfusable microvessels, scale bar 100μm. (E) COMSOL modeling of perfusion velocity through vascular network. (F-G) Representative examples of mature microvessel MPS with WTC11 and EDi029-A iEC (white).

SUPPLEMENTARY FIGURES

TABLE 3.1: iPSC cell line information.

WTC11 and EDi029-A were purchased for research use. TC012 was obtained via a collaboration with Dr. Maike Sander at University of California, San Diego.

Cell Line	Vendor	Donor Source	Donor Demographics	Reprogramming Method	Comment(s)
WTC11	Coriell Institute for Medical Research	Dermal Fibroblasts	30yr asian male	Non-integrating episomal	Clone 6, eGFP Alias GM25256, UCSFi001-A-6 (RRID:CVCL_IR32)
EDi029-A	Cedars-Sinai Medical Center	PBMC	80yr caucasian male	Non-integrating episomal	RRID:CVCL_YB22
TC012	N/A	PBMC	unknown	unknown	

TABLE 3.2: Antibody Information used for flow cytometry and immunofluorescence staining.

Marker	Vendor	Catalog Number
c-Kit	BD Pharmigen	555714
CD31	BD Pharmigen	563652
CD31	Dako	M0823
CD31	BD Pharmigen	562855
CD34	BD Pharmigen	562577
CD45	BD Pharmigen	560178
PDGFRα	Biolegend	323508
PDGFRβ	BD Pharmigen	564124
PDGFRβ	Invitrogen	MA5-15143
Sox2	Invitrogen	50-9811-82
VE-Cadherin	BD Pharmigen	561714
VEGFR2	BD Pharmigen	560495
Donkey anti-Mouse	Invitrogen	A10037
Donkey anti-Rabbit	Invitrogen	A31573

CHAPTER 4: An activating Gnaq R183Q mutation drives port wine birthmark lesion formation in a vascularized organ-on-chip microphysiological system

Van Trigt, William K.[1], Hatch, Chris J.[2], Piermatteo, Zee S.[1], Ewald, Makena L.[1], Fang, Jennifer S.[1,3], Kelly, Kristen M.[4], Hughes, Christopher C W.[1]

1. Department of Molecular Biology and Biochemistry; Charlie Dunlop School of Biological Sciences; University of California Irvine, Irvine, CA, USA
2. Department of Biomedical Engineering; Henry Samueli School of Engineering; University of California Irvine, Irvine, CA, USA
3. Department of Cell and Molecular Biology, School of Science and Engineering, Tulane University, New Orleans, LA, USA
4. Department of Dermatology; School of Medicine; University of California Irvine, Irvine, CA, USA

LIST OF ABBREVIATIONS

PWB: Port wine birthmark

EC: endothelial cell

CM: capillary malformation

SWS: Sturge-Weber syndrome

GNAQ: guanine nucleotide-binding protein subunit alpha Q

MPS: microphysiological system

GEF: GTP exchange factor

VMO: vascularized micro organ

ECFC-EC: endothelial colony forming cell- endothelial cell

HUVEC: human umbilical vein endothelial cell

iPSC: induced pluripotent stem cell

iEC: induced pluripotent stem cell-derived endothelial cell

ACKNOWLEDGEMENTS

This work was made possible, in part, through access to the following: the Genomics Research and Technology Hub Shared Resource of the Cancer Center Support Grant (P30CA-062203), the Single Cell Analysis Core shared resource of Complexity, Cooperation and Community in Cancer (U54CA217378), the Genomics-Bioinformatics Core of the Skin Biology Resource Based Center (P30AR075047) at the University of California, Irvine and NIH shared instrumentation grant 1S10OD021718-01 (HiSeq 4000). Support for this work was provided by the UCI Stem Cell Research Center and NIH NINDS (5T32NS082174-08), NIH NHLBI (R01 HL149748), and NIH NCATS (UH3TR002137).

ABSTRACT

Port-wine birthmark (PWB) is a progressive, congenital blood vessel disease that affects roughly one in 350 people and manifests as a light pink patch on the face or neck that can darken with age and develop soft tissue hypertrophy or nodularity. A portion of PWB patients have vascular lesions that are not superficial, affecting dentition, eyes, and/ or brain tissues and causing a variety of neurological and cognitive deficits called Sturge-Weber Syndrome (SWS). Most superficial PWB is resolved with pulsed-laser therapy during the first decade of life; deeper vascular lesions and some skin lesions, however, are difficult to treat and developing new therapeutic strategies has stalled over the last few decades. Several hurdles to therapeutic progress include poor understanding of disease biology and limited *in vitro* and *in vivo* models of PWB.

Port-wine birthmarks are caused by endothelial somatic mutations within the Gnaq protein's GTP hydrolysis site, which likely over-activates downstream growth and survival pathways of the endothelial cells containing a GNAQ mutation. We have used a multidisciplinary, translational approach to develop a microphysiological model of PWB lesions using our *in vitro* vascularized micro-organ (VMO) platform.

Here we lay out our progress developing an autologous model of *in vitro* vasculogenesis for the study of PWB. We can recapitulate in this model using GNAQ-mutant vasculature the formation of dilated vascular lesions seen in patients. Through single cell transcriptome analysis of PWB patients and this model system, we additionally identify overexpression of BMP2 in PWB mutant EC as potential drivers of vascular lesion formation. Future experiments plan to leverage this novel mechanism for the discovery of effective therapeutics.

INTRODUCTION

Preliminary effort to make an *in vitro* vascularized model of port wine birthmark aimed to introduce mutant GNAQ* to primary, healthy endothelial cell colony-forming cells (ECFC) via lentivirus transduction. That work is laid out here in the following section. Please see background info below for preliminary work not included in this manuscript.

Lentivirus introduces constitutively active mutant or control GNAQ

We created lentiviral constructs using cold fusion to introduce wild-type GNAQ (GNAQ-WT) and R183Q GNAQ (GNAQ*-R183Q) to ECFC (FIGURE 4.1 A). Empty vector (EV) control lentivirus was created using the empty backbone with no gene insertion. The GNAQ sequences were purchased from Addgene; the final plasmids were analyzed by Sanger sequencing to confirm integration of sequences of interest prior to creation of lentivirus. qPCR analysis of primary ECFC transduced with a titer of lentivirus was used to determine the optimal amount of virus to use for future experiments (FIGURE 4.1 B). Gene expression measures the combined expression of GNAQ introduced from lentivirus as well as GNAQ from native alleles. To achieve *in vivo* ratio of mutation burden, we proceeded with viral dilutions that would double the expression of total GNAQ in the EC, reflecting the heterozygous expression of mutant – to – wild type GNAQ in patients.

GNAQ*-R183Q impairs EC migration but not proliferation

We were interested if PWB vascular lesion formation is in part due to GNAQ*-R183Q effects on migration or proliferation rate. It is possible that vascular lesions form and slowly progress due to clustering of mutant cells with undesired proliferation. A scratch assay was performed to evaluate migration capacity (FIGURE 4.1 C). ECFC transduced with control and mutant lentivirus were plated 2 days post-transduction. The cell culture surface was scratched with a P1000 pipette tip, and cells were allowed to regrow into the area for 24 hours. ECFC transduced with GNAQ*-R183Q lentivirus displayed a reduction in migration capacity compared to EV and GNAQ-WT controls. A proliferation assay was performed 48 hours post-transduction to identify if mutant GNAQ increases proliferation rate (FIGURE 4.1 D). EdU incorporation in all samples did not detect a statistically significant difference between conditions.

GNAQ*-R183Q ECFC form hyperdense vascular networks that progressively dilate

ECFC transduced with GNAQ-WT control and GNAQ*-R183Q lentivirus form vascularized networks by Day10 (FIGURE 4.2 A-B). These networks are anastomosed with the media channels and are perfusable with 70kDa dextran dye. Morphogenic analysis of vascular networks (FIGURE 4.2 C) identified trends towards increased branch length and vessel density in mutant networks, suggesting a hyperdense vascular phenotype similar to that seen in very mild patient lesions at birth. By Day21 (FIGURE 4.2 D-E), the vascular networks have continued maturing and remodeling, and small areas of the GNAQ*-R183Q vascular networks indicate areas of dilation (FIGURE 4.2 F).

Transition to iPSC-derived model

The successful MPS data presented in this preliminary section indicated that we were hopeful a PWB model could be created, especially the observation of hyperdense vascular networks that mimic early lesions seen in young patients. We thus desired to continue investigating a model of port wine birthmark using an iPSC-derived system for two reasons: the GNAQ lentiviral transduction seemed to alter the growth characteristics and health of the ECFC post-transduction (the EC seem to be sensitive to total amount of GNAQ expressed, regardless of whether it is WT or R183Q) and we desired a system that would express GNAQ at physiological levels under native gene location and control. This later work with iPSC-EC do not replicate migration deficiencies shown in the previous section but show exacerbated lesion development more similar to PWB severe hallmarks of disease. It is unclear to us at this time if the migration deficiency is an artifact of the previously mentioned cell stress of lentiviral transduction.

MATERIALS AND METHODS

Fabrication of Microfluidic Plate

Device fabrication and loading has been described previously [5,15,165]. Briefly, a custom silicon master mold is created using stereolithography, which is transferred to a Sylgard 184 PDMS (Dow Silicones Corporation) replica before creating working molds using polyurethane liquid plastic (Smooth Cast 385, Smooth-On Inc.). A PDMS chip layer is then replicated from a working mold. Inlets and outlets are punched with a

1.5mm biopsy punching tool while the gel loading inlet, outlet, and burst valve are punched with 1mm biopsy punches. The PDMS chip layer is first attached to a 150μm thin transparent PDMS membrane by treatment bonding with oxygen plasma for 80 seconds. The PDMS layers are then attached to the bottomless reservoir plate (printed using FormLabs Form 3B printer and High Temp Resin V2) by curing a flood-coat of liquid PDMS between the chip layer and plate. The fully assembled platform is placed in a 65°C oven overnight for complete curing before sterilization in an autoclave. The plate is then covered with a clear, sterile 96-well plate polystyrene lid.

Doxycycline-Inducible ETV2 (iETV2) Lentivirus

ETV2 (plasmid 61061; Addgene) coding sequence was inserted into a doxycycline-inducible Gateway backbone (pCW57.1; plasmid 41393; Addgene) using the Gateway LR Clonase II Enzyme kit (Invitrogen). Plasmid was isolated and purified using ZymoPURE II Plasmid Maxiprep Kit (Zymo Research) and confirmed using Sanger sequencing from Retrogen Inc. iETV2 was made into a second generation lentivirus using transfection with Lipofectamine 2000 (Invitrogen) in HEK293T cell line (ATCC) with psPAX2 (plasmid 12260; Addgene) and pCMV-VSV-G (plasmid 8454; Addgene). Lentivirus infectivity determined via P24 ELISA (Takara Bio).

Cell Culture Maintenance

WTC11 (GM25256; Coriell Institute for Medical Research), Edi029-A (Cedars-Sinai Medical Center), and TC012 (University of California, San Diego) were cultured in mTeSR1 (Stem Cell Technologies) with Matrigel (Corning) coated plates (TABLE 3.1).

ReLeSR (Stem Cell Technologies), 10mM ROCK inhibitor (for WTC11 and TC012 only; g-27632, ROCKi; Stem Cell Technologies), and Cryostor CS10 (Biolife Solutions) were used for passaging and cryopreserving. iPSC colonies were transduced overnight with iETV2 lentivirus and 0.8mg/mL polybrene (Santa Cruz Biotechnology) one day before overnight 1µg/mL puromycin (MilliporeSigma) selection. Normal human lung fibroblasts (NHLF, Lonza) are used between passages 6-10 and are cultured in DMEM (Corning) containing 10% FBS (Gemini Bio). Human umbilical vein endothelial cell (HUVEC) or endothelial colony-forming cell-derived endothelial cell (ECFC-EC) controls were plated with 0.1% gelatin (Sigma Aldrich) coated flasks and EGM-2 (Lonza) and used between passages 6-8. EC without a fluorescence reporter were transduced with lentivirus expressing mCherry (plasmid 27339; Addgene), green fluorescent protein (GFP; plasmid 27340; Addgene), or azurite (plasmid 36086; Addgene). All cells are cultured in a humidified incubator at 37°C and 5% CO_2.

Differentiation of iPSC to EC

iPSC were differentiated to EC using reagents and modified protocols from Stem Cell Technologies. iPSC colonies were passaged using ReLeSR to low confluency (5,000 cells/cm^2) in flasks coated with Matrigel using mTeSR1 and 10mM ROCK inhibitor (when appropriate) on Day0, with an emphasis on breaking up colonies into very small clusters of about 5 cells per cluster. The next day and following day(s) (Day1 and Day2+), media was replaced with Mesoderm Induction Media (Stem Cell Technologies). EC Differentiation was achieved by adding on each day Endothelial Induction Media (Stem Cell Technologies) with 1µg/mL Doxycycline (MilliporeSigma) to

induce ETV2 transient expression. Duration in Mesoderm Induction Media and Endothelial Induction Media were each optimized per cell line. Following the conclusion of EC Induction, cells were trypsinized (0.05%; Gibco) and plated into new flasks coated in Animal Component-Free Cell Attachment Substrate (Stem Cell Technologies) in PHEC+ media, comprised of M199 basal media (Gibco), 20% heat-inactivated Fetal Bovine Serum (VWR), 1mg/mL Endothelial Cell Growth Supplement (ECGS; Life Technologies), and 10ng/mL VEGFA-165 (Shenandoah Biotechnology). If necessary, EC were purified with CD31 magnetic separation (MACS).

Characterization of iPSC-EC by flow cytometry:

Single cell suspensions of $1x10^6$ cells in FACS tubes were rinsed briefly fixed with 4% paraformaldehyde for 15 minutes before permeabilization with 0.1% triton X-100 in DPBS. Cells were stained with antibody (BD Biosciences, TABLE 3.2) and analyzed with a BD Fortessa flow cytometer. Results were analyzed with FCS Express 7, using isotype matched controls and anti-mouse compensation beads (Invitrogen) for gating and compensation, respectively.

Vasculogenic Assay in MPS:

To load tissue chambers, NHLFs (Lonza) and ECs are harvested and resuspended in fibrinogen solution at a cell line-dependent concentration (typically 3×10^6 each cell type per mL). Fibrinogen is prepared by dissolving 95% clottable bovine fibrinogen (Neta Scientific) in EBM2 basal media (Lonza) to a concentration of 8 mg per mL. Fibrinogen solution is diluted to a final concentration of approximately 4.6mg per ml

with Collagen-1 (Enzo Life Sciences), fibronectin (MilliporeSigma) dissolved in 1x HBSS (Corning), and aprotinin (MilliporeSigma). The final gel-cell matrix suspension is mixed with thrombin (50U per mL, MilliporeSigma) for a final concentration of 3U per mL, quickly seeded into the microtissue chambers through a gel loading inlet and allowed to polymerize in a 37°C incubator for 15 minutes. Laminin (1mg per mL, Life Technologies) is then introduced into the microfluidic channels through medium inlets and incubated at 37°C for an additional 15 minutes. After incubation, culture medium (EGM-2, Lonza) is placed into the microfluidic channels and medium wells. Medium height in reservoir wells is reset every day to maintain interstitial flow and fresh media is replaced every other day. To evaluate vessel formation, MPS are imaged every other day on a Lionheart FX (Agilent) automated fluorescent microscope using the standard 4x air objective.

Image Analysis (vessel formation and permeability assay/ perfusion test)

Mature vascular networks are challenged for perfusion and/ or permeability using 70kDa fluorophore-conjugated dextran (MilliporeSigma) dissolved in culture media at 50mg per mL. Vessel morphometric analysis was performed using MatLab 2022a and Rapid Editable Analysis of Vessel Elements Routine (REAVER) according to Corliss *et al.* [152].

Comsol Fluid Analysis

Images of tissue chambers were converted into a binary image and imported into AutoCAD in order to map the vessel morphometry. This file was then exported into

Comsol and fluid pressure inputs were applied to the media inlets and outlets based on media height in the media wells at the beginning of media flow. Output measurements of Comsol are fluid velocity and shear stress on the vascular wall.

Immunofluorescent microscopy:

MPS were fixed by perfusing 4% paraformaldehyde through the media channels of each device for 30 minutes. The bottom PDMS membrane was peeled from the device layer and each tissue chamber was manually excised and placed tissue-side down in a 24 well plate for staining. Tissues were washed 3 times for 5 minutes with DPBS on a gentle rocker before permeabilization for 30 minutes with 0.1% Triton-X 100 in DPBS. Tissues were blocked for 1 hour at room temperature in 0.1% Triton-X 100 with 5% FBS and 1% donkey serum before overnight incubation at 4°C with primary antibody in DPBS (TABLE 3.2). Tissue chambers were washed 3 times for 5 minutes with DPBS before 1 hour staining of secondary antibody. DAPI served as a nuclear stain and isotype controls were used as negative staining controls.

Bulk RNA Sequencing

Samples were sent to the UCI Genomics and Research Technology Hub (GRTH) for bulk RNA Illumina sequencing. Samples were prepared in house using the Zymo Quick RNA Mini-Prep kit and were evaluated on a nanodrop for purity and concentration before submission to the GRTH. Future experiments will use this data for deeper understanding of each iPSC-derived EC line.

Single-Cell RNA Sequencing:

Media was aspirated from each well and the bottom membrane was gently peeled off the device to expose the tissue chambers. Tissues were washed with 500μL of DPBS. To each, 100μL of TrypLE (Gibco) was added as a droplet on top of the chamber and incubated for 5 min. After digestion, tissue chambers were transferred into a 15mL conical tube with EGM2 and centrifuged at 300×g for 5 min at 4°C to pellet single cells and whole tissues. Media was carefully aspirated and 200U collagenase III in 1mL DPBS was added to the undigested tissues. After gentle pipetting, the solution was allowed to sit for 2 min at room temperature before pipetting gently again to dissociate the gel. Digestion mix was washed with 10mL of EGM2 and centrifuged at 300×g for 5 minutes at 4°C. Cells were resuspended into DPBS with 1% human serum albumin and passed through a moist 70μm filter by spinning at 200×g for 1 min. Cells were counted and volume was adjusted so that total cells were at a concentration of 1000 cells per μL.

Suspensions were loaded onto a Chromium Single Cell Instrument (10× Genomics) to generate single cell gel beads in emulsion (GEMs). GEMs were processed to generate cDNA libraries by using 10× Genomics v2 chemistry according to the Chromium Single Cell 3′ Reagent kit v2 user guide: CG00052 Rev B. Quantification of cDNA libraries was performed using Qubit dsDNA HS Assay kit (Life Technologies Q32851), high-sensitivity DNA chips (Agilent 5067-4626) and KAPA qPCR (Kapa Biosystems KK4824). Libraries were sequenced on an Illumina NovaSeq6000 to achieve an average of 50,000 reads per cell.

FASTQ files for each library were aligned to an indexed GRCh38 reference genome using Cell Ranger (10× genomics) Count 3.1.0 to generate count matrices. Count matrices were loaded into RStudio (1.2.5042 version, R version 4.0.4 [166,167]) and converted into a Seurat object using the Seurat R Package (version 4.0.0.9015 [168,169]). Cells containing more than 15% mitochondrial RNA or with less than 200 features were removed. Additionally, genes not detected in at least 3 cells were trimmed. Data were normalized, the 2000 top variable features were found, and scaled using the NormalizeData, Find VariableFeatures, and ScaleData functions, respectively. Data were further normalized using the SCTransform function and the difference between cells in the S phase and G2M phase was regressed to help distinguish non-cycling from cycling cells. Doublets were identified and removed using the DoubletFinder R package (version 2.0.3 [170]). A modified version of the chooseR R package was used to generate silhouette scores for selecting the resolution [171]. Clusters were labeled based on the expression of known markers (ECs: PECAM1, CDH5, VWF, KDR, CLDN5 [172]; fibroblasts: PDGFRα, PDGFRβ, COL1A1 [173]; stroma: PDGFRβ, TPM1, ACTA2 [174]; cycling cells: MKI67 and TOP2A. Heatmaps were generated by filtering expression for each clustering by log2 fold change. Pathway analysis was performed using clusterProfiler with the GO Biological Process 2021 database on the top 100 differentially expressed genes [175]. The significance of key pathways was directly compared for each dataset.

Individual libraries were integrated using the scMC Run- scMC R function and package (version 1.0.0) with default settings [176]. scMC removes the technical variation while preserving biological variation using variance analysis in an unsupervised manner.

For integration, the ‘RNA’ slot was used for each library. After integration, cell types were assigned to individual cells based on the analysis of the individual libraries. UMAP for all the datasets was generated with palette from the Polychrome R package (version 1.5.1) [177].

RESULTS

PWB vessel lesions in vitro match those seen in patients

Vessel lesions in patients show a dilated morphology when visualized using optical coherence tomography (OCT) imaging. Control tissue in middle (FIGURE 4.3 A) shows thin, evenly distributed capillaries in dermis, compared to hierarchical vessel overgrowth in rosacea dermis (left) or PWB dermis (left). PWB dermis shows unorganized and dilated vascular overgrowth as hallmark of disease presentation. The iEC are loaded into a MPS as outlined in FIGURE 4.3 B. iEC grow in the tissue chamber over a period of 1 week. Control iEC form thin microvessels (FIGURE 4.3 C) while GNAQ mutant iEC form areas of large dilation (FIGURE 4.3 D). These images were used for COMSOL fluid analysis (FIGURE 4.3 E) to highlight the low-flow characteristics of PWB vascular lesions. Additionally, some PWB VMO can show vascular tangles or areas of extreme dilation (FIGURE 4.3 F).

iEC form mature vasculature and recruit pericytes

Immunofluorescent staining of PWB VMO shows eGFP+ iEC surrounded by pericyte-like cells (FIGURE 4.4 A). These vessel lesions in the PBW VMO are larger in diameter than microvessels of wild-type iEC, sometimes by a substantial amount

(FIGURE 4.4 B). Confocal imaging of vessel lesions (FIGURE 4.4 C) and healthy vessels (FIGURE 4.4 D) in the PWB VMO show that both mutant and healthy vessels recruit pericyte-like cells to the abluminal surface of the vasculature, as seen in maximum z-projections of 3D images as well as 2D cross-section slices of vasculature. A decrease in mural cell coverage of vessel lesions was not observed.

Patient scSeq identifies BMP2 as a potential driver of lesion formation

Single cell RNA sequencing of patient scalp tissue was performed on birthmark and unaffected patient-matched control tissue on two PWB patients (referred to a Patient 3 and Patient 4; FIGURE 4.5 A). Sequencing was performed on 4mm biopsy punches of the dermis. Each biopsy's cell populations were combined into a unified UMAP (FIGURE 4.5 B) and cell types were identified based on expression of key cell identity genes (FIGURE 4.5 C). Cell types identified include EC, adipocytes, fibroblasts, lymphocytes and other immune cells, keratinocytes, melanocytes, and smooth muscle cells. The EC population was subclustered (FIGURE 4.5 D) to identify EC subpopulations that were uniquely present in both PWB biopsy samples but not in the matched control tissue. This analysis identified the unique subpopulation 6 that, we believe, has the GNAQ mutation (FIGURE 4.5 E). Pathway analysis of these subpopulations identifies that BMP2 is one of the most highly differentially expressed genes in subpopulation 6 (FIGURE 4.5 F). Given its role in the TGFβ superfamily, we identify it as a candidate for driving lesion formation in PWB and worthy of further exploration in future projects.

The PWB VMO has been sequenced using scRNA Seq

To validate the transcriptomic profile of the PWB VMO with that of the patient samples, the PWB VMO was tested via scRNA seq. Control and mutant vessel networks were analyzed for sequencing at two different timepoints. An early timepoint of Day3 (FIGURE 4.6 A-B) was selected to highlight gene profiles of nascent vessels still forming lesions; additionally, the timepoint at Day6 (FIGURE 4.6 C-D) in VMO development was selected as vessels were already formed and in the process of maturing. In this way, we hope to identify through ongoing studies how BMP2 might be playing a role in lesion formation versus genes that may be contributing to lesion stabilization or progression.

DISCUSSION

Building off the procedures in the previous chapters, we have combined our knowledge of MPS tissue chips and port wine birthmark genetic drivers to successfully make a model of PWB that captures the hallmarks of the disease in patients. These PWB tissues capture a dilated vessel phenotype that characterizes lesions in the dermis. In contrast, many modern PWB models fail to recapitulate this morphology [178,179]. Most show poor vascularization of disconnected microvessels, and in vivo models typically do not show morphology in the dermis but instead present in tissues such as the gut (which are unaffected in human patients). As such, we believe that our model system provides a more physiologically-relevant microenvironment to test therapeutics.

Many researchers have been working on developing therapeutics for PWB, mostly by treating the immediate downstream predicted effectors of GNAQ like MEK, ERK, or Rho/Rac [178,180,181]. However, intervention of these pathways individually has shown little efficacy in patients. It is possible that GNAQ is promiscuous enough that overactivation of both of these pathways (possibly combined with others) leads to lesion formation. We therefore are hopeful that BMP2 inhibition will show more promise as it is downstream of both the MAPK and Rho/Rac pathways.

It is possible that mutant GNAQ driving BMP2 activation causes lesion formation through perturbation of the TGFβ-VEGF-Notch relationships, as this axis plays a key role in vascular formation and maintenance [182–188]. Future experiments will evaluate if BMP2 inhibition or antagonism will prevent mutant iEC from forming PWB lesions.

Furthermore, it is possible that BMP2 may play a key role in uncovering disease biology in SWS vascular lesions as BMP2-directed calcification may be involved in neuronal tissue pathology [178]. As of yet, we do not understand why PWB vascular lesions in the brain have slightly different pathology relating to calcium deposition, nor do we understand what vascular defects might relate to neurologic impairment and epilepsy in patients with SWS. BMP2 activation, as it relates to calcium signaling, could be responsible for these impacts.

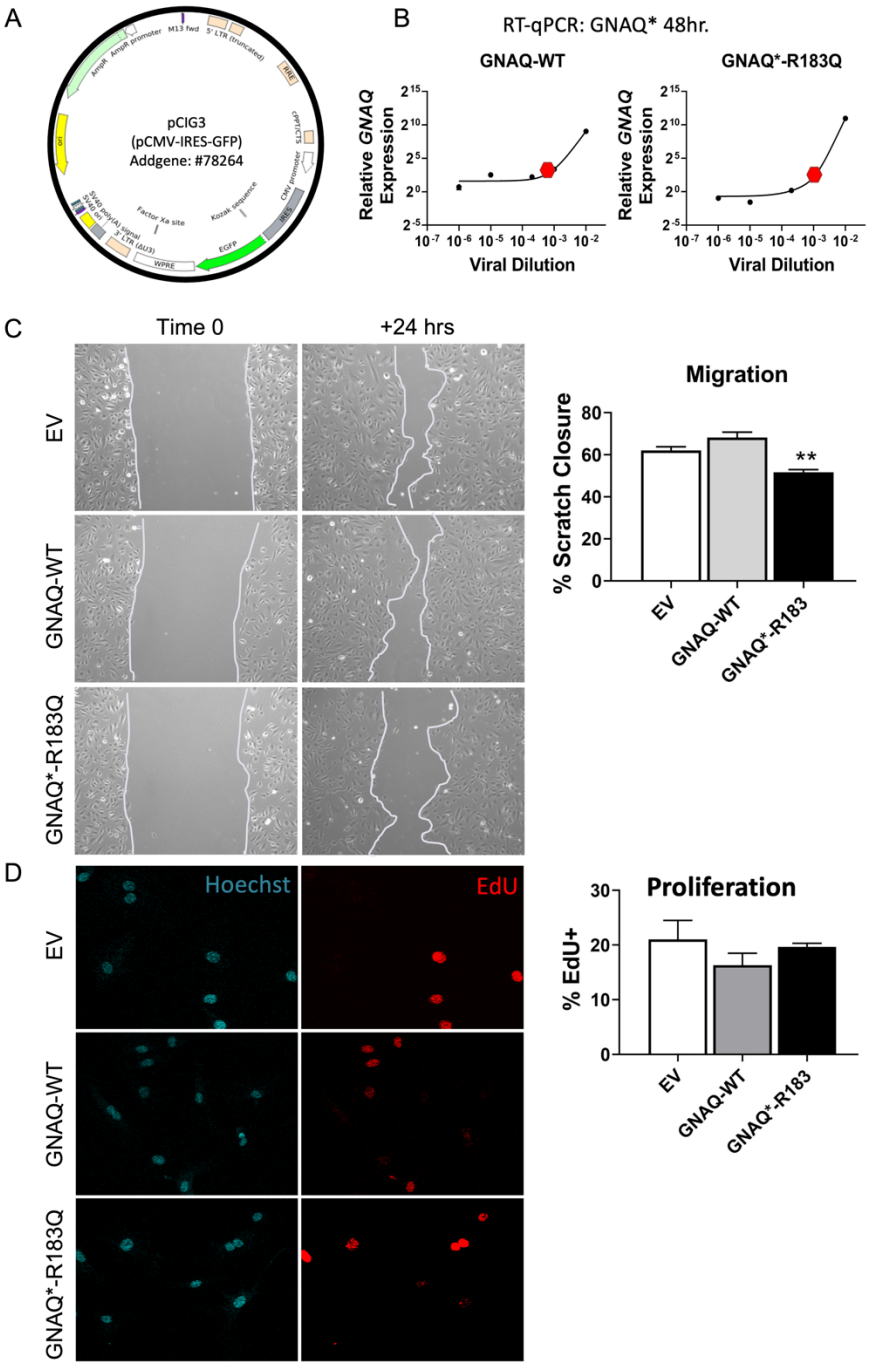

FIGURE 4.1: GNAQ* lentivirus impairs ECFC migration but not proliferation.

(A) Plasmid map of pCI3G backbone. Cloning site between CMV promotor and IRES sites. (B) qPCR quantification of total GNAQ expression of ECFC transduced with control and GNAQ*-R183Q lentivirus. (C) Scratch assay of GNAQ*-ECFC identifies

reduction in migration capacity 24 hours post-scratch. n=15 for each condition. (D) Edu incorporation assay performed 48 hours post-transduction does not revel effect of GNAQ*-R183Q on proliferation rate of ECFC. n= 36 for each condition.

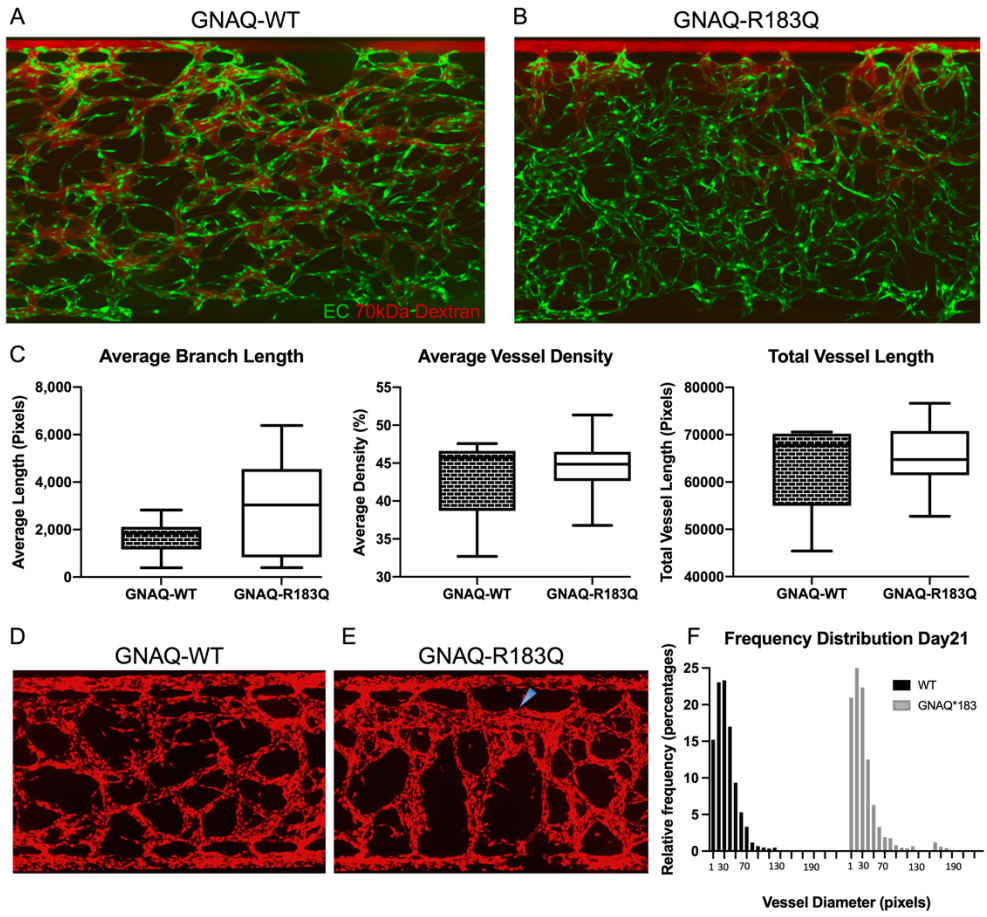

FIGURE 4.2: GNAQ*-ECFC form hyperdense vascular beds with small areas of dilation.

(A) ECFC (green) transduced with GNAQ-WT control and (B) GNAQ*-R183Q lentivirus form vascularized in vitro networks that are perfusable by Day10. (C) Morphogenic analysis of vascularized networks at Day10 identify increases in vessel branch length and density. (D) vascular networks continue developing and remodeling to day21. (F) quantification of vessel diameter at Day21 identifies small portions of GNAQ*-ECFC vasculature (red) that is dilated.

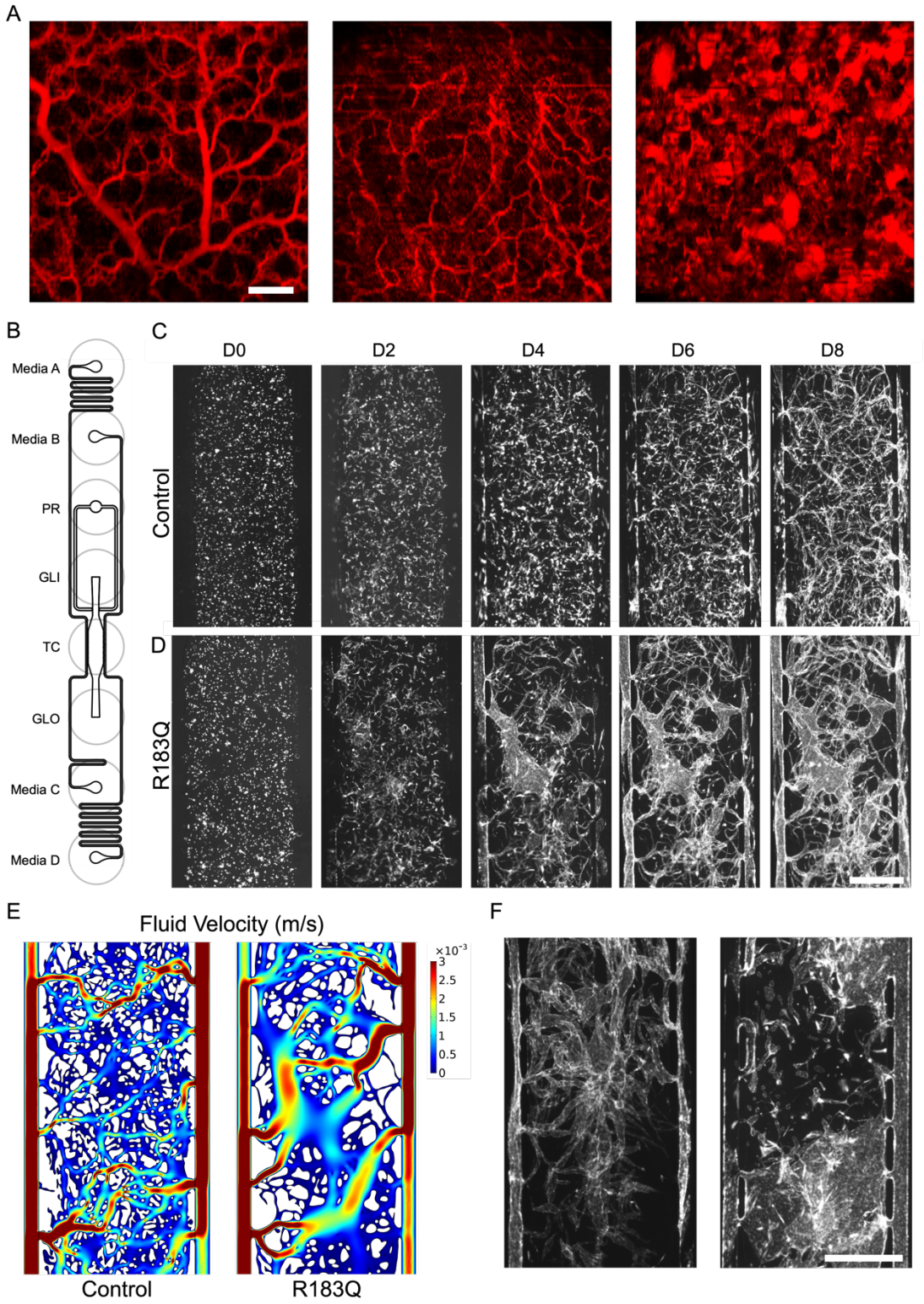

FIGURE 4.3: In vitro model of PWB matches morphology of PWB lesions in patient skin.

A) OCT images of WT, rosacea, PWB, respectively. B) CAD schematic of MPS. (PR pressure release valve; GLI gel loading inlet; TC tissue chamber; GLO gel loading outlet). C-D) fluorescent WT and mutant vessels formation from start to Day8. E) comsol of flow from networks in C-D. F) representative images of more mutant networks. All scale bars 1mm

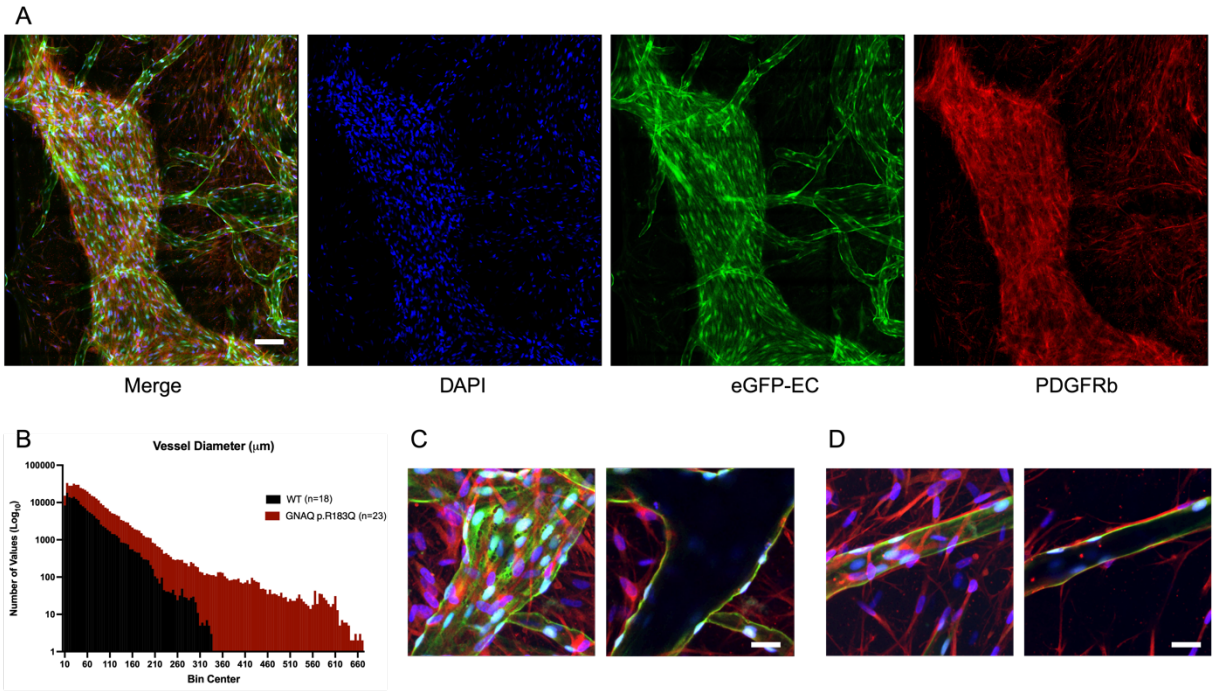

FIGURE 4.4: Morphology of mutant vessels in VMO.

(A) IF staining of PWB vessel lesion in VMO identifies PDGFRβ+ pericytes surrounding eGFP+ ECf. Scale bar 100 µm. (B) Vessel diameter measurements capture dilated diameter of mutant iEC vessels. (C) Mutant and (D) control vessels are surrounded by PDGFRβ+ pericytes at the eGFP+ vessel wall. Z-stack projections and 2D slices, respectively. Scale bars 25 µm.

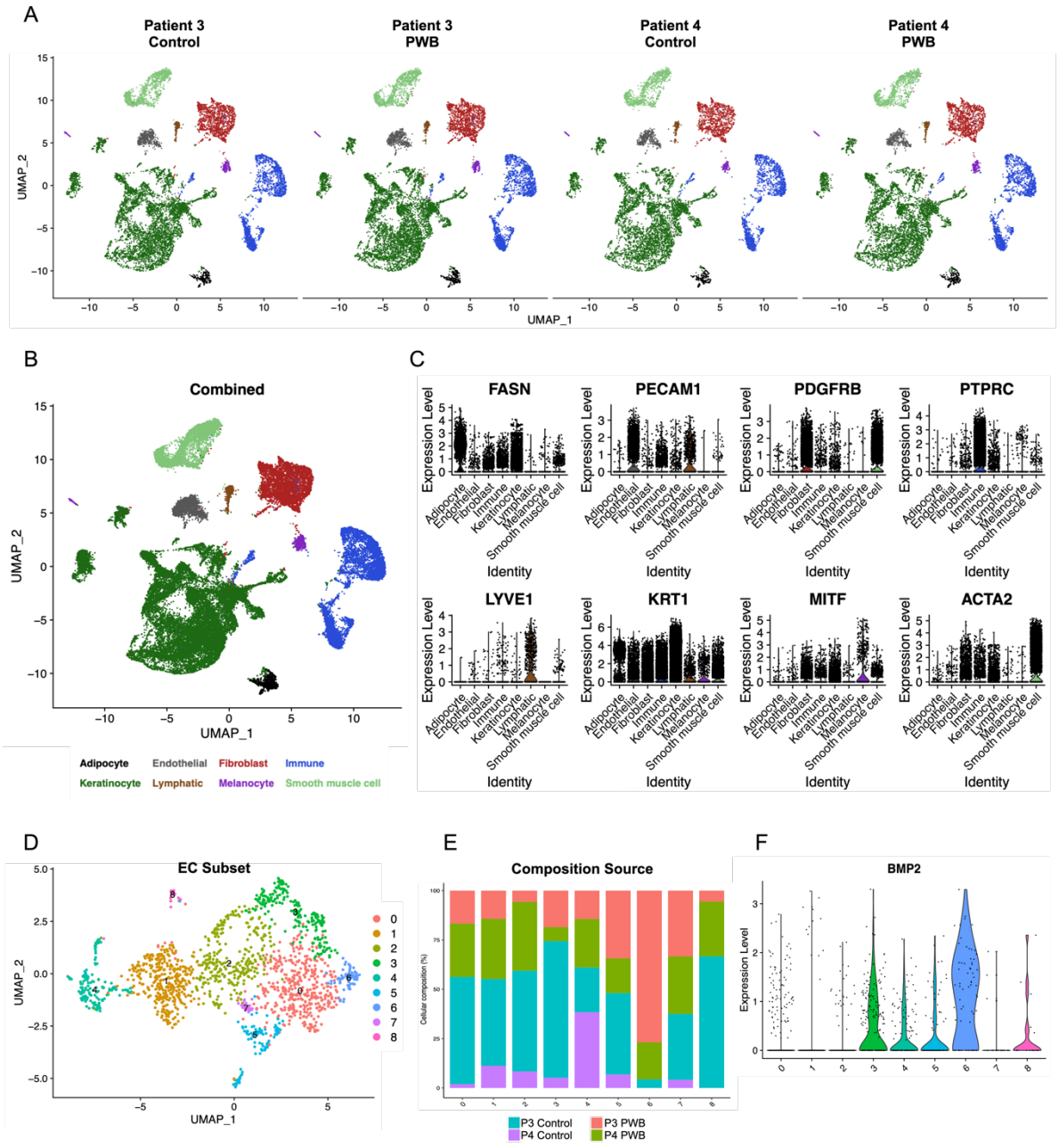

FIGURE 4.5: Patient scSeq reveals BMP2 activated EC subset in PWB vessel lesions. (A) UMAPs for individual datasets of patient PWB and matched tissue controls are combined into unified UMAP in (B). (C) Cell types are identified by key marker expression. (D-E) Endothelial cells from UMAP in (B) are subset into subpopulations to

identify a subpopulation #6 of EC that is unique to PWB tissue samples. (F) This PWB subpopulation #6 uniquely expresses very high levels of BMP2.

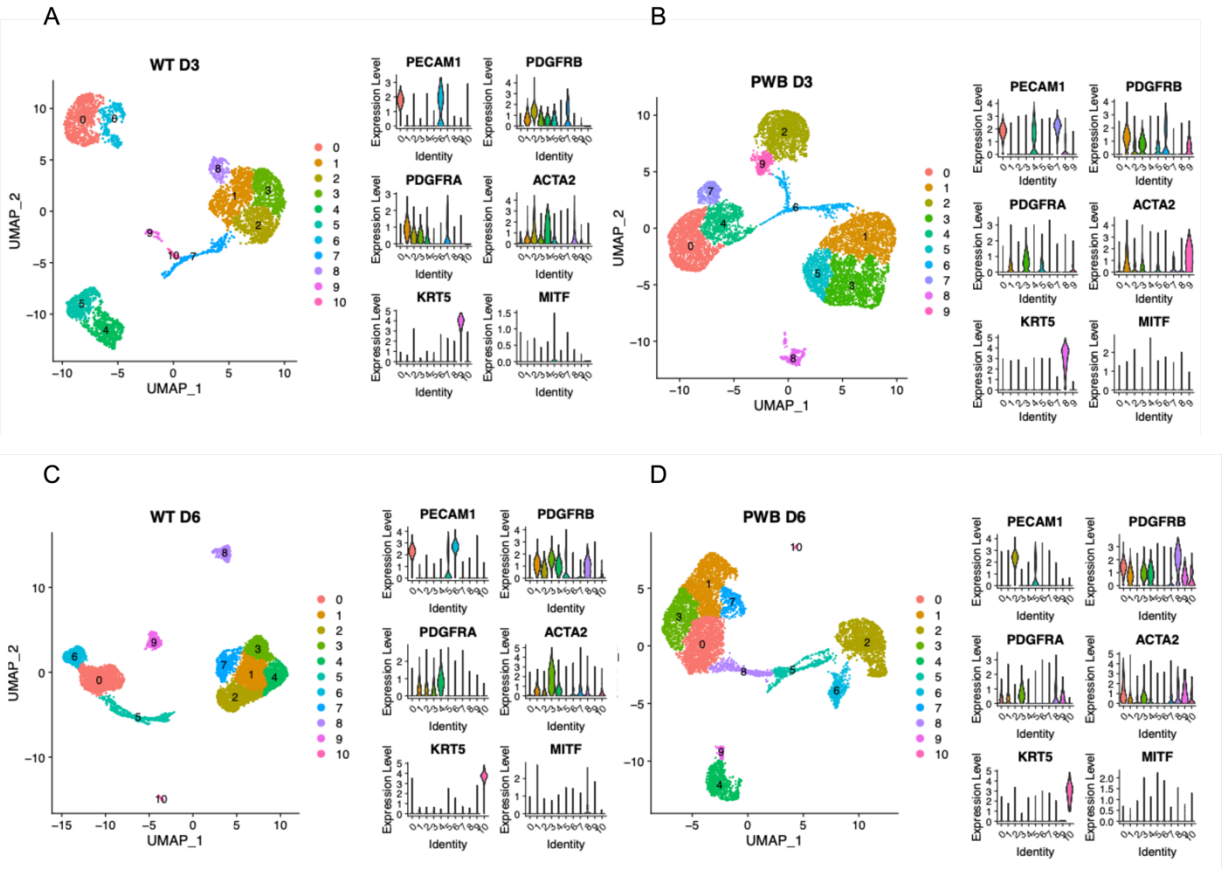

FIGURE 4.6: PWB MPS scSeq identifies multiple cell types.

(A) Control VMO and (B) PWB VMO tissue chambers isolated at Day3 of vessel formation. (C) Control VMO and (D) PWB VMO tissue chambers isolated at Day6 of vessel formation.

REFERENCES

1. Mestas, J. & Hughes, C. C. W. Of mice and not men: differences between mouse and human immunology. *J. Immunol. Baltim. Md 1950* **172**, 2731–2738 (2004).
2. Martignoni, M., Groothuis, G. M. M. & de Kanter, R. Species differences between mouse, rat, dog, monkey and human CYP-mediated drug metabolism, inhibition and induction. *Expert Opin. Drug Metab. Toxicol.* **2**, 875–894 (2006).
3. Brehm, M. A., Shultz, L. D., Luban, J. & Greiner, D. L. Overcoming Current Limitations in Humanized Mouse Research. *J. Infect. Dis.* **208**, S125–S130 (2013).
4. Hsu, Y.-H. *et al.* Full range physiological mass transport control in 3D tissue cultures. *Lab. Chip* **13**, 81–89 (2013).
5. Moya, M. L., Hsu, Y.-H., Lee, A. P., Hughes, C. C. W. & George, S. C. In vitro perfused human capillary networks. *Tissue Eng. Part C Methods* **19**, 730–737 (2013).
6. Phan, D. T. T. *et al.* A vascularized and perfused organ-on-a-chip platform for large-scale drug screening applications. *Lab. Chip* **17**, 511–520 (2017).
7. Yue, T. *et al.* A modular microfluidic system based on a multilayered configuration to generate large-scale perfusable microvascular networks. *Microsyst. Nanoeng.* **7**, 4 (2021).
8. Wang, X. *et al.* Engineering anastomosis between living capillary networks and endothelial cell-lined microfluidic channels. *Lab. Chip* **16**, 282–290 (2016).
9. Wang, X. *et al.* An on-chip microfluidic pressure regulator that facilitates reproducible loading of cells and hydrogels into microphysiological system platforms. *Lab. Chip* **16**, 868–876 (2016).

10. Wang, X., Phan, D. T. T., George, S. C., Hughes, C. C. W. & Lee, A. P. 3D Anastomosed Microvascular Network Model with Living Capillary Networks and Endothelial Cell-Lined Microfluidic Channels. *Methods Mol. Biol. Clifton NJ* **1612**, 325–344 (2017).

11. Newman, A. C., Nakatsu, M. N., Chou, W., Gershon, P. D. & Hughes, C. C. W. The requirement for fibroblasts in angiogenesis: fibroblast-derived matrix proteins are essential for endothelial cell lumen formation. *Mol. Biol. Cell* **22**, 3791–3800 (2011).

12. Newman, A. C. *et al.* Analysis of stromal cell secretomes reveals a critical role for stromal cell-derived hepatocyte growth factor and fibronectin in angiogenesis. *Arterioscler. Thromb. Vasc. Biol.* **33**, 513–522 (2013).

13. Phan, D. T. *et al.* Blood-brain barrier-on-a-chip: Microphysiological systems that capture the complexity of the blood-central nervous system interface. *Exp. Biol. Med. Maywood NJ* **242**, 1669–1678 (2017).

14. Bender, R. H. F. *et al.* A vascularized 3D model of the human pancreatic islet for ex vivo study of immune cell-islet interaction. *Biofabrication* **16**, 025001 (2024).

15. Sobrino, A. *et al.* 3D microtumors in vitro supported by perfused vascular networks. *Sci. Rep.* **6**, 31589 (2016).

16. Liu, Y. *et al.* Human in vitro vascularized micro-organ and micro-tumor models are reproducible organ-on-a-chip platforms for studies of anticancer drugs. *Toxicology* **445**, 152601 (2020).

17. Hachey, S. J. & Hughes, C. C. W. Applications of tumor chip technology. *Lab. Chip* **18**, 2893–2912 (2018).

18. Hachey, S. J. *et al.* An in vitro vascularized micro-tumor model of human colorectal cancer recapitulates in vivo responses to standard-of-care therapy. *Lab. Chip* **21**, 1333–1351 (2021).

19. Hachey, S. J., Gaebler, D. & Hughes, C. C. W. Establishing a Physiologic Human Vascularized Micro-Tumor Model for Cancer Research. *J. Vis. Exp. JoVE* (2023) doi:10.3791/65865.

20. Hachey, S. J. *et al.* A human vascularized microtumor model of patient-derived colorectal cancer recapitulates clinical disease. *Transl. Res. J. Lab. Clin. Med.* **255**, 97–108 (2023).

21. Hachey, S. J. *et al.* Targeting tumor-stromal interactions in triple-negative breast cancer using a human vascularized micro-tumor model. *Breast Cancer Res. BCR* **26**, 5 (2024).

22. Ewald, M. L., Chen, Y.-H., Lee, A. P. & Hughes, C. C. W. The vascular niche in next generation microphysiological systems. *Lab. Chip* **21**, 3244–3262 (2021).

23. Aghajanian, A., Wittchen, E. S., Allingham, M. J., Garrett, T. A. & Burridge, K. Endothelial cell junctions and the regulation of vascular permeability and leukocyte transmigration. *J. Thromb. Haemost. JTH* **6**, 1453–1460 (2008).

24. Patan, S. Vasculogenesis and angiogenesis. *Cancer Treat. Res.* **117**, 3–32 (2004).

25. Potente, M. & Mäkinen, T. Vascular heterogeneity and specialization in development and disease. *Nat. Rev. Mol. Cell Biol.* **18**, 477–494 (2017).

26. Tahergorabi, Z. & Khazaei, M. A Review on Angiogenesis and Its Assays. *Iran. J. Basic Med. Sci.* **15**, 1110–1126 (2012).

27. Hatch, C. J. *et al.* SARS-CoV-2 infection of endothelial cells, dependent on flow-induced ACE2 expression, drives hypercytokinemia in a vascularized microphysiological system. *Front. Cardiovasc. Med.* **11**, (2024).

28. Yin, R. *et al.* Activation of PKCα and PI3K Kinases in Hypertrophic and Nodular Port Wine Stain Lesions. *Am. J. Dermatopathol.* **39**, 747–752 (2017).

29. Kanada, K. N., Merin, M. R., Munden, A. & Friedlander, S. F. A prospective study of cutaneous findings in newborns in the United States: correlation with race, ethnicity, and gestational status using updated classification and nomenclature. *J. Pediatr.* **161**, 240–245 (2012).

30. Higueros, E., Roe, E., Granell, E. & Baselga, E. Sturge-Weber Syndrome: A Review. *Actas Dermosifiliogr.* **108**, 407–417 (2017).

31. Martins, L. *et al.* Computational analysis for GNAQ mutations: New insights on the molecular etiology of Sturge-Weber syndrome. *J. Mol. Graph. Model.* **76**, 429–440 (2017).

32. Sturge Weber Foundation. *The Sturge Weber Foundation* https://sturge-weber.org/.

33. Couto, J. A. *et al.* Endothelial Cells from Capillary Malformations Are Enriched for Somatic GNAQ Mutations. *Plast. Reconstr. Surg.* **137**, 77e–82e (2016).

34. Bichsel, C. & Bischoff, J. A somatic missense mutation in GNAQ causes capillary malformation. *Curr. Opin. Hematol.* **26**, 179–184 (2019).

35. Schneider, B. *et al.* Frequent and Yet Unreported GNAQ and GNA11 Mutations are Found in Uveal Melanomas. *Pathol. Oncol. Res. POR* **25**, 1319–1325 (2019).

36. Jain, F., Longakit, A., Huang, J. L.-Y. & Van Raamsdonk, C. D. Endothelin signaling promotes melanoma tumorigenesis driven by constitutively active GNAQ. *Pigment Cell Melanoma Res.* **33**, 834–849 (2020).

37. Lee, K.-T. *et al.* Phenotypic association of presence of a somatic GNAQ mutation with port-wine stain distribution in capillary malformation. *Head Neck* **41**, 4143–4150 (2019).

38. Lee, J. W., Chung, H. Y., Cerrati, E. W., O, T. M. & Waner, M. The Natural History of Soft Tissue Hypertrophy, Bony Hypertrophy, and Nodule Formation in Patients With Untreated Head and Neck Capillary Malformations. *Dermatol. Surg. Off. Publ. Am. Soc. Dermatol. Surg. Al* **41**, 1241–1245 (2015).

39. Tierney, E. P. & Hanke, C. W. Treatment of nodules associated with port wine stains with CO2 laser: case series and review of the literature. *J. Drugs Dermatol. JDD* **8**, 157–161 (2009).

40. Cong, T., Liu, L., Zhang, H., Wang, L. & Jiang, X. Port-wine stains associated with large vestibular aqueduct syndrome caused by mutations in GNAQ and SLC26A4 genes: A case report. *J. Dermatol.* **47**, 78–81 (2020).

41. Huang, L. *et al.* Somatic GNAQ Mutation is Enriched in Brain Endothelial Cells in Sturge-Weber Syndrome. *Pediatr. Neurol.* **67**, 59–63 (2017).

42. Nakashima, M. *et al.* The somatic GNAQ mutation c.548G>A (p.R183Q) is consistently found in Sturge-Weber syndrome. *J. Hum. Genet.* **59**, 691–693 (2014).

43. Shirley, M. D. *et al.* Sturge-Weber syndrome and port-wine stains caused by somatic mutation in GNAQ. *N. Engl. J. Med.* **368**, 1971–1979 (2013).

44. Daniels, A. B. *et al.* High throughput mass spectrometry-based mutation profiling of primary uveal melanoma. *Invest. Ophthalmol. Vis. Sci.* **53**, 6991–6996 (2012).

45. Jordan, M. *et al.* Reverse Phenotyping in Patients with Skin Capillary Malformations and Mosaic GNAQ or GNA11 Mutations Defines a Clinical Spectrum with Genotype-Phenotype Correlation. *J. Invest. Dermatol.* **140**, 1106-1110.e2 (2020).

46. Perelman School of Medicine, University of Pennsylvania, Genetic Diagnostic Laboratory. U Penn Dept. of Genetics. *Somatic Overgrowth and Vascular Malformation Genetic Testing* https://genetics.med.upenn.edu/.

47. Waelchli, R. *et al.* New vascular classification of port-wine stains: improving prediction of Sturge-Weber risk. *Br. J. Dermatol.* **171**, 861–867 (2014).

48. Sabeti, S. *et al.* Consensus Statement for the Management and Treatment of Port-Wine Birthmarks in Sturge-Weber Syndrome. *JAMA Dermatol.* **157**, 98–104 (2021).

49. Bichsel, C. A. *et al.* Association of Somatic GNAQ Mutation With Capillary Malformations in a Case of Choroidal Hemangioma. *JAMA Ophthalmol.* **137**, 91–95 (2019).

50. Izikson, L., Nelson, J. S. & Anderson, R. R. Treatment of hypertrophic and resistant port wine stains with a 755 nm laser: a case series of 20 patients. *Lasers Surg. Med.* **41**, 427–432 (2009).

51. Bernstein, E. F. The pulsed-dye laser for treatment of cutaneous conditions. *G. Ital. Dermatol. E Venereol. Organo Uff. Soc. Ital. Dermatol. E Sifilogr.* **144**, 557–572 (2009).

52. Bae, Y.-S. C., Alabdulrazzaq, H., Brauer, J. A. & Geronemus, R. G. Treatment of recalcitrant port-wine stains (PWS) using a combined pulsed dye laser (PDL) and radiofrequency (RF) energy device. *J. Am. Acad. Dermatol.* **76**, 321–326 (2017).

53. Yu, W. *et al.* Why do port-wine stains (PWS) on the lateral face respond better to pulsed dye laser (PDL) than those located on the central face? *J. Am. Acad. Dermatol.* **74**, 527–535 (2016).

54. Wang, B., Mei, X., Wang, Y., Hu, X. & Li, F. Adjuncts to pulsed dye laser for treatment of port wine stains: a literature review. *J. Cosmet. Laser Ther. Off. Publ. Eur. Soc. Laser Dermatol.* 1–9 (2022) doi:10.1080/14764172.2022.2052901.

55. Lipner, S. R. Topical Adjuncts to Pulsed Dye Laser for Treatment of Port Wine Stains: Review of the Literature. *Dermatol. Surg. Off. Publ. Am. Soc. Dermatol. Surg. Al* **44**, 796–802 (2018).

56. Sidbury, R. *et al.* Topically applied imiquimod inhibits vascular tumor growth in vivo. *J. Invest. Dermatol.* **121**, 1205–1209 (2003).

57. Gao, L. *et al.* Topical axitinib suppresses angiogenesis pathways induced by pulsed dye laser. *Br. J. Dermatol.* **172**, 669–676 (2015).

58. Taquin, H., Lacour, J.-P., Le Duff, F., Chiaverini, C. & Passeron, T. Treatment of resistant port-wine stains with bosentan and pulsed dye laser: a pilot prospective study. *J. Eur. Acad. Dermatol. Venereol. JEADV* **30**, 1432–1434 (2016).

59. Rikihisa, N. *et al.* Intravenous injection of artificial red cells and subsequent dye laser irradiation causes deep vessel impairment in an animal model of port-wine stain. *Lasers Med. Sci.* **33**, 1287–1293 (2018).

60. Rikihisa, N., Watanabe, S., Satoh, K., Saito, Y. & Sakai, H. Photosensitizer Effects of Artificial Red Cells on Dye Laser Irradiation in an Animal Model Assuming Port-Wine Stain Treatment. *Plast. Reconstr. Surg.* **139**, 707e–716e (2017).

61. Kelly, A., Pai, A., Lertsakdadet, B., Choi, B. & Kelly, K. M. Microvascular Effects of Pulsed Dye Laser in Combination With Oxymetazoline. *Lasers Surg. Med.* **52**, 17–22 (2020).

62. Sebold, A. J. *et al.* Sirolimus Treatment in Sturge-Weber Syndrome. *Pediatr. Neurol.* **115**, 29–40 (2021).

63. Miller, R. S., Ball, K. L., Comi, A. M. & Germain-Lee, E. L. Growth hormone deficiency in Sturge-Weber syndrome. *Arch. Dis. Child.* **91**, 340–341 (2006).

64. Bachur, C. D., Comi, A. M. & Germain-Lee, E. L. Partial Hypopituitarism in Patients With Sturge-Weber Syndrome. *Pediatr. Neurol.* **53**, e5-6 (2015).

65. Neves, S. R., Ram, P. T. & Iyengar, R. G protein pathways. *Science* **296**, 1636–1639 (2002).

66. Urtatiz, O. & Van Raamsdonk, C. D. Gnaq and Gna11 in the Endothelin Signaling Pathway and Melanoma. *Front. Genet.* **7**, 59 (2016).

67. Syrovatkina, V., Alegre, K. O., Dey, R. & Huang, X.-Y. Regulation, Signaling, and Physiological Functions of G-Proteins. *J. Mol. Biol.* **428**, 3850–3868 (2016).

68. Simon, M. I., Strathmann, M. P. & Gautam, N. Diversity of G proteins in signal transduction. *Science* **252**, 802–808 (1991).

69. Dong, Q. *et al.* Molecular cloning of human G alpha q cDNA and chromosomal localization of the G alpha q gene (GNAQ) and a processed pseudogene. *Genomics* **30**, 470–475 (1995).

70. Oldham, W. M. & Hamm, H. E. Structural basis of function in heterotrimeric G proteins. *Q. Rev. Biophys.* **39**, 117–166 (2006).

71. Wolf, Y. I., Brenner, S. E., Bash, P. A. & Koonin, E. V. Distribution of protein folds in the three superkingdoms of life. *Genome Res.* **9**, 17–26 (1999).

72. Sprang, S. R. G protein mechanisms: insights from structural analysis. *Annu. Rev. Biochem.* **66**, 639–678 (1997).

73. Bosch, D. E. *et al.* A P-loop mutation in Gα subunits prevents transition to the active state: implications for G-protein signaling in fungal pathogenesis. *PLoS Pathog.* **8**, e1002553 (2012).

74. Strange, P. G. Signaling mechanisms of GPCR ligands. *Curr. Opin. Drug Discov. Devel.* **11**, 196–202 (2008).

75. Venkatakrishnan, A. J. *et al.* Molecular signatures of G-protein-coupled receptors. *Nature* **494**, 185–194 (2013).

76. Hepler, J. R. *et al.* Functional importance of the amino terminus of Gq alpha. *J. Biol. Chem.* **271**, 496–504 (1996).

77. Tall, G. G., Krumins, A. M. & Gilman, A. G. Mammalian Ric-8A (synembryn) is a heterotrimeric Galpha protein guanine nucleotide exchange factor. *J. Biol. Chem.* **278**, 8356–8362 (2003).

78. Tall, G. G. & Gilman, A. G. Purification and functional analysis of Ric-8A: a guanine nucleotide exchange factor for G-protein alpha subunits. *Methods Enzymol.* **390**, 377–388 (2004).

79. Gabay, M. *et al.* Ric-8 proteins are molecular chaperones that direct nascent G protein α subunit membrane association. *Sci. Signal.* **4**, ra79 (2011).

80. Kimple, R. J., Kimple, M. E., Betts, L., Sondek, J. & Siderovski, D. P. Structural determinants for GoLoco-induced inhibition of nucleotide release by Galpha subunits. *Nature* **416**, 878–881 (2002).

81. Garcia-Marcos, M., Ghosh, P. & Farquhar, M. G. GIV is a nonreceptor GEF for G alpha i with a unique motif that regulates Akt signaling. *Proc. Natl. Acad. Sci. U. S. A.* **106**, 3178–3183 (2009).

82. Ghosh, P., Garcia-Marcos, M. & Farquhar, M. G. GIV/Girdin is a rheostat that fine-tunes growth factor signals during tumor progression. *Cell Adhes. Migr.* **5**, 237–248 (2011).

83. Baltoumas, F. A., Theodoropoulou, M. C. & Hamodrakas, S. J. Interactions of the α-subunits of heterotrimeric G-proteins with GPCRs, effectors and RGS proteins: a critical review and analysis of interacting surfaces, conformational shifts, structural diversity and electrostatic potentials. *J. Struct. Biol.* **182**, 209–218 (2013).

84. Soundararajan, M. *et al.* Structural diversity in the RGS domain and its interaction with heterotrimeric G protein alpha-subunits. *Proc. Natl. Acad. Sci. U. S. A.* **105**, 6457–6462 (2008).

85. Sjögren, B. Regulator of G protein signaling proteins as drug targets: current state and future possibilities. *Adv. Pharmacol. San Diego Calif* **62**, 315–347 (2011).

86. Rhee, S. G. & Bae, Y. S. Regulation of phosphoinositide-specific phospholipase C isozymes. *J. Biol. Chem.* **272**, 15045–15048 (1997).

87. Lutz, S. *et al.* Structure of Galphaq-p63RhoGEF-RhoA complex reveals a pathway for the activation of RhoA by GPCRs. *Science* **318**, 1923–1927 (2007).

88. Musi, E. *et al.* Tris DBA palladium is an orally available inhibitor of GNAQ mutant uveal melanoma in vivo. *Oncotarget* **10**, 4424–4436 (2019).

89. Li, Z. *et al.* Recurrent GNAQ mutation encoding T96S in natural killer/T cell lymphoma. *Nat. Commun.* **10**, 4209 (2019).

90. Gaeta, R. *et al.* Diffuse bone and soft tissue angiomatosis with GNAQ mutation. *Pathol. Int.* **70**, 452–457 (2020).

91. He, R. *et al.* Klippel-Trenaunay and Sturge-Weber Overlap Syndrome with KRAS and GNAQ mutations. *Ann. Clin. Transl. Neurol.* **7**, 1258–1264 (2020).

92. Garcia, R. J. *et al.* Endothelin 3 induces skin pigmentation in a keratin-driven inducible mouse model. *J. Invest. Dermatol.* **128**, 131–142 (2008).

93. Van Raamsdonk, C. D. *et al.* Frequent somatic mutations of GNAQ in uveal melanoma and blue naevi. *Nature* **457**, 599–602 (2009).

94. Choi, J.-Y., Lee, Y. S., Shim, D. M. & Seo, S. W. Effect of GNAQ alteration on RANKL-induced osteoclastogenesis in human non-small-cell lung cancer. *Bone Jt. Res.* **9**, 29–35 (2020).

95. Francis, J. H. *et al.* Investigation of Somatic GNAQ, GNA11, BAP1 and SF3B1 Mutations in Ophthalmic Melanocytomas. *Ocul. Oncol. Pathol.* **2**, 171–177 (2016).

96. Fortin Ensign, S. *et al.* Genomic analysis reveals low tumor mutation burden which may be associated with GNAQ/11 alteration in a series of primary leptomeningeal melanomas. *Pigment Cell Melanoma Res.* **33**, 458–465 (2020).

97. Schrader, K. A. *et al.* Germline Variants in Targeted Tumor Sequencing Using Matched Normal DNA. *JAMA Oncol.* **2**, 104–111 (2016).

98. Wettschureck, N. *et al.* Loss of Gq/11 family G proteins in the nervous system causes pituitary somatotroph hypoplasia and dwarfism in mice. *Mol. Cell. Biol.* **25**, 1942–1948 (2005).

99. Frederick, A. L., Saborido, T. P. & Stanwood, G. D. Neurobehavioral phenotyping of G(αq) knockout mice reveals impairments in motor functions and spatial working memory without changes in anxiety or behavioral despair. *Front. Behav. Neurosci.* **6**, 29 (2012).

100. Chen, Y. *et al.* Endogenous Gαq-Coupled Neuromodulator Receptors Activate Protein Kinase A. *Neuron* **96**, 1070-1083.e5 (2017).

101. Arey, R. N., Stein, G. M., Kaletsky, R., Kauffman, A. & Murphy, C. T. Activation of Gαq Signaling Enhances Memory Consolidation and Slows Cognitive Decline. *Neuron* **98**, 562-574.e5 (2018).

102. Zhai, M. *et al.* The effect of GNAQ methylation on GnRH secretion in sheep hypothalamic neurons. *J. Cell. Biochem.* **120**, 19396–19405 (2019).

103. Sun, X. *et al.* Gnaq Protects PC12 Cells from Oxidative Damage by Activation of Nrf2 and Inhibition of NF-kB. *Neuromolecular Med.* **22**, 401–410 (2020).

104. Abecassis, I. J., Xu, D. S., Batjer, H. H. & Bendok, B. R. Natural history of brain arteriovenous malformations: a systematic review. *Neurosurg. Focus* **37**, E7 (2014).

105. Stefani, M. A. *et al.* Large and deep brain arteriovenous malformations are associated with risk of future hemorrhage. *Stroke* **33**, 1220–1224 (2002).

106. Halim, A. X. *et al.* Longitudinal risk of intracranial hemorrhage in patients with arteriovenous malformation of the brain within a defined population. *Stroke* **35**, 1697–1702 (2004).

107. Cordonnier, C., Klijn, C. J. M., van Beijnum, J. & Al-Shahi Salman, R. Radiological investigation of spontaneous intracerebral hemorrhage: systematic review and trinational survey. *Stroke* **41**, 685–690 (2010).

108. van Beijnum, J. *et al.* Outcome after spontaneous and arteriovenous malformation-related intracerebral haemorrhage: population-based studies. *Brain J. Neurol.* **132**, 537–543 (2009).

109. Barbosa Do Prado, L., Han, C., Oh, S. P. & Su, H. Recent Advances in Basic Research for Brain Arteriovenous Malformation. *Int. J. Mol. Sci.* **20**, E5324 (2019).

110. Nikolaev, S. I. *et al.* Somatic Activating KRAS Mutations in Arteriovenous Malformations of the Brain. *N. Engl. J. Med.* **378**, 250–261 (2018).

111. Al-Olabi, L. *et al.* Mosaic RAS/MAPK variants cause sporadic vascular malformations which respond to targeted therapy. *J. Clin. Invest.* **128**, 1496–1508 (2018).

112. Chen, W. *et al.* Reduced mural cell coverage and impaired vessel integrity after angiogenic stimulation in the Alk1-deficient brain. *Arterioscler. Thromb. Vasc. Biol.* **33**, 305–310 (2013).

113. Choi, J. H. & Mohr, J. P. Brain arteriovenous malformations in adults. *Lancet Neurol.* **4**, 299–308 (2005).

114. Cheng, P. *et al.* Effect of elevation of vascular endothelial growth factor level on exacerbation of hemorrhage in mouse brain arteriovenous malformation. *J. Neurosurg.* **132**, 1566–1573 (2019).

115. Chen, Y. *et al.* Evidence of inflammatory cell involvement in brain arteriovenous malformations. *Neurosurgery* **62**, 1340–1349; discussion 1349-1350 (2008).

116. Ola, R. *et al.* PI3 kinase inhibition improves vascular malformations in mouse models of hereditary haemorrhagic telangiectasia. *Nat. Commun.* **7**, 13650 (2016).

117. Kim, T. *et al.* Epidemiology of ruptured brain arteriovenous malformation: a National Cohort Study in Korea. *J. Neurosurg.* 1–6 (2018) doi:10.3171/2018.1.JNS172766.

118. Su, H. *et al.* Reduced expression of integrin alphavbeta8 is associated with brain arteriovenous malformation pathogenesis. *Am. J. Pathol.* **176**, 1018–1027 (2010).

119. Yao, R., Alkhawtani, A. Y. F., Chen, R., Luan, J. & Xu, M. Rapid and efficient in vivo angiogenesis directed by electro-assisted bioprinting of alginate/collagen microspheres with human umbilical vein endothelial cell coating layer. *Int. J. Bioprinting* **5**, 194 (2019).

120. Walker, E. J. *et al.* Bevacizumab attenuates VEGF-induced angiogenesis and vascular malformations in the adult mouse brain. *Stroke* **43**, 1925–1930 (2012).

121. Winkler, E. A. *et al.* Defective vascular signaling & prospective therapeutic targets in brain arteriovenous malformations. *Neurochem. Int.* **126**, 126–138 (2019).

122. Zhu, W. *et al.* Thalidomide Reduces Hemorrhage of Brain Arteriovenous Malformations in a Mouse Model. *Stroke* **49**, 1232–1240 (2018).

123. Pan, P., Shaligram, S. S., Do Prado, L. B., He, L. & Su, H. The role of mural cells in hemorrhage of brain arteriovenous malformation. *Brain Hemorrhages* **2**, 49–56 (2021).

124. Lindahl, P., Johansson, B. R., Levéen, P. & Betsholtz, C. Pericyte loss and microaneurysm formation in PDGF-B-deficient mice. *Science* **277**, 242–245 (1997).

125. Lebrin, F. *et al.* Thalidomide stimulates vessel maturation and reduces epistaxis in individuals with hereditary hemorrhagic telangiectasia. *Nat. Med.* **16**, 420–428 (2010).

126. Li, Z., Ma, L., Wu, C., Ma, J. & Chen, X. Pediatric brain arteriovenous malformation unfavorable hemorrhage risk: extrapolation to a morphologic model. *Chin. Neurosurg. J.* **4**, 15 (2018).

127. Jiang, X. *et al.* Inactivating mutations in Drosha mediate vascular abnormalities similar to hereditary hemorrhagic telangiectasia. *Sci. Signal.* **11**, eaan6831 (2018).

128. Feng, X. *et al.* A Platform of Synthetic Lethal Gene Interaction Networks Reveals that the GNAQ Uveal Melanoma Oncogene Controls the Hippo Pathway through FAK. *Cancer Cell* **35**, 457-472.e5 (2019).

129. Truong, A. *et al.* Chloroquine Sensitizes GNAQ/11-mutated Melanoma to MEK1/2 Inhibition. *Clin. Cancer Res. Off. J. Am. Assoc. Cancer Res.* (2020) doi:10.1158/1078-0432.CCR-20-1675.

130. van Weeghel, C. *et al.* Do GNAQ and GNA11 Differentially Affect Inflammation and HLA Expression in Uveal Melanoma? *Cancers* **11**, (2019).

131. Krebs, F. S. *et al.* Trametinib Induces the Stabilization of a Dual GNAQ p.Gly48Leu- and FGFR4 p.Cys172Gly-Mutated Uveal Melanoma. The Role of Molecular Modelling in Personalized Oncology. *Int. J. Mol. Sci.* **21**, (2020).

132. Rietschel, P. *et al.* Variates of survival in metastatic uveal melanoma. *J. Clin. Oncol. Off. J. Am. Soc. Clin. Oncol.* **23**, 8076–8080 (2005).

133. Pyrhönen, S. The treatment of metastatic uveal melanoma. *Eur. J. Cancer Oxf. Engl. 1990* **34 Suppl 3**, S27-30 (1998).

134. Zuidervaart, W. *et al.* Activation of the MAPK pathway is a common event in uveal melanomas although it rarely occurs through mutation of BRAF or RAS. *Br. J. Cancer* **92**, 2032–2038 (2005).

135. Boru, G. *et al.* Heterogeneity in Mitogen-Activated Protein Kinase (MAPK) Pathway Activation in Uveal Melanoma With Somatic GNAQ and GNA11 Mutations. *Invest. Ophthalmol. Vis. Sci.* **60**, 2474–2480 (2019).

136. Yoo, J. H. *et al.* ARF6 Is an Actionable Node that Orchestrates Oncogenic GNAQ Signaling in Uveal Melanoma. *Cancer Cell* **29**, 889–904 (2016).

137. Liau, J.-Y. *et al.* High frequency of GNA14, GNAQ, and GNA11 mutations in cherry hemangioma: a histopathological and molecular study of 85 cases indicating GNA14 as the most commonly mutated gene in vascular neoplasms. *Mod. Pathol. Off. J. U. S. Can. Acad. Pathol. Inc* **32**, 1657–1665 (2019).

138. Le Guin, C. H. D. *et al.* GNAQ Q209R Mutations Are Highly Specific for Circumscribed Choroidal Hemangioma. *Cancers* **11**, (2019).

139. Huang, L. *et al.* Endothelial GNAQ p.R183Q Increases ANGPT2 (Angiopoietin-2) and Drives Formation of Enlarged Blood Vessels. *Arterioscler. Thromb. Vasc. Biol.* **42**, e27–e43 (2022).

140. Soon, K. *et al. Development and Characterization of a Human Model of Arteriovenous Malformation (AVM)-on-a-Chip*. http://biorxiv.org/lookup/doi/10.1101/2022.01.20.477166 (2022) doi:10.1101/2022.01.20.477166.

141. GARD. *Genetic and Rare Diseases (GARD) Information Center* https://rarediseases.info.nih.gov/.

142. NORD. *NORD (National Organization for Rare Disorders)* https://rarediseases.org/.

143. Wan, H.-Y. *et al.* Stabilization and improved functionality of three-dimensional perfusable microvascular networks in microfluidic devices under macromolecular crowding. *Biomater. Res.* **27**, 32 (2023).

144. Maurissen, T. L. *et al.* Modeling early pathophysiological phenotypes of diabetic retinopathy in a human inner blood-retinal barrier-on-a-chip. *Nat. Commun.* **15**, 1372 (2024).

145. Offeddu, G. S. *et al.* Microphysiological endothelial models to characterize subcutaneous drug absorption. *ALTEX* **40**, 299–313 (2023).

146. Rota, A. *et al.* A three-dimensional method for morphological analysis and flow velocity estimation in microvasculature on-a-chip. *Bioeng. Transl. Med.* **8**, e10557 (2023).

147. Blazeski, A. *et al.* Engineering microvascular networks using a KLF2 reporter to probe flow-dependent endothelial cell function. *bioRxiv* 2023.10.31.565021 (2023) doi:10.1101/2023.10.31.565021.

148. Park, H. *et al.* Defective Flow-Migration Coupling Causes Arteriovenous Malformations in Hereditary Hemorrhagic Telangiectasia. *Circulation* **144**, 805–822 (2021).

149. Kim, Y. I., Lee, C.-Y. & Shin, M. K. Downregulation of activin-signaling gene expression in passaged normal human dermal fibroblasts. *Biomed. Rep.* **12**, 17–22 (2020).

150. Wietecha, M. S. *et al.* Activin-mediated alterations of the fibroblast transcriptome and matrisome control the biomechanical properties of skin wounds. *Nat. Commun.* **11**, 2604 (2020).

151. Attisano, L., Wrana, J. L., Montalvo, E. & Massagué, J. Activation of signalling by the activin receptor complex. *Mol. Cell. Biol.* **16**, 1066–1073 (1996).

152. Corliss, B. A. *et al.* REAVER: A program for improved analysis of high-resolution vascular network images. *Microcirc. N. Y. N 1994* **27**, e12618 (2020).

153. Tucker, W. D., Arora, Y. & Mahajan, K. Anatomy, Blood Vessels. in *StatPearls* (StatPearls Publishing, Treasure Island (FL), 2024).

154. CDC. Million Hearts® Turning Point. *Centers for Disease Control and Prevention* https://www.cdc.gov/grand-rounds/pp/2014/20140916-heart-abcs.html (2018).

155. Nakatsu, M. N., Davis, J. & Hughes, C. C. W. Optimized fibrin gel bead assay for the study of angiogenesis. *J. Vis. Exp. JoVE* 186 (2007) doi:10.3791/186.

156. Nakatsu, M. N. & Hughes, C. C. W. An optimized three-dimensional in vitro model for the analysis of angiogenesis. *Methods Enzymol.* **443**, 65–82 (2008).

157. Ng, A. H. M. *et al.* A comprehensive library of human transcription factors for cell fate engineering. *Nat. Biotechnol.* (2020) doi:10.1038/s41587-020-0742-6.

158. Wang, K. *et al.* Robust differentiation of human pluripotent stem cells into endothelial cells via temporal modulation of ETV2 with modified mRNA. *Sci. Adv.* **6**, eaba7606 (2020).

159. Abutaleb, N. O. & Truskey, G. A. Differentiation and characterization of human iPSC-derived vascular endothelial cells under physiological shear stress. *STAR Protoc.* **2**, 100394 (2021).

160. Kim, C. Disease modeling and cell based therapy with iPSC: future therapeutic option with fast and safe application. *Blood Res.* **49**, 7–14 (2014).

161. Atchison, L. *et al.* iPSC-Derived Endothelial Cells Affect Vascular Function in a Tissue-Engineered Blood Vessel Model of Hutchinson-Gilford Progeria Syndrome. *Stem Cell Rep.* **14**, 325–337 (2020).

162. Jang, S., Collin de l'Hortet, A. & Soto-Gutierrez, A. Induced Pluripotent Stem Cell–Derived Endothelial Cells. *Am. J. Pathol.* **189**, 502–512 (2019).

163. Fan, X. *et al.* Functional Characterization of Human Induced Pluripotent Stem Cell-Derived Endothelial Cells. *Int. J. Mol. Sci.* **23**, 8507 (2022).

164. Williams, I. M. & Wu, J. C. Generation of Endothelial Cells From Human Pluripotent Stem Cells. *Arterioscler. Thromb. Vasc. Biol.* **39**, 1317–1329 (2019).

165. Hsu, Y.-H., Moya, M. L., Hughes, C. C. W., George, S. C. & Lee, A. P. A microfluidic platform for generating large-scale nearly identical human microphysiological vascularized tissue arrays. *Lab. Chip* **13**, 2990–2998 (2013).

166. R Studio. *RStudio: integrated development environment for R.* https://posit.co/download/rstudio-desktop/.

167. R: The R Project for Statistical Computing. https://www.r-project.org/.

168. Butler, A., Hoffman, P., Smibert, P., Papalexi, E. & Satija, R. Integrating single-cell transcriptomic data across different conditions, technologies, and species. *Nat. Biotechnol.* **36**, 411–420 (2018).

169. Satija, R., Farrell, J. A., Gennert, D., Schier, A. F. & Regev, A. Spatial reconstruction of single-cell gene expression data. *Nat. Biotechnol.* **33**, 495–502 (2015).

170. McGinnis, C. S., Murrow, L. M. & Gartner, Z. J. DoubletFinder: Doublet Detection in Single-Cell RNA Sequencing Data Using Artificial Nearest Neighbors. *Cell Syst.* **8**, 329-337.e4 (2019).

171. Patterson-Cross, R. B., Levine, A. J. & Menon, V. Selecting single cell clustering parameter values using subsampling-based robustness metrics. *BMC Bioinformatics* **22**, 39 (2021).

172. Ho, M. *et al.* Identification of endothelial cell genes by combined database mining and microarray analysis. *Physiol. Genomics* **13**, 249–262 (2003).

173. Muhl, L. *et al.* Single-cell analysis uncovers fibroblast heterogeneity and criteria for fibroblast and mural cell identification and discrimination. *Nat. Commun.* **11**, 3953 (2020).

174. Reference Genome Group of the Gene Ontology Consortium. The Gene Ontology's Reference Genome Project: a unified framework for functional annotation across species. *PLoS Comput. Biol.* **5**, e1000431 (2009).

175. Yu, G., Wang, L.-G., Han, Y. & He, Q.-Y. clusterProfiler: an R package for comparing biological themes among gene clusters. *Omics J. Integr. Biol.* **16**, 284–287 (2012).

176. Zhang, L. & Nie, Q. scMC learns biological variation through the alignment of multiple single-cell genomics datasets. *Genome Biol.* **22**, 10 (2021).

177. Coombes, K. R., Brock, G., Abrams, Z. B. & Abruzzo, L. V. Polychrome: Creating and Assessing Qualitative Palettes with Many Colors. *J. Stat. Softw.* **90**, 1–23 (2019).

178. Schrenk, S. *et al.* MEK inhibition reduced vascular tumor growth and coagulopathy in a mouse model with hyperactive GNAQ. *Nat. Commun.* **14**, 1929 (2023).

179. Zecchin, D. *et al.* GNAQ/GNA11 Mosaicism Causes Aberrant Calcium Signaling Susceptible to Targeted Therapeutics. *J. Invest. Dermatol.* **144**, 811-819.e4 (2024).

180. Krantz, B. A., Dave, N., Komatsubara, K. M., Marr, B. P. & Carvajal, R. D. Uveal melanoma: epidemiology, etiology, and treatment of primary disease. *Clin. Ophthalmol. Auckl. NZ* **11**, 279–289 (2017).

181. Nicholson, C. L. *et al.* Successful management of an arteriovenous malformation with trametinib in a patient with capillary-malformation arteriovenous malformation syndrome and cardiac compromise. *Pediatr. Dermatol.* **39**, 316–319 (2022).

182. Sahara, M. *et al.* Manipulation of a VEGF-Notch signaling circuit drives formation of functional vascular endothelial progenitors from human pluripotent stem cells. *Cell Res.* **24**, 820–841 (2014).

183. Langenfeld, E. M. & Langenfeld, J. Bone morphogenetic protein-2 stimulates angiogenesis in developing tumors. *Mol. Cancer Res. MCR* **2**, 141–149 (2004).

184. Raida, M. *et al.* Bone morphogenetic protein 2 (BMP-2) and induction of tumor angiogenesis. *J. Cancer Res. Clin. Oncol.* **131**, 741–750 (2005).

185. Zuo, W. *et al.* Promotive effects of bone morphogenetic protein 2 on angiogenesis in hepatocarcinoma via multiple signal pathways. *Sci. Rep.* **6**, 37499 (2016).

186. Benn, A. *et al.* Role of bone morphogenetic proteins in sprouting angiogenesis: differential BMP receptor-dependent signaling pathways balance stalk vs. tip cell competence. *FASEB J. Off. Publ. Fed. Am. Soc. Exp. Biol.* **31**, 4720–4733 (2017).

187. Chen, W.-C. *et al.* BMP-2 induces angiogenesis by provoking integrin α6 expression in human endothelial progenitor cells. *Biochem. Pharmacol.* **150**, 256–266 (2018).

188. Dyer, L. A., Pi, X. & Patterson, C. The role of BMPs in endothelial cell function and dysfunction. *Trends Endocrinol. Metab. TEM* **25**, 472–480 (2014).